

# Additive engineering for highly efficient and stable perovskite solar cells



Cite as: Appl. Phys. Rev. **10**, 011308 (2023); doi: [10.1063/5.0097704](https://doi.org/10.1063/5.0097704)

Submitted: 30 April 2022 · Accepted: 5 January 2023 ·

Published Online: 14 February 2023



View Online



Export Citation



CrossMark

Do-Kyoung Lee<sup>1</sup> and Nam-Gyu Park<sup>1,2,a)</sup>

## AFFILIATIONS

<sup>1</sup>School of Chemical Engineering and Center for Antibonding Regulated Crystals, Sungkyunkwan University, Suwon 16419, South Korea

<sup>2</sup>SKKU Institute of Energy Science and Technology (SIEST), Sungkyunkwan University, Suwon 16419, South Korea

Note: This paper is part of the special collection on Energy Storage and Conversion.

<sup>a)</sup>Author to whom correspondence should be addressed: [npark@skku.edu](mailto:npark@skku.edu)

## ABSTRACT

Since the groundbreaking report on solid-state perovskite solar cells (PSCs) in 2012, PSC receives great attention due to its high power conversion efficiency (PCE) obtainable at low-cost fabrication. A PCE of 9.7% in 2012 was swiftly improved to 25.7% in 2022 via perovskite composition engineering and grain size control. The excellent photovoltaic performance originates from the defect-tolerant property of organic lead halide perovskite associated with the antibonding nature of the valence band. Nevertheless, the reduction of defect-induced trap density of the state is still required to improve further photovoltaic performance and stability. Among the methods reported to reduce defects, additive engineering is one of the promising strategies for controlling crystallographic defects because it can regulate crystallization kinetics and grain boundaries. In this review, we describe materials and methods for additive engineering applied to lead-based perovskite. In addition, the effects of additive engineering on photovoltaic performance and stability are discussed.

Published under an exclusive license by AIP Publishing. <https://doi.org/10.1063/5.0097704>

## TABLE OF CONTENTS

|   |    |
|---|----|
| I. INTRODUCTION .....   | 1  |
| II. PREREQUISITE FOR ADDITIVE ENGINEERING .....                             | 2  |
| A. Defect chemistry .....   | 2  |
| B. Nucleation and crystal growth .....                                      | 5  |
| C. Additive engineering for controlling defects in Pb-based perovskite..... | 6  |
| III. ADDITIVES IN PRECURSOR SOLUTION AND THEIR EFFECTS.....                 | 7  |
| A. Cationic additives .....   | 7  |
| 1. Organic cations.....   | 7  |
| 2. Inorganic cations .....  | 10 |
| B. Anionic additives.....   | 12 |
| 1. Halide anions .....  | 12 |
| 2. Non-halide anions .....  | 14 |
| C. Multifunctional additives.....   | 16 |
| 1. Molecules and polymers as Lewis base additives.....                      | 16 |
| 2. Organosilane-based cross-linking additives .....                         | 19 |
| 3. Surfactant additives .....   | 19 |
| IV. SUMMARY AND PERSPECTIVE .....   | 20 |

## I. INTRODUCTION

Organic ammonium and divalent lead cation are coordinated with twelve and six halide anions, respectively, to form perovskite, that is, a key light-absorbing material for perovskite solar cells (PSCs). The state-of-the-art technology led to a certified power conversion efficiency (PCE) of 25.7%.<sup>1</sup> Perovskite, discovered in 1839 from CaTiO<sub>3</sub>,<sup>2</sup> has a unique structure allowing large cations in the cubo-octahedral A-site of ABX<sub>3</sub> (X = oxygen or halogen).<sup>3,4</sup> Oxide perovskites were reported to show interesting properties such as ferroelectricity,<sup>5–7</sup> superconductivity,<sup>8–10</sup> and catalytic properties.<sup>11,12</sup> By taking advantage of large cations in the A-site, organic methylammonium (MA) was introduced to form lead- or tin-based halide perovskites in 1978.<sup>13,14</sup> Color change was observed from colorless to dark black as halide changed from chloride to iodide, which indicate the decrease in the bandgap. In 2009, methylammonium lead iodide (MAPbI<sub>3</sub>) and bromide (MAPbBr<sub>3</sub>) were first used as a sensitizer in dye-sensitized solar cells,<sup>15</sup> where MAPbI<sub>3</sub> adsorbed on the mesoporous TiO<sub>2</sub> film resulted in a PCE of 3.8%. Almost doubled PCE of 6.5% was reported by Park's group in 2011 via precursor solution engineering,<sup>16</sup> which was, however, unnoticed because of the instability of perovskite in the presence of a polar liquid electrolyte. A substantially stable PSC was developed

using a solid hole conducting material, spiro-OMeTAD [(2,2',7,7'-Tetrakis[N,N-di(4-methoxyphenyl)amino]-9,9'-spirobifluorene],<sup>17</sup> which demonstrated a PCE of 9.7% together with long-term stability for 500 h under an ambient condition. This breakthrough result has triggered perovskite photovoltaic research.

In addition to the photovoltaic application, halide perovskites were also found to be suitable for the light emitting diode (LED),<sup>18–22</sup> memristors,<sup>23–28</sup> photodetector,<sup>29,30</sup> and laser diode<sup>31,32</sup> due to their superior opto-electronic properties.<sup>33–48</sup> Thus, devices employing halide perovskites are considered to be commercially viable.<sup>49–51</sup> Although recent research has been focused on technologies for commercialization such as scale-up processes<sup>52,53</sup> and tandem devices,<sup>54,55</sup> operational stability is one of the issues to be solved.<sup>56–58</sup> Regarding efficiency, there is still room for enhancement toward the Shockley–Queisser (S–Q) limit.<sup>59,60</sup> The attainable efficiency was theoretically studied,<sup>61–63</sup> where a PCE of over 30% was expected from perovskites with a bandgap of 1.47–1.6 eV. For instance, MAPbI<sub>3</sub> with a bandgap of ~1.6 eV and FAPbI<sub>3</sub> (FA = formamidinium) with a bandgap of 1.47 eV could achieve a PCE of 30.1% and 31.7%, respectively. However, in real devices, lower efficiencies have been observed due to a few gap between the measured open-circuit voltage ( $V_{OC}$ ) and fill factor (FF) and the theoretical ones. The loss of  $V_{OC}$  and FF is related to Shockley–Read–Hall (SRH) recombination associated with bulk and interface defects.<sup>64,65</sup> Defects present in the semiconductor are fatal factors that adversely affect the charge carrier dynamics, resulting in diminishing the photovoltaic performance.<sup>66,67</sup> For halide perovskite materials, various defects can be also induced. However, a long charge carrier lifetime was unexpectedly observed, which is mainly due to the defect-tolerant property.<sup>45,48</sup> Nevertheless, defects in halide perovskite are required to be controlled in order to minimize recombination and improve stability.

As mentioned earlier, operational stability is related to defects of halide perovskite films and devices. According to International Electrotechnical Commission (IEC) 61215/61646 protocol,<sup>68</sup> the operational stability of solar modules is evaluated by tracking photovoltaic performance as a function of exposure time under harsh environmental conditions such as the UV exposure test with elevated temperature, the light soaking test under 600–1000 W/m<sup>2</sup> at a temperature of 50 °C ± 10 °C, the humidity-freeze cycling test under a relative humidity (RH) of 85% ± 5% at 85 °C to –40 °C ± 2 °C, the thermal stress test with thermal cycling at a temperature from –40 °C ± 2 °C to 85 °C ± 2 °C, and the damp-heat test at 85 °C ± 2 °C under 85% ± 5% RH for 1000 h. Despite efforts made to improve the operational stability of PSCs, the stability of PSCs is by far not as good as the commercial silicon solar cell. This might be due to high bulk and grain boundary defects of ionic characteristic halide perovskite.<sup>69,70</sup> In addition, the opto-electric properties cannot be maintained under high humid environment due to the dissolution problem of the perovskite.<sup>71</sup> Regarding factors affecting the stability of PSCs, heat is also one of the factors affecting the stability of perovskite.<sup>72</sup> Since lead halide perovskite has relatively low deformation energy and is composed of volatile organic substances such as methylamine, its crystal structure can be deformed and the constituent substances can be dissipated at elevated temperatures. Thermally activated ion migration and/or the reorientation dynamics of dipolar organic cations induced by point defects leads to deformation of the crystal structure,<sup>73–75</sup> where the migration of charged defects can be driven by light.<sup>76</sup>

Furthermore, the halide, especially iodide, tends to be oxidized under a UV-visible light source and the iodine disappears via the sublimation processes, which can damage the perovskite crystal structure. Degradation of the perovskite film can be accelerated by excess photo-generated charge carriers accumulated or trapped at the surface and grain boundaries. Not only the external environmental conditions such as heat, light, and moisture, but the crystalline phase could affect the stability of PSCs.<sup>77</sup> Typically, Goldschmidt's tolerance factor ( $t$ ) has been used to determine the distortion and stability (formability) of the perovskite crystal structure,<sup>78</sup> where the optimal range of the tolerance factor is suggested to be  $0.9 \leq t \leq 1$ . For the smaller ( $t < 0.9$ ) and higher ( $t > 1.0$ ) cases, the non-perovskite crystal structure is thermodynamically stabilized. For instance, FAPbI<sub>3</sub> with  $t$  slightly higher than 1 is stabilized to cubic perovskite phase at a temperature above 150 °C, which tends to be transformed to a non-perovskite hexagonal phase at room temperature.<sup>79–81</sup> Therefore, regarding the stability of PSCs, thermodynamic phase stability is also one of the important factors, which will be discussed in detail in the *cationic additives* parts.

**When considering the factors affecting photovoltaic performance and stability of PSCs as a whole, defects of perovskite films seem to be strongly involved.** Thus, understanding the origin of defect formation in perovskite film is critical for achieving highly efficient and stable PSCs and defect-less high-quality perovskite films as well. Among the reported methods to minimize defects, additive engineering is one of the effective approaches.<sup>82,83</sup> The state-of-the-art PSCs demonstrating PCEs over 23% since 2018 have used additives in the perovskite precursor solutions, where the additives were found to play important roles in regulating the crystallization kinetics and passivating grain boundaries.

In this review, we describe the recent progress of additive engineering and its effect on the perovskite film quality and photovoltaic performance of PSCs. In order to understand the role of additives in controlling the crystallinity and defects of perovskite films, we briefly describe the defect chemistry and crystal nucleation and growth. Additives are categorized here into cationic additive, anionic additive, and multifunctional additive since the ions dissociated from the additive interact with perovskite precursor ions or clusters. This review is believed to give important insight into the role of additives and the design of defect-less high-quality perovskite films.

## II. PREREQUISITE FOR ADDITIVE ENGINEERING

### A. Defect chemistry

It is natural that various defects are spontaneously formed based on thermodynamics. According to the third law of thermodynamics, an ideally defect-free perfect crystal can be formed only at absolute zero (Kelvin scale). However, it is impossible to form a perfect crystal at a given temperature because entropy, associated with the defect, is not zero as given in the following equation:

$$\Delta G = \Delta H - T\Delta S, \quad (1)$$

where  $G$ ,  $H$ ,  $S$ , and  $T$  are the free energy, the enthalpy, the entropy, and the temperature, respectively. In Fig. 1(a), free energy change ( $\Delta G$ ) is plotted as a function of defect concentration, where a certain concentration of defect is inevitably required to minimize  $\Delta G$ . Thus, the presence of defects in semiconductor materials is unavoidable based on thermodynamics.<sup>84,85</sup>

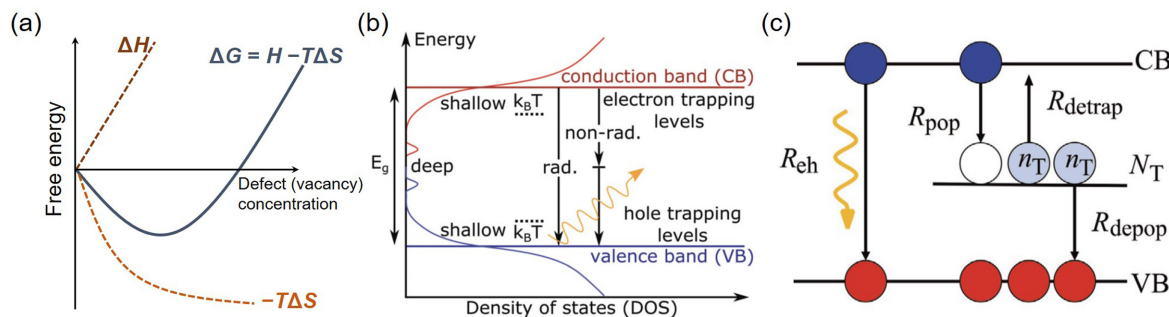


**FIG. 1.** (a) Free energy of crystal formation as a function of the defect concentration. (b) The density of states (DOS) showing shallow and deep traps along with radiative and non-radiative recombination. Reproduced with permission from Jin *et al.*, Mater. Horiz. 7, 397 (2020). Copyright 2020 Royal Society of Chemistry.<sup>89</sup> (c) Recombination processes of trap-mediated non-radiative recombination and band-to-band radiative recombination, where  $R_{eh}$  is the rate constant of radiative recombination,  $R_{pop}$  is the rate constant of non-radiative recombination with the free trap states and excited electrons in CB,  $R_{detrap}$  is the rate constant for detrapping behavior of trapped charge carriers,  $R_{depop}$  is the rate constant of non-radiative recombination with holes and trapped charge carriers,  $n_T$  is the density of trapped charge carriers, and  $N_T$  is total trap density. Reproduced with permission from Trimpl *et al.*, Adv. Funct. Mater. 30, 2004312 (2020). Copyright 2020 Wiley-VCH GmbH.<sup>92</sup>

Defects in semiconductor materials have an ill influence on charge carrier dynamics.<sup>86–88</sup> In general, the electronic energy states of the defect (vacancies, interstitial, impurities, etc.) are mostly presented in the bandgap between valence band maximum (VBM) and conduction band minimum (CBM), which creates shallow or deep level traps [Fig. 1(b)].<sup>89</sup> These defective states can interfere with the desired charge carrier dynamics by trapping carriers generated within the semiconductors. In particular, carriers trapped by deep-level states exhibit a relatively ultraslow response to detrapping processes or cannot be escaped from their states compared with those trapped by the shallow-level state. Both shallow- and deep-level states in association with defects lead to SRH recombination, also called trap-mediated non-radiative recombination, which interferes with charge carrier dynamics in terms of carrier transporting and extraction behavior [Fig. 1(c)].<sup>90–92</sup> In addition, such defects have caused a lot of detrimental effects such as low reliability and performance of devices based on semiconductors as well as the accelerated degradation of materials. Therefore, controlling defects in materials is one of the important technologies in semiconductor-based devices.

In ionic crystals, defects occur due to impurity, vacancy, dislocation, etc. Crystallographic defects can be categorized according to their dimension. For example, zero-dimensional (0D) defects are called point defects, including vacancy, interstitial, Schottky, Frenkel, and antisite defects.<sup>103,104</sup> It is also divided into line, plane, and volume defects according to 1D, 2D, and 3D, respectively, and each is classified into detailed defect forms. Among them, point defects can be propagated to defects of different dimensions, indicating that it might be the origin of defect formation in various dimensions. Defect formation in semiconductor materials is related to surface energy, which is proportional to the surface area, atomic bonding strength, and the number of bonds on the surface.<sup>93,94</sup> That is, the deformation and propagation to other forms of defects can occur to induce the dislocation of atomic arrangement and agglomeration of defects or crystals for the relaxation of the unstable state as the surface energy increases when the point defect concentration increases.<sup>95,96</sup> Other defects should be considered necessary, but point defects are one of the most important parts of the field of materials science as they can be the root cause of other dimensional defects. Hence, it is important to identify the origin of defects and to understand the mechanism of point defect formation.

For organic-inorganic metal halide perovskites, studies on defect chemistry have been intensively carried out to understand the formation mechanism and characteristics of defects. It is well known that halide perovskite shows defect-tolerant characteristics probably due to its unique chemical bonding nature. The  $ns$  and  $np$  orbitals of the p-block metal element (Pb or Sn) and the p-block halide element (Cl, Br, or I) mainly contribute to the band structure. A-site cations also affect the band structure, but it might be inadequate and more related to the phase stability than band-edge characteristics. For the  $\text{APbI}_3$  perovskite, the ground state electronic configuration of Pb and I is  $[\text{Xe}]4f^{14}5d^{10}6s^26p^2$  and  $[\text{Kr}]4d^{10}5s^25p^5$ , respectively. Based on a linear combination of atomic orbitals (LCAO), molecular orbital (MO) can be constructed by overlapping 6s and 6p orbitals of Pb with the 5p orbital of I. As can be seen in the simple picture of MO in Fig. 2(a),<sup>45</sup> the antibonding orbital formed by 5p of I and 6s of Pb overlap is occupied, contributing to VBM, while the formation of the CBM is associated with the unoccupied antibonding due to overlap of 5p of I and 6p of Pb. The antibonding character in VBM is responsible for a defect-tolerant property because the iodide dangling bond formed by lead cation vacancy will be resonant in VB. This characteristic has been demonstrated through computational simulation and fundamental analysis such as density of states (DOS) calculated from density functional theory (DFT),<sup>97,98</sup> projected crystal orbital Hamilton population (pCOHP),<sup>99</sup> and population of defective transition levels calculated by Heyd–Scuseria–Ernzerhof (HSE) hybrid method with combining spin-orbit coupling (SOC) effects.<sup>100,101</sup> Despite the defect-tolerant property, deep traps might be generated depending on the orbital alignment and structural deformation.<sup>102</sup> Thus, the defect is not negligible and should be carefully handled in halide perovskite. Defects in halide perovskite can result from the uncoordinated atoms mostly on the surface and the migration of ionic species and charged defects in an external electric field. Most of the reports on defects of halide perovskites have focused on 0D point defects and 2D planar defects (surface and grain boundaries). For point defects, vacancies with different charges result in such as Schottky defect since ionic crystals tend to maintain charge neutrality. Defect formation energy (DFE) and thermodynamic ionization energy levels estimated by DFT calculation are an invaluable information to determine and analyze the possible defects in perovskite materials.<sup>103–105</sup> DFEs can be estimated by Eq. (2) used in the supercell approach,<sup>104,106</sup>

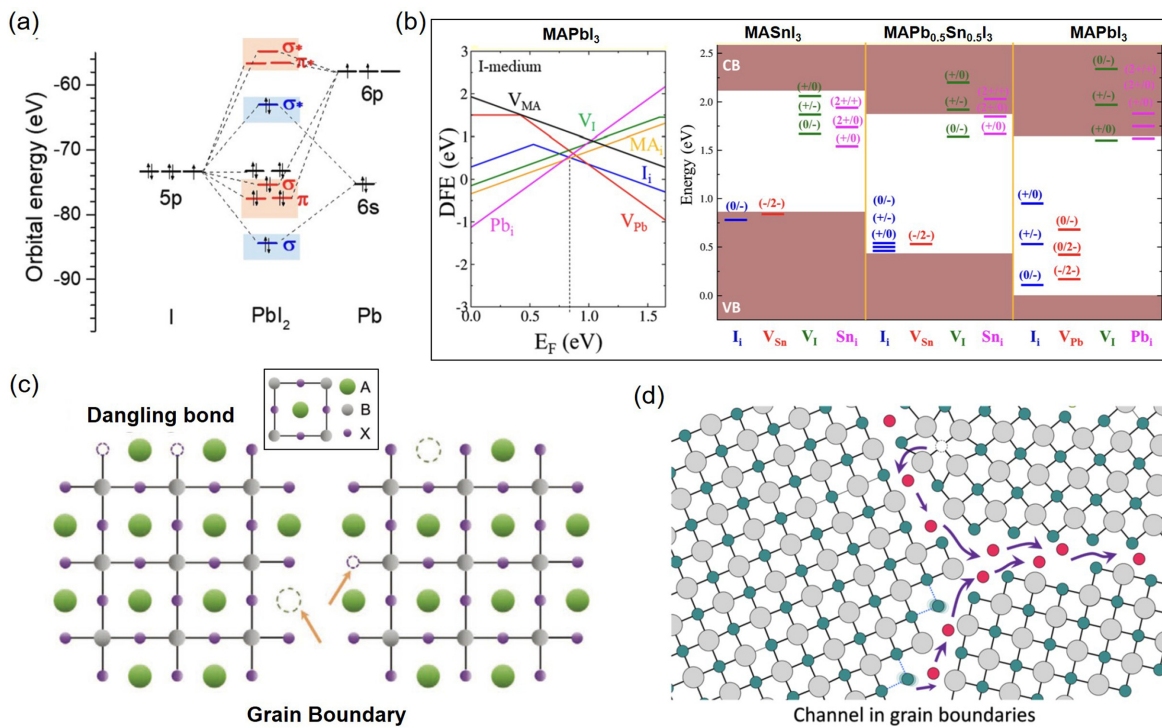


**FIG. 2.** (a) Molecular orbital of lead iodide constructed simply by a linear combination of atomic orbital (LCAO). Reproduced with permission from Kim *et al.*, Chem. Rev. **120**, 7867 (2020). Copyright 2020 American Chemical Society.<sup>45</sup> (b) (left one panel) Defect formation energies for iodide medium (I-medium) condition of MAPbI<sub>3</sub>. (right three panels) Thermodynamic ionization energies of defects in MAPbI<sub>3</sub>, MAPb<sub>0.5</sub>Sn<sub>0.5</sub>I<sub>3</sub> and MASnI<sub>3</sub>. Reproduced with permission from Meggiolaro *et al.*, J. Phys. Chem. Lett. **11**, 3546 (2020). Copyright 2020 American Chemical Society.<sup>107</sup> (c) Schematic illustration of a crystal lattice with vacancies (dangling bond) at surfaces and grain boundaries. Reproduced with permission from Li *et al.*, Adv. Mater. **34**, 2108102 (2022). Copyright 2022 Wiley-VCH GmbH.<sup>108</sup> (d) Schematics of the ion migration throughout channel in grain boundaries. Reproduced with permission from Yuan and Huang, Acc. Chem. Res. **49**, 286 (2016). Copyright 2016 American Chemical Society.<sup>109</sup>

$$\begin{aligned} \text{DFE}(X^q) = & E_{\text{total}}(X^q) - E_{\text{perfect}} - \sum_i n_i \mu_i + q(E_F + E_{\text{VBM}} + \Delta V) \\ & + (E_{\text{corr}})^q, \end{aligned} \quad (2)$$

where  $X^q$  is the defect or impurity X in charge state q,  $E_{\text{total}}(X^q)$  is the total energy of the supercell with  $X^q$  defect,  $E_{\text{perfect}}$  is the energy of the perfect supercell without any defects,  $n_i$  is the number of type i,  $\mu_i$  is the chemical potential of type i,  $E_F$  is the Fermi level,  $E_{\text{VBM}}$  is the energy of VBM in the bulk,  $\Delta V$  is the electrostatic potential shift, and  $(E_{\text{corr}})^q$  is the electrostatic interaction correction term. Low DFE means an increase in probability to form defects. In Fig. 2(b), the DFEs depending on the defect type are plotted as a function of the Fermi level ( $E_F = E - E_{\text{VBM}}$ ).<sup>107</sup> Furthermore, thermodynamic ionization energy levels can be defined by using the calculated DFEs, where the shallow or deep level states of each defect depending on the ionized state can be determined [Fig. 2(b)]. For instance,  $V_I$  and  $Pb_i$  defect states in MAPbI<sub>3</sub> are close to CB, indicating that they have a shallow level, while  $V_I$  and  $Sn_i$  defect states in MASnI<sub>3</sub> have relatively deeper levels. On the contrary,  $I_i$  and  $V_{Sn}$  states for MAPbI<sub>3</sub> are distributed in the deep level, while  $I_i$  and  $V_{Sn}$  states for MASnI<sub>3</sub> are situated nearby VB. The DFEs and thermodynamic ionization energy levels can be also obtained by various functional approximations such as Perdew–Burke–Ernzerhof (PBE) functional. It means that the analysis and interpretation of defects may differ depending on computational modeling methods; hence, which method is more effective and

accurate has been still debated. Nevertheless, these computationally analytical methods are indispensable for a fundamental understanding of defects in perovskite materials. For the case of 2D planar defects, discontinuously oriented crystal structure is responsible for the planar defect. Grain boundary is a typical planar defect. Polycrystalline perovskite films generally contain grain boundaries and uncoordinated atoms on the surface including random crystallographic orientations of different sized grains [Figs. 2(c) and 2(d)].<sup>108,109</sup> The planar defects formed on the surface and grain boundaries are treated similarly with point defects.

Studies based on DFE and thermodynamic ionization energy levels estimated by DFT calculation have addressed the types (shallow or deep) and the species (vacancy, interstitial and antisite) of defects, defect density, and thermodynamic susceptibility of each defect possibly formed in perovskite materials. Even for the species with high DFEs or shallow characteristics, those should not be neglected due to the complicated interaction with elements and defects in perovskite systems. Commonly, vacancies originated from A-site organic cations and X-site halide anions lead to the shallow traps, which can, however, induce deep-energy-level traps in relation with Schottky and Frenkel defects. These Schottky and Frenkel defects exhibit low DFE, which means that it is probably possible to induce detrimental defects with different characteristics. For examples,  $V_X^{+}$  species is possibly interacted with  $V_B^{2-}$  through compensation reactions, resulting in the

formation of Frenkel defects with  $X_i^-$  with the deep energy level.<sup>104</sup> Vacancies associated with  $BX_2$  species can be also induced by Schottky defect formation. Since defective species with low defect density or shallow energy level can be induced in the form of fatal defects in perovskite materials, they should not be ignored. These defects are the origin of deterioration of semiconductor properties of perovskite materials. It interferes with charge carrier dynamics, resulting in severe degradation of charge carrier lifetime and diffusion length, which, in turn, influences the performance and stability of photovoltaic devices. Therefore, understanding the formation mechanism of intrinsic and extrinsic defects in perovskite materials is key to realize high efficiency and stability of PSCs toward commercialization.

The efficiency and stability of PSCs are influenced by these defects. There are three representative causes associated with defects in perovskites: (i) the formation of reactive sites that can interact with  $O_2$  and  $H_2O$ , (ii) migration of ionic species or charged defects, and (iii) interruption of charge carrier dynamics. First, oxygen and moisture can permeate through the high surface area film with many grain boundaries.<sup>71,72</sup>  $O_2$  is allowed to be placed in halide ion vacancies due to the smaller size of  $O_2$  (152 pm) than ionic radius of halide ions [ $I^-$  (198 pm),  $Br^-$  (185 pm), and  $Cl^-$  (175 pm)]. When halide perovskite is exposed to UV-visible light, reactive oxygen species ( $O_2^-$ ) are generated, which can induce the deprotonation of amine-based organic cations and thereby  $H_2O$  is produced. Thus, such reactive sites deteriorate the optical and electrical properties of PSCs due to the disruption of the compositional balance and crystal structure. Second, the ionic species and charged defects can migrate at the given temperature due to a relatively low activation energy for ion migration.<sup>103,110</sup> Under illumination or external bias conditions, ion migration of the charged species is accelerated even at room temperature.<sup>111</sup> This is one of the origins of I-V hysteresis in PSCs and the hysteretic behavior deteriorates the reliability, reproducibility, and operational stability of PSCs.<sup>109,112</sup> Third, defect interferes with charge carrier dynamics, where defect can reduce the charge carrier concentration and transporting property because defects trap carriers and slow down trapping/detrapping process for transporting. In addition, the degradation of perovskite films was reported to be accelerated by trapped charge carriers at grain boundaries.<sup>113,114</sup> Since defects in halide perovskite have theoretically and experimentally proved to strongly correlate with efficiency and stability of PSCs, effective methodologies for controlling defects are required to be developed.

## B. Nucleation and crystal growth

Since the crystallinity of semiconductors highly interrelates with defects, an improvement of crystallinity can, thus, suppress the crystallographic defects. For this reason, high-purity single crystals have been suggested for opto-electronic materials because of extremely minimized grain boundaries and crystallographic defects and thereby anticipation of excellent opto-electronic properties.<sup>41,69,115,116</sup> However, as mentioned before, polycrystal with defect is thermodynamically more stable than the single crystal. Since crystallinity refers to the degree of structural order, the extent of ordering of the atomic arrangement in a solid determines crystallinity. Lower crystallinity of halide perovskite than the conventional semiconductors like Si or GaAs leads to higher defect density of about  $\sim 10^{16\text{--}18}\text{ cm}^{-3}$  as compared to those for Si ( $\sim 10^{15}\text{ cm}^{-3}$ ) and GaAs ( $\sim 10^{13\text{--}14}\text{ cm}^{-3}$ ).<sup>84,117,118</sup> Despite high-defect density, diffusion length as long as  $\sim 10\text{ }\mu\text{m}$  and charge carrier

lifetime as high as over  $1\text{ }\mu\text{s}$  are observed from halide perovskite thanks to the defect-tolerant property. For minimizing crystallographic/structural defects by further improvement of crystallinity of halide perovskites, better understanding the nucleation and crystal growth mechanism is prerequisite.

At an initial stage, homogeneous or heterogeneous nucleation occurs to precipitate crystals by reducing solubility of solutions when the solute concentration reaches critical point of supersaturation. The formed seed crystals are grown to bigger crystals. The crystallization process has been generally explained on the basis of nucleation and crystal growth theory,<sup>119</sup> which is commonly applied in colloidal chemistry, and LaMer's model has been frequently adapted to express the crystallization mechanism of colloidal particles from the soluble monomer.<sup>119–121</sup> The presence of colloidal particles in solutions was first proved by Richard Zsigmondy, which was modeled by LaMer and co-work to address crystallization mechanism. Figure 3(a) shows the LaMer's model describing that there are three different states for the formation of colloidal particles from the liquid phase with the soluble monomer to solid phase. When increasing the concentration of solution, driven by increasing temperature for instance, nuclei are formed above minimum concentration (critical concentration,  $C_S$ ) for the nucleation (stage I). Then, the nucleation predominantly occurs up to the concentration of critical supersaturation (stage II), after which the concentration of solution is dropped and saturated due to the precipitation of particles (stage III). Although this LaMer's model briefly elucidates the nucleation and growth processes for crystallization mechanism, there are limitation to understand the actual crystallization process because LaMer's model is hard to expect the size distribution of particles. Furthermore, this model does not take the simultaneous homogeneous–heterogeneous nucleation processes and the phenomena related to growth process such as diffusion, aggregation, and Oswald ripening into consideration. Therefore, more detailed theoretical approach is required to understand the nucleation and growth processes.

Nucleation mechanism is divided into homogeneous nucleation and heterogeneous nucleation. The change of free energy [ $\Delta G(r)$ ] for homogeneous nucleation is expressed by the sum of the bulk free energy [ $\Delta G_V = (4/3)\pi r^3 \Delta G_v$ ] and the surface free energy ( $\Delta G_S = 4\pi r^2 \gamma$ ) as given in the following equation:<sup>119</sup>

$$\Delta G(r) = (4/3)\pi r^3 \Delta G_v + 4\pi r^2 \gamma, \quad (3)$$

where  $r$  is the radius of (spherical) particle,  $\Delta G_v$  is the volume free energy per unit volume, and  $\gamma$  is surface tension. Based on Eq. (3),  $\Delta G$  can be expressed as a function of  $r$  [Fig. 3(b)], where  $\Delta G_c$  and  $r_c$  are the activation (barrier) energy for nucleation and critical radius of particles, respectively. In the case of  $r < r_c$ , particles are not formed and nuclei tend to be dissolved in solution again, while particles start to grow upon  $r > r_c$ . In order to stabilize the nuclei,  $\Delta G_c$  energy should be supplied to the nuclei. Homogeneous nucleation occurs when the bonding between particles is favorable and is the process by which nuclei are formed without any preferential site. On the other hand, heterogeneous nucleation occurs at the preferential sites, that is, impurities and the reactive sites on the nucleus surface. Therefore, it is probably possible to increase the size of particles by adjusting the free energy associated with the bulk and surface or by promoting heterogeneous nucleation to induce the growth process to be dominant. Not only this, temperature changes affect the particle size. Temperature

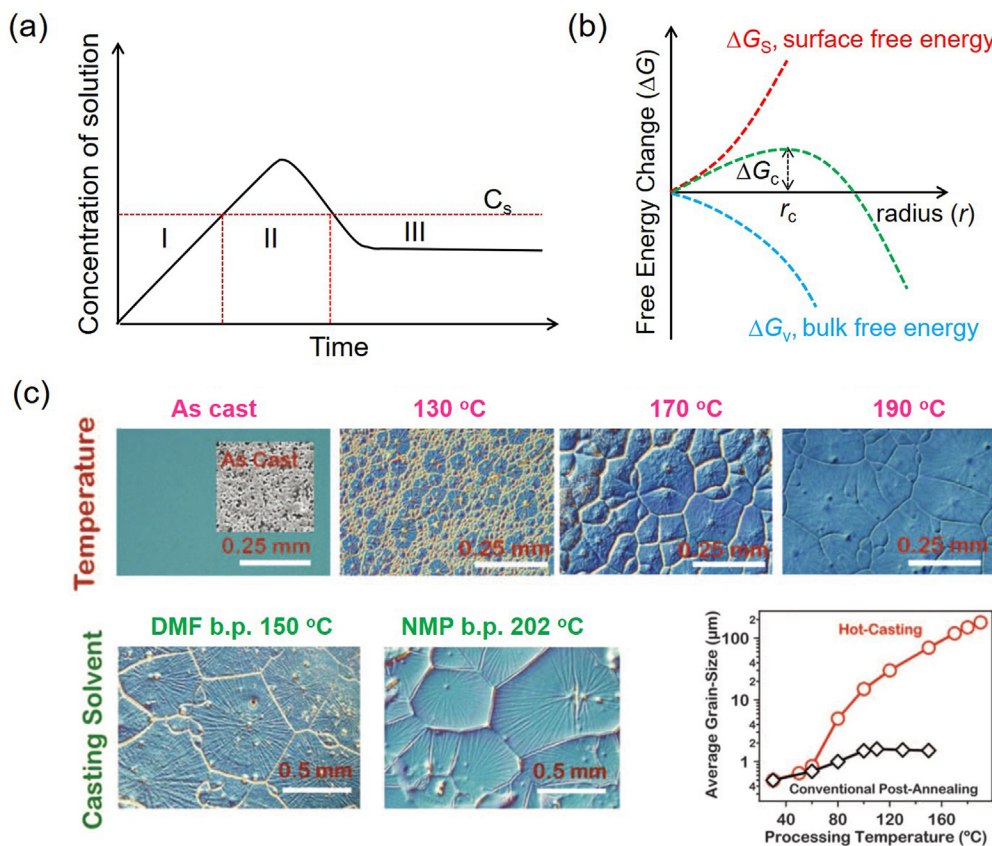


**FIG. 3.** (a) Concentration of solution as a function of reaction time based on LaMer's model. (b) Free energy change ( $\Delta G$ ) as a function of radius for the nucleation process. (c) Optical microscopic images of  $\text{MAPbI}_{3-x}\text{Cl}_x$  perovskite film depending on fabrication conditions: (top) hot-casting and (bottom left) conventional post-annealing with different solvents. (bottom right) Average grain size as a function of processing temperature for hot-casting and conventional post-annealing. Reproduced with permission from Nie et al., Science 347, 522 (2015). Copyright 2015 The American Association for the Advancement of Science.<sup>122</sup>

control can lead to large particles if the growth is dominant and the rate of nucleation is delayed. For example, it was confirmed that  $\text{MAPbI}_{3-x}\text{Cl}_x$  can be enlarged as the substrate temperature increases [Fig. 3(c)].<sup>122</sup> In this way, understanding the factors that contribute to the crystallization process can help to realize a desired crystal size. Efforts have been made to form high quality perovskite films by effectively controlling crystallization kinetics via various methods.<sup>123–125</sup> Nevertheless, the crystallization phenomena in the halide perovskite film is still unclear.

### C. Additive engineering for controlling defects in Pb-based perovskite

Numerous defects such as vacancies, interstitials, impurities, and grain boundaries cannot be circumvented in polycrystalline perovskite films. The presence of defects in perovskite films has negative effect on the ideal charge carrier dynamics, resulting in the degradation of performance and stability of photovoltaic devices. In terms of efficiency, the trap states that exist in the bandgap can diminish charge carrier lifetime, diffusion length, and carrier concentration. Moreover, ion migration and accumulation associated with hysteresis behavior will

be provoked by defects, which can reduce the reliability and reproducibility of photovoltaic performance. For representative examples, Frenkel defects of vacancies ( $\text{V}_X^+$ ) and interstitials ( $\text{X}_i^-$  or  $\text{X}_i^0$ ) can be easily induced even at room temperature due to low defect formation of halide ions in perovskite materials.<sup>104,126,127</sup> These point defects dissipate carrier transport and collection, which reduces charge carrier lifetime and diffusion length of perovskite films. Surface defects, grain boundaries, and random/non-continuous crystal orientation are also factors affecting the efficiency loss due to the failure of transport of charges to charge transporting layers or external circuits. Solution-processed polycrystalline perovskite films have dangling bond and undercoordinated ions in surface and grain boundaries, which can act as defects and directly affect the efficiency loss. Recently, the performance of practical PSCs was evaluated by comparing it with the theoretical performance limit using the S-Q limit approach.<sup>59,60</sup>  $V_{\text{OC}}$  and FF are relatively lower than the theoretical values compared to short-circuit current density ( $J_{\text{SC}}$ ), which is strongly correlated with surface and grain boundary defects. These defects can also cause the collapse of the perovskite crystal structure and the formation of active reaction sites, resulting in deterioration of the stability of PSCs. As mentioned before, the perovskite materials consisting of hygroscopic ions are

vulnerable to  $O_2$  and  $H_2O$  and has an adverse effect on stability. Defects formed by reacting with oxygen and moisture is able to lead to destruction of the perovskite crystal structure. Thermal stability is also important issue to be solved in PSCs. Organic components in perovskite materials can be easily evaporated from perovskite crystal structure due to its volatile nature at given temperature induced by the radiant heat of the sun. Moreover, light-induced degradation is also one of factors affecting the stability of PSCs, where the built-in electric field driven by light is triggered to migrate defects and charged species since the activation energy for migration of defects is related to organic cations and halide anions. The importance of the phase stability of perovskite materials has also been underlined. Based on thermodynamics, perovskite materials can be spontaneously transformed into photo-inactive non-perovskite phases due to relatively low Gibb's free energy required for phase transition, which causes deterioration of the stability of PSCs. Accordingly, the development of novel methods to passivate defects is urgently required since defects in perovskite materials are directly related to both efficiency of stability.

Regarding passivation of defects, additive engineering is one of the effective methods. Additive engineering applied in the field of PSCs is undoubtedly essential in order to realize high efficiency and stability. Additives in the perovskite precursor solution help to form high-quality perovskite films with large grain size and low fraction of grain boundaries by controlling the crystallization kinetics as well as to passivate numerous defects distributed on the surface and grain boundaries in these films. To manipulate additive engineering in PSCs, the interaction between perovskite precursors and additives is scientifically considered. In this review, recent progress in additive engineering is described, which will provide clues for designing additive engineering.

### III. ADDITIVES IN PRECURSOR SOLUTION AND THEIR EFFECTS

#### A. Cationic additives

##### 1. Organic cations

Organic cations in the cubo-octahedral site in the halide perovskite are mainly composed of ammonium functional group that can interact with  $BX_6^{4-}$  octahedra via hydrogen bonding.<sup>128</sup> Management of the A-site organic cation is one of the effective methods to control the phase or crystal structure without significantly affecting the band structure and the band-edge carrier properties.<sup>129,130</sup> Therefore, the modification of organic cations via additive engineering is desirable way to improve the properties and stability of perovskite films. Typically, FAPbI<sub>3</sub>, MAPbI<sub>3</sub>, and CsPbI<sub>3</sub> are widely used as light absorbers.

The tolerance factor is calculated to be 0.99 for FAPbI<sub>3</sub>, 0.91 for MAPbI<sub>3</sub>, and 0.84 for CsPbI<sub>3</sub> based on the cationic radius of 253 pm for FA<sup>+</sup> ( $HC(NH_2)_2^+$ ), 217 pm for MA<sup>+</sup> ( $CH_3NH_3^+$ ), and 167 pm for Cs<sup>+</sup>.<sup>45,131</sup> The bandgap of FAPbI<sub>3</sub>, MAPbI<sub>3</sub>, and CsPbI<sub>3</sub> is estimated to be 1.48, 1.55, and 1.73 eV, respectively.<sup>132</sup> FAPbI<sub>3</sub> and CsPbI<sub>3</sub> have the values close to the limit of optimal range for forming a cubic perovskite structure compared with that for MAPbI<sub>3</sub>, which implies that the formability of the cubic phase of the perovskite structure for FAPbI<sub>3</sub> and CsPbI<sub>3</sub> is lower than that for MAPbI<sub>3</sub>. A tetragonal-cubic phase of the perovskite structure for MAPbI<sub>3</sub> can be easily formed at a relatively low temperature (160 K for the tetragonal phase and 330 K

for the cubic phase), while non-perovskite hexagonal FAPbI<sub>3</sub> and orthorhombic CsPbI<sub>3</sub> are stabilized at low temperature. Relatively high temperature is required to form the cubic perovskite phase for FAPbI<sub>3</sub> (~423 K) and CsPbI<sub>3</sub> (~598 K). This obvious A-site cation effect on the phase transition seems to be influenced by the thermally active reorientation dynamics of the corresponding A-site cations.<sup>133–135</sup> Therefore, since organic cations have a significant effect on crystal structure, phase stability, and phase purity, management of chemical bonding between organic cation and inorganic lattice is expected to contribute to suppression of defects and improvement of photovoltaic performance and stability of PSCs.

For additive engineering, two methods have been used to deposit perovskite films, which is a direct coating using a perovskite solution with additive [Fig. 4(a)] and a tow-step coating via the PbI<sub>2</sub> film formed from an additive-contained PbI<sub>2</sub> solution [Fig. 4(b)]. FAPbI<sub>3</sub> has been, in general, used for PSCs in recent years, where high efficiency over 20% has been achieved by the addition of additives in the perovskite precursor solution instead of the bare precursor solution.<sup>79</sup> For instance, MACl is used as additive for most of high efficiency FAPbI<sub>3</sub>-based PSCs [Fig. 4(c)].<sup>135,136</sup> The phase transition of FAPbI<sub>3</sub> from the hexagonal phase (non-perovskite  $\delta$ -phase) to cubic phase (perovskite  $\alpha$ -phase) occurs at temperature of around 150 °C. However,  $\alpha$ -phase can be stabilized at lower temperature when introducing the smaller cation such as MA into the FA site due to the lattice contraction [Fig. 4(d)].<sup>136</sup> The large quantity of the MA cation was found to be incorporated in the as-coated  $FA_xMA_{1-x}PbI_3$  film with the cubic phase, which was transformed to nearly FAPbI<sub>3</sub> composition via the elimination of gaseous methylamine at higher temperature. Thus, the MACl additive plays a critical role in stabilizing  $\alpha$ -phase FAPbI<sub>3</sub>, where almost no MACl was left in the resulting FAPbI<sub>3</sub> film despite the fact that fairly large amount of 30%–40% MACl was initially introduced in the precursor solution. This indicates that very small amount of the MA cation is participated in stabilizing  $\alpha$ -phase cubic FAPbI<sub>3</sub>, and the process of coating, drying, and annealing should be carefully controlled to adjust the amount of MA in the final film composition. In addition, unreacted PbI<sub>2</sub> and hexagonal FAPbI<sub>3</sub> are significantly suppressed by the presence of MACl, which can lead to an improvement of phase stability. In the previous work,<sup>136</sup> high crystallinity and purity of FAPbI<sub>3</sub> perovskites were demonstrated by including 40 mol. % MACl in the perovskite precursor solution. The MA<sup>+</sup> cation and the Cl<sup>-</sup> anion are able to stabilize  $\alpha$ -phase FAPbI<sub>3</sub>. As a result, charge carrier lifetime determined by time-resolved photoluminescence (TRPL) is significantly prolonged thanks to enlarged grain size and high crystallinity, which indicates that non-radiative recombination induced by defects is substantially suppressed. The role of MACl additive was verified by DFT calculation. It was suggested that MACl could stabilize an intermediate phase in the pre-annealing step, which played an important role in implementation of the highly pure  $\alpha$ -phase FAPbI<sub>3</sub> in the post-annealing step. The certified PSCs over 25% are mostly based on the MACl additive engineering. Although the contribution of Cl<sup>-</sup> in MACl cannot be ruled out, the contribution from the MA cation seems to be more pronounced. For instance, NH<sub>4</sub>Cl was used as an additive in preparing a FAPbI<sub>3</sub> film.<sup>137</sup> However, no substantial improvement was observed in spite of the smaller cationic size of NH<sub>4</sub><sup>+</sup> (148 pm), which indicates that the organic ammonium cation in the additive plays more important role than the chloride anion.

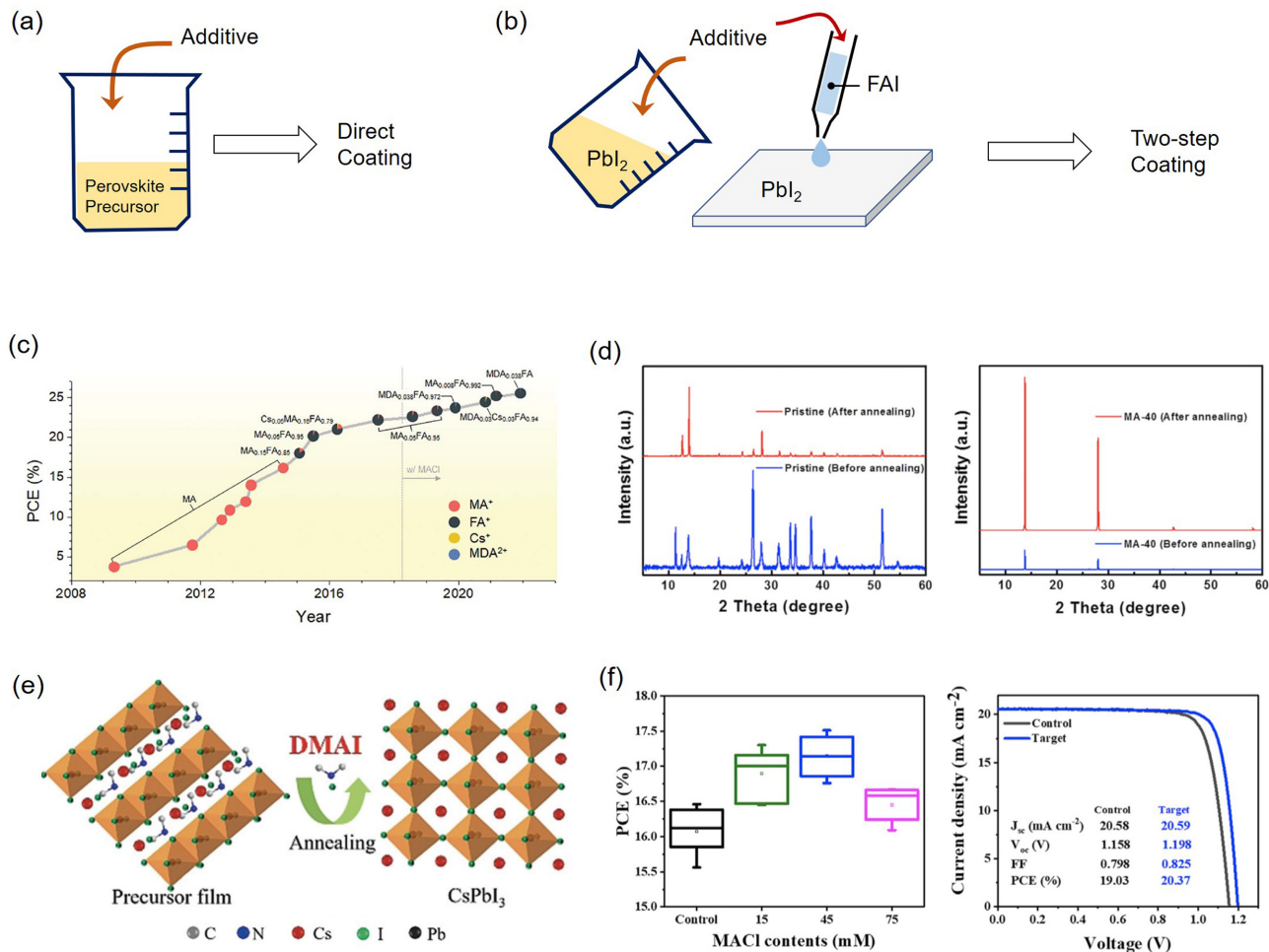


**FIG. 4.** A schematic illustration of additive engineering showing (a) direct deposition from additive-contained precursor solution and (b) two-step deposition using either a PbI<sub>2</sub> precursor solution or a FAI (for FAPbI<sub>3</sub> case) precursor solution with the additive. (c) PCE evolution of PSCs depending on the change in the A-site cation in lead iodide perovskites. Reproduced with permission from Lee *et al.*, Science **375**, eabj1186 (2022). Copyright 2022 The American Association for the Advancement of Science.<sup>135</sup> (d) XRD patterns of FAPbI<sub>3</sub>-based perovskite films without (pristine) and with 40 mol. % MACl additive (MA-40) before and after annealing. Reproduced with permission from Kim *et al.*, Joule **3**, 2179 (2019). Copyright 2019 Elsevier, Inc.<sup>136</sup> (e) Schematic illustration of the crystallization of CsPbI<sub>3</sub> via the DMAI additive. Reproduced with permission from Wang *et al.*, Angew. Chem. Int. Ed. **58**, 16691 (2019). Copyright 2019 Wiley-VCH GmbH and Co. KGaA, Weinheim.<sup>151</sup> (f) (left) Statistical PCE data of CsPbI<sub>3</sub>-based PSCs as a function of the concentration of the MACl additive and (right) comparison of J-V curves for the best-performing CsPbI<sub>3</sub>-based PSCs without (control) and with 45 mM MACl (target). Reproduced with permission from Yoon *et al.*, Joule **5**, 183 (2020). Copyright 2020 Elsevier, Inc.<sup>152</sup>

Except for cations smaller than the FA cation, larger cations have been also used as an additive. There are two types of large cations, that is, geometrically spherical and linear structures. Cations with spherical geometry include, for instance, guanidinium (GA), imidazolium (IA), and dimethylammonium (DMA). Alkylammonium derivatives are cations with linear geometry. GA-based additives (ionic radius of GA<sup>+</sup> = 278 pm) were applied to MAPbI<sub>3</sub> to enhance charge carrier lifetime and suppress ion migration, where the origin of the enhanced charge carrier lifetime was investigated.<sup>138</sup> When inducing an appropriate amount of GA (5 mol. %), charge carrier lifetime was significantly enhanced from 81 ± 2 ns for pristine (MAPbI<sub>3</sub>) to 935 ± 30 ns for GA<sub>0.05</sub>MA<sub>0.95</sub>PbI<sub>3</sub>, which contributed to the enhancement of VOC and eventually PCE. By using <sup>13</sup>C, <sup>2</sup>H, and <sup>14</sup>N magic angle spinning nuclear magnetic resonance (MAS NMR) measurement, the rate of

cation reorientation of MA and GA in GA<sub>1-x</sub>MA<sub>x</sub>PbI<sub>3</sub> was estimated to verify the correlation between rotational reorientation and charge carrier lifetime. The rate of reorientation ( $\leq 18 \pm 8$  ps) for the GA cation is much faster than that ( $113 \pm 25$  ps) of the MA cation according to <sup>14</sup>N-MAS spectroscopic data measured at 300 K, which was considered to be responsible for the prolonged charge carrier lifetime by two orders of magnitude via the electron–rotor interaction associated with fast reorientation of the GA cation. Such rotational reorientation dynamics of cations could contribute to stabilizing charge carriers due to polaronic behavior that screens the electrostatic interaction between charge carriers.<sup>139–141</sup> The behavior of the GA cation was found to have beneficial effects not only on charge carrier lifetime but also on ion migration.<sup>142</sup> Upon substitution of a certain amount of MA with the GA cation in MAPbI<sub>3</sub>, the activation energy of ion migration was

enhanced due to steric impediment. According to the DFT calculation for  $GA_{1-x}MA_xPbI_3$  and  $Ace_{1-x}MA_xPbI_3$  ( $Ace =$  Acetamidinium, ionic radius = 277 pm),<sup>142</sup> a strong interaction between organic cations and  $PbI_6^{4-}$  via hydrogen bonding was responsible for improvement of operational stability under heat and illumination conditions.  $GACl$ ,<sup>143</sup>  $GASCN$ ,<sup>144,145</sup> and  $AceBr$ <sup>146</sup> were attempted to improve efficiency and stability of PSCs through stabilizing crystal structure, increasing charge carrier properties, and suppressing ion migration. It is noted that the GA salts might induce low crystallinity and high Urbach tail energy when increasing the additive concentration,<sup>143,147,148</sup> which is related to the lattice strain by introducing the oversized cations in the perovskite lattice.

In addition to  $FAPbI_3$  and  $MAPbI_3$ , additive engineering with large-sized organic cations has been applied to  $CsPbI_3$ . Phase transition of  $CsPbI_3$  from the photo-inactive orthorhombic phase to photo-active cubic ( $\alpha$ -phase) or tetragonal ( $\beta$ -phase) phase occurs at high temperature (approximately 300 °C). The low tolerance factor of about 0.84 due to the small ionic radius of 167 pm for Cs cation makes it difficult for  $CsPbI_3$  to be stabilized into the  $\alpha$ - or  $\beta$ -phase. It was proposed that the large cation is expected to stabilize photo-active  $CsPbI_3$  via additive engineering. The DMA cation was found to stabilize  $\beta$ - $CsPbI_3$  at relative lower temperature,<sup>149,150</sup> where dimethylammonium iodide (DMAI) was suggested as one of the best additives for  $CsPbI_3$ . The crystallization of  $CsPbI_3$  perovskite films can be controlled by forming stable intermediate phase with the DMA cation [Fig. 4(e)],<sup>151</sup> where the volatile nature of DMA cation contributes to form stable intermediate phase of  $CsPbI_3$ -DMAI. Nearly pure  $CsPbI_3$  could be obtained at high temperature via the elimination of volatile DMA, which led to a PCE of 19.03% and long-term stability for 30 days under a dark storage condition under  $10\% \pm 5\%$  RH and at 20–25 °C. The DMAI additive was also found to be involved in the crystallization kinetics, which was beneficial for high-quality  $CsPbI_3$  perovskite films with high crystallinity and enlarged grain size. Yoon *et al.* reported that dual additives of MACl and DMAI improved further PCE of  $CsPbI_3$  based PSCs to over 20% [Fig. 4(f)].<sup>152</sup> XRD and GIWAXS of  $CsPbI_3$  perovskite films exhibited that the MACl additive was easily removed due to its volatile nature without affecting the crystal structure of  $CsPbI_3$  perovskites but contributed to the improvement of the morphology of annealed- $CsPbI_3$  films. Moreover, the long-term stability of  $CsPbI_3$ -based photovoltaic devices was also improved by using MACl. In general,  $CsPbI_3$  was problematic due to phase instability due to the low tolerance factor. Larger cations of MA or DMA than Cs were found to be beneficial for the stable  $CsPbI_3$  perovskite phase because of the improved tolerance factor. Furthermore, defects and grain boundaries were reduced by larger cations, leading to further improvement in charge carrier lifetime and transport dynamics.

Large cations with the long alkyl chain are potential for additive engineering to induce low dimensional perovskite. 2D/3D mixed perovskite was proposed for improving stability, especially against moisture. Since 2D perovskite with the long alkyl chain cation might decrease charge separation and collection due to its low conductivity, a careful design on the additive engineering is required to control 2D layer thickness. Quasi-2D approach is one of approaches to control the 2D layer thickness.<sup>153</sup> For 2D/3D hetero-structured perovskite films, a small amount of long chain organic cations should be applied so as not to deteriorate the electrical and structural properties of 3D perovskite.<sup>153–155</sup> Different 2D structures are formed depending on

additives, where mono-ammonium salts can lead to Ruddlesden-Popper 2D perovskite and di-ammonium salts can result in Dion-Jacobson 2D one. As mono-ammonium salts, phenethylammonium (PEA), 4-fluoro-phenethylammonium (FPEA), butylammonium (BA), and octylammonium (OA) cations have been suggested.<sup>156–158</sup> Long chain organic cations can induce preferred orientation of perovskite in the film. For example, the BA cation in 3D perovskite enhanced the (100) plane oriented normal to the substrate as measured by 2D x-ray diffraction (XRD),<sup>157</sup> which was found to be beneficial to increasing charge carrier lifetime. The 2D perovskite in between the vertically oriented 3D perovskite leads to type-I band alignment, which is able to act as a potential barrier for the suppression of the charge carrier recombination and the trapping at the grain boundaries. Epitaxial growth of  $FAPbI_3$  with low defect density was observed by introducing PEA and FPEA cations,<sup>156</sup> where 2D perovskite distributed in grain boundaries owing to high formation energy and low surface energy enabled 3D perovskite to enhance crystallinity and grain size via homogeneous nucleation inhibition and heterogeneous crystal growth. PEACl additive demonstrated that the photo-inactive hexagonal perovskite phase was reduced and the crystallinity of the perovskite film was improved,<sup>159</sup> which eventually reduced trap density of state (tDOS) obtained from thermal admittance spectroscopy (TAS) measurement. It was reported that n-propylammonium chloride (PACl) additive applied to  $FAPbI_3$  showed better performance and stability than a conventional MACl<sup>160</sup> in which various cationic chlorides of MA, BA, n-amylammonium (=pentylammonium, AA), and cyclopropylammonium (CPA) were also compared. The preferred orientation of perovskite was observed upon addition of 20 mol. % PACl, which was confirmed by grazing-incidence wide-angle x-ray scattering (GIWAXS) measurements [Fig. 5(a)]. As compared to MACl, PACl exhibited better charge carrier lifetime and lower Urbach energy, which led to the improvement of photovoltaic performance. According to study on the chemical bonding nature by measuring x-ray photoelectron spectroscopy (XPS), the Pb 4f XPS peak shifted to lower binding energy for the PACl-based perovskite film than for the MACl-based counterpart, which indicates that PACl passivated more effectively surface defects than MACl. The higher efficiency of 22.22% for the PACl-based PSC than the MACl-based one was attributed to better defect passivation. Furthermore, the long-term stability of PSCs was better for PACl than for MACl, which was due to the surface passivation effect of the longer alkyl chain forming the pseudo-2D structure on the surface. Relatively improved hydrophobic nature of PACl showed more stable behavior against humidity.

The Dion-Jacobson phase of  $(PDA)(MA)_{x-1}Pb_xI_{3x+1}$  was reported to be superior to the Ruddlesden-Popper phase of  $(PA)_2(MA)_{x-1}B_xX_{3x+1}$  in terms of efficiency and stability, where PA is the n-propylammonium cation and PDA is the 1,3-propyldiammonium cation.<sup>161</sup> According to the stability test under humidity (40%–70% RH), heat (85 °C), and light (1 sun illumination) conditions,  $(PDA)(MA)_3Pb_4I_{13}$  (Dion-Jacobson phase) was better than  $MAPbI_3$  and  $(PA)_{2MA}3Pb_4I_{13}$  (Ruddlesden-Popper phase). The Dion-Jacobson phase was applied to additive engineering using 1,3-diaminopropane, 1,6-diaminohexane, and 1,8-diaminoctane.<sup>162</sup> Those organic di-ammonium iodides effectively suppressed ionic defects and reinforced bonding strength of crystals through cross-linking at the grain boundary region. As a result, the PCE of 21.5% was achieved and 90% of initial efficiency was maintained for over

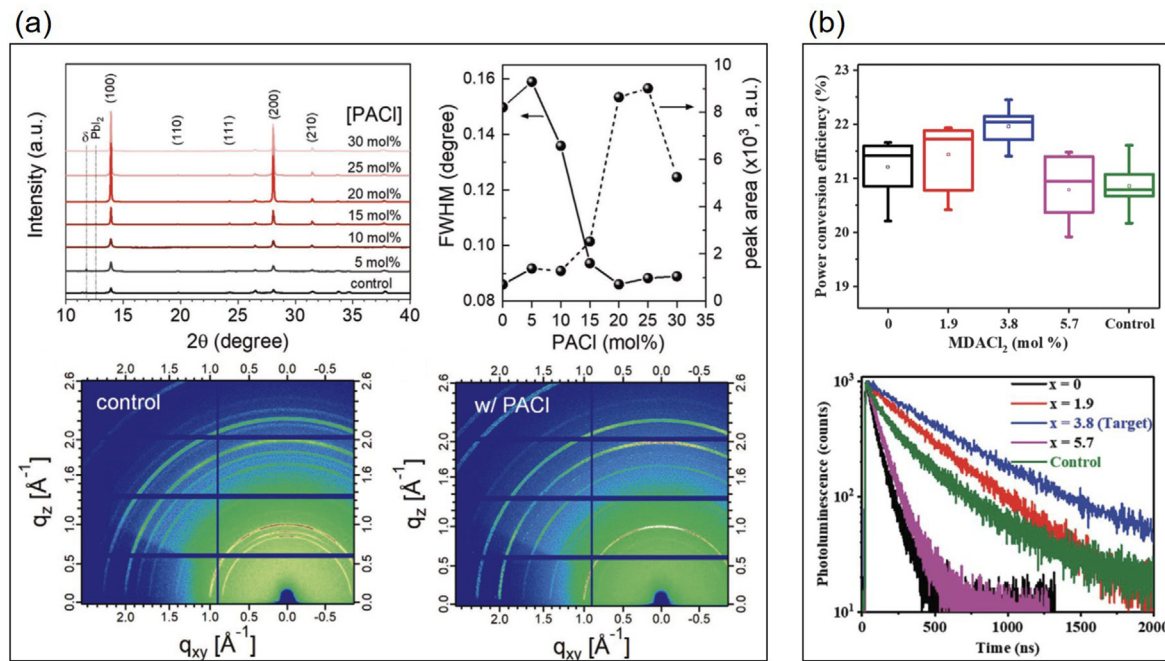


**FIG. 5.** (a) (top left) XRD patterns of FAPbI<sub>3</sub>-based perovskite films depending on the concentration of the PACI additive. (top right) Full width at half maximum (FWHM) and peak area of the (100) peak. (bottom) Two-dimensional grazing-incidence wide-angle x-ray scattering (GIWAXS) of FAPbI<sub>3</sub>-based perovskite films without (control) and with 20 mol. % PACI (w/PACI). Reproduced with permission from Zhang et al., *Adv. Energy Mater.* **11**, 2102538 (2021). Copyright 2021 Wiley-VCH GmbH.<sup>160</sup> (b) (top) Statistical PCE data of PSCs depending on the concentration of the MDACl<sub>2</sub> additive. (bottom) Time-resolved photoluminescence (TRPL) decay of perovskite films of FAPbI<sub>3</sub>:xMDACl<sub>2</sub> ( $x = 0, 1.9, 3.8$ , and  $5.7$  mol. %) and control (FAPbI<sub>3</sub>)<sub>0.95</sub>(MAPbBr<sub>3</sub>)<sub>0.05</sub>. Reproduced with permission from Min et al., *Science* **366**, 749 (2019). Copyright 2019 The American Association for the Advancement of Science.<sup>163</sup>

500 h under  $50\% \pm 5\%$  RH and 1 sun illumination. Methyleneammonium chloride (MDACl<sub>2</sub>) was used as an additive in the FAPbI<sub>3</sub> precursor solution [Fig. 5(b)],<sup>163</sup> where the grain size of FAPbI<sub>3</sub> was enlarged by the MDACl<sub>2</sub> additive and thereby a certified PCE of 23.7% was demonstrated along with improved thermal and light stability. Much enhanced carrier lifetime for the optimal 3.8 mol. % MDACl<sub>2</sub> is responsible for the improved PCE.

## 2. Inorganic cations

Unlike organic cations such as ammonium derivatives, inorganic cations may be involved in a direct incorporation into the lattice or doping because of relatively smaller ionic radius. Doping can manipulate the electrical, optical, and structural properties of semiconductor materials, and its applicability is extremely diverse depending on concentration, ionic size, and metallic nature of inorganic cations.<sup>164</sup> Monovalent alkali metal ions have been used as an additive in PSCs, especially cesium (Cs), rubidium (Rb), and potassium (K) cations. The Cs cation (ionic radius = 167 pm) is usually used for FAPbI<sub>3</sub> due to its role in the stabilizing crystal structure and enhancing phase purity by incorporate into the perovskite lattice. Study on the effect of the concentration of CsI in the precursor solution on performance and stability revealed that 3 mol. % of Cs<sup>+</sup> with respect to the FA cation led to a certified PCE of 24.4% due to the decreased trap density and the improved thermal stability at 85 °C [Fig. 6(a)].<sup>165</sup> The lattice strain was released by smaller Cs into the DMAcI<sub>2</sub> additive treated

perovskite film, which stabilized  $\alpha$ -phase FAPbI<sub>3</sub>.<sup>166</sup> A dual additive engineering with both MACl and CsCl was reported to be better than a single additive.<sup>167</sup> As can be seen in Fig. 6(b), introduction of the CsCl additive significantly improves crystallinity and reduces trap density from  $1.04 \times 10^{16} \text{ cm}^{-3}$  for only MACl additive to  $0.69 \times 10^{16} \text{ cm}^{-3}$  for dual additives with [MACl]/[CsCl] = 2. Thanks to the beneficial effect of Cs-based cationic additive, high PCE of 23.22% was achieved and an improved operational/environmental stability was also demonstrated. It is noted that the perovskite precursor solution that already include MACl has been usually used for the additional additive. When introducing the additional Cs cation in the MACl-contained perovskite precursor solution, the stabilization of the cubic phase of FAPbI<sub>3</sub> can be more effectively controlled even at a low concentration of the Cs<sup>+</sup>-containing additive because of the smaller Cs ion than the MA cation. Since methylamine, formed by thermal or chemical decomposition of the MA cation, is volatile due to the low boiling point of  $-6^\circ\text{C}$  and the high vapor pressure of 186.1 kPa at  $20^\circ\text{C}$ , introduction of Cs<sup>+</sup> can further improve thermal stability. Despite the improved thermal stability, phase segregation toward Cs-rich perovskite in the mixed FAC system is expected under the operational condition, which should be addressed appropriately. Despite stabilizing the perovskite phase by the incorporation of smaller cations such as MA<sup>+</sup> and/or Cs<sup>+</sup>, the bandgap is slightly enlarged and thus photocurrent might be lost to some extent. It is, thus, important to stabilize  $\alpha$ -phase FAPbI<sub>3</sub> with minimizing the bandgap change.

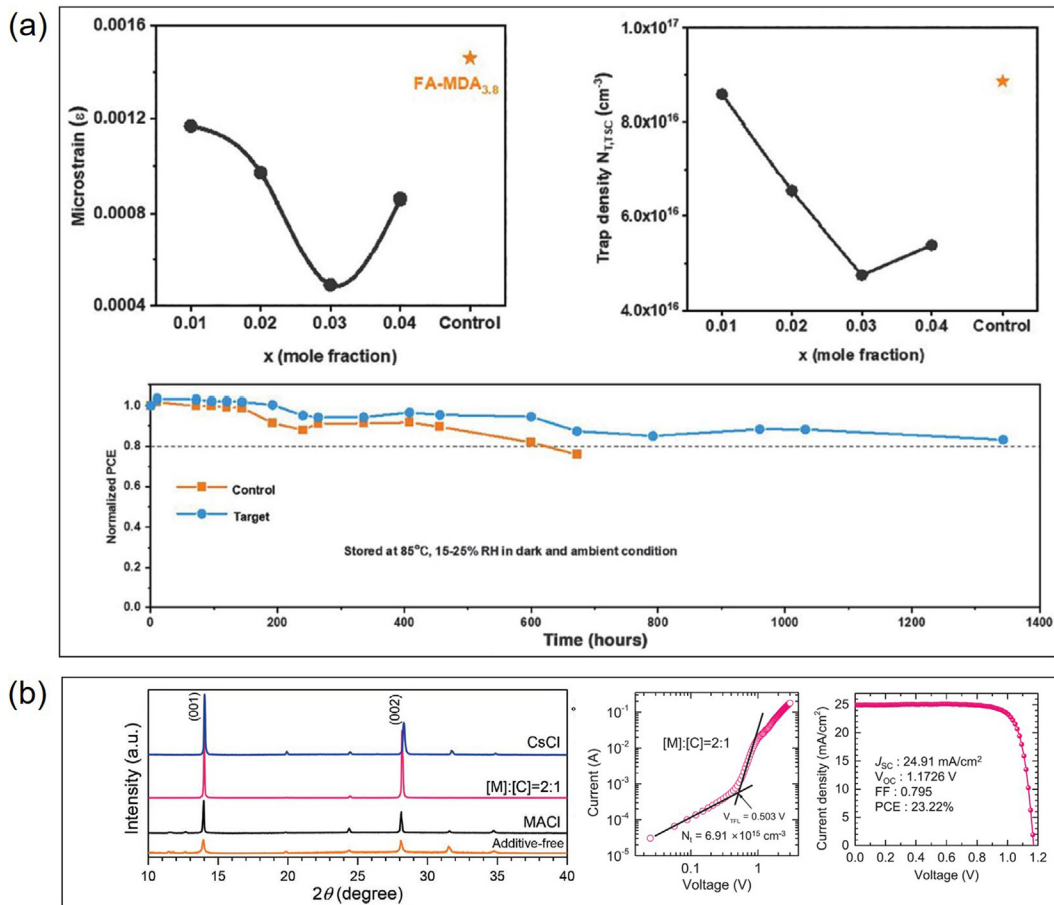


**FIG. 6.** (a) (top) Microstrain and trap density for perovskite films depending on different concentrations of the dual additive of CsI and MDACl<sub>2</sub>. (bottom) Thermal stability of PSCs without (control) or with (target) dual additive. Reproduced with permission from Kim *et al.*, Science **370**, 108 (2020). Copyright 2020 The American Association for the Advancement of Science.<sup>165</sup> (b) (left) XRD patterns for perovskite films with different additive conditions, (middle) space charge limited current (SCLC) as a function of applied voltage measured in the dark, and (right) J-V curves of best-performing PSC. Reproduced with permission from Yang and Park, Adv. Funct. Mater. **31**, 2100396 (2021). Copyright 2021 Wiley-VCH GmbH.<sup>167</sup>

The Rb cation is a possible cationic additive. Similar to the Cs cation, the monovalent Rb cation was found to improve performance and stability.<sup>168,169</sup> It was reported that the addition of RbI into the perovskite precursor solution stabilized the crystal structure due to well-controlled tolerance factor and reduced charge trap state by increasing activation energy of vacancy formation in grain interiors and grain boundaries [Fig. 7(a)].<sup>170</sup> From the total conductivity measurement using the temperature dependent galvanostatic technique, ionic conductivity can be extracted from the electronic part (plateau) in Fig. 7(b). Activation energy for ion migration obtained from ionic conductivity using the Nernst-Einstein equation was increased from 0.451 (control) to 0.579 eV (5% concentration of Rb<sup>+</sup>), which implies that the presence of 5% Rb<sup>+</sup> in the perovskite film inhibits effectively the ion (probably iodide) migration.

Most of studies have shown that the Rb cation was mixed with other cation additive to form the triple cation perovskite having FA-Cs-Rb or applied to the passivation of ETL in the n-i-p device structure, rather than the single additive source.<sup>168,171,172</sup>

It was found that mixed-cation and mixed-halide perovskite materials show phase segregation and degradation under illumination and/or heat, which is driven or accelerated by the migration of ionic species or defective impurities such as vacancies and interstitials. Potassium (K<sup>+</sup>) additive is known to be an effective cation protecting ion migration. Potassium iodide (KI) in mixed-cation (Cs-MA-FA) and mixed halide (I-Br) perovskites was found to maximize the stability and the external photoluminescence quantum efficiency (PLQE) [Fig. 8(a)].<sup>173</sup> From the time-dependent PLQE, higher PLQE along with time-independent PLQE is observed after the addition of KI, regardless of the concentration of KI. In addition, no change in the PL peak position is observed after the addition of KI ( $x = 0.4$ ), while the considerable red shift of the PL peak position is detected for the controls without KI [see the right panel in top of Fig. 8(a)]. This indicates that phase segregation toward Br-rich and I-rich perovskites is substantially suppressed by K<sup>+</sup> ion. Furthermore, both internal and external PLQE are significantly enhanced by KI additive engineering, which is an indicative of a significant suppression of non-radiative

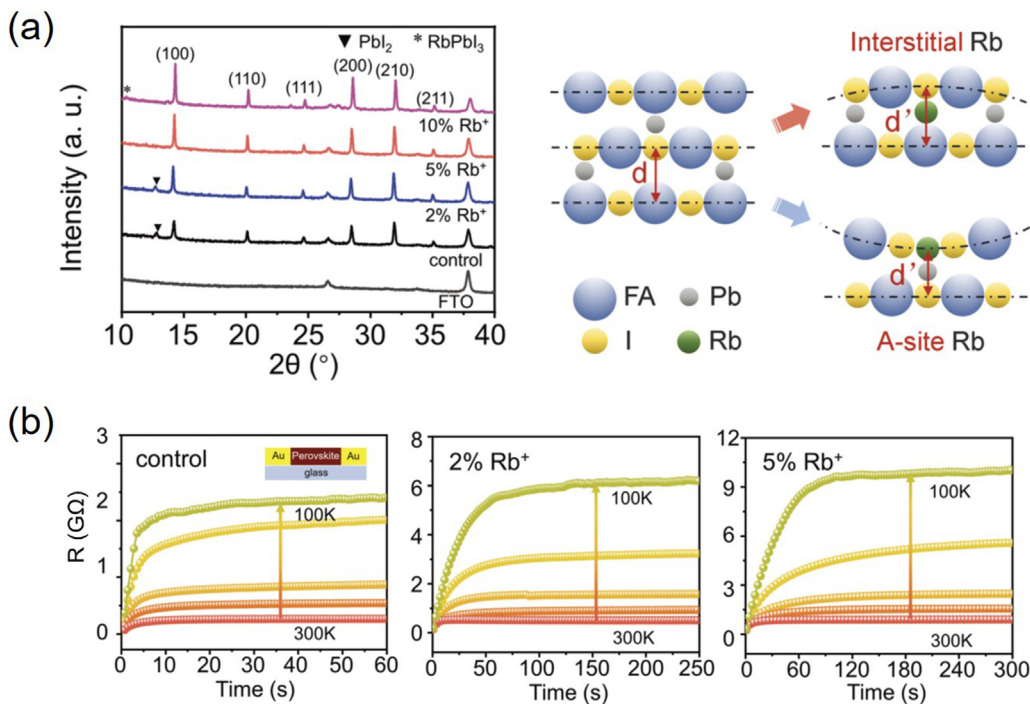


**FIG. 7.** (a) (left) XRD patterns for  $(\text{FAPbI}_3)_{0.85}(\text{MAPbBr}_3)_{0.15}$  perovskite films depending on the concentration of rubidium iodide (RbI). (right) Schematic of the change in the crystal plane distance (described as “d”) by different locations (interstitial and A-site incorporation) of the Rb cation in  $(\text{FAPbI}_3)_{0.85}(\text{MAPbBr}_3)_{0.15}$  perovskite lattices, where the crystal plane distance for the interstitial Rb case (2 mol. % RbI addition) is expanded, while that for the A-site Rb case (5 mol. % RbI addition) is reduced. (b) Galvanostatic curves for perovskite films with 0%, 2%, 5% RbI measured at different temperatures ranging from 100 to 300 K, where the resistance (R) determined from applied potential was measured as different voltage response time with a constant current of 2 pA. Reproduced with permission from Xu *et al.*, *Adv. Mater.* **34**, 2109998 (2022). Copyright 2022 Wiley-VCH GmbH.<sup>170</sup>

recombination [see the left panel in bottom of Fig. 8(a)]. The origin of the role of KI in suppression of ion migration was studied by variation of the MI concentration ( $M = \text{Li}, \text{Na}, \text{K}, \text{Rb}$  and  $\text{Cs}$ ) added in perovskite precursor solutions.<sup>174</sup> In addition, alkali metal iodides were applied to various compositions such as  $\text{MAPbI}_3$ ,  $\text{FAPbI}_3$ ,  $\text{FA}_{0.85}\text{MA}_{0.1}\text{Cs}_{0.05}\text{PbI}_{2.7}\text{Br}_{0.3}$ , and  $\text{FA}_{0.85}\text{MA}_{0.15}\text{PbI}_{2.55}\text{Br}_{0.45}$ . Negligible J-V hysteresis was observed only from KI, where the null hysteresis was achieved from all studied perovskite compositions. This indicates that  $\text{K}^+$  is universally working for the significant reduction of hysteresis for all perovskite composition. Theoretical calculation in this work revealed that  $\text{K}^+$  doping inhibits Frenkel defects with octahedrally stabilized K interstitials [Fig. 8(b)], where other alkali cations ( $\text{Li}^+, \text{Na}^+, \text{Rb}^+$ , and  $\text{Cs}^+$ ) are not suitable for octahedral interstitials according to a simple approach based on the cation/anion radius ratio. The effective protection of ion migration by the incorporation of  $\text{K}^+$  ion was found to have a beneficial effect on stability. Light soaking test shows a much better stability of PSC employing perovskite doped with  $\text{K}^+$  than the one without  $\text{K}^+$  [Fig. 8(c)].<sup>175</sup> Since Cs and/or Rb cations stabilize the perovskite phase of  $\text{FAPbI}_3$ , the incorporation of  $\text{K}^+$  into a phase stable  $\text{FAPbI}_3$  will further improve stability.

It was reported that the  $\text{Eu}^{3+}-\text{Eu}^{2+}$  ion pair was used as a redox shuttle to suppress the formation of  $\text{Pb}^0$  and  $\text{I}^0$  via additive engineering using europium acetylacetone [ $\text{Eu}(\text{acac})_3$ ], which resulted in a significant improvement of stability and efficiency of  $\text{MAPbI}_3$  PSC.<sup>176</sup>

Under operational conditions,  $\text{I}^-$  and  $\text{Pb}^{2+}$  tend to be chemically reactive to initiate the decomposition of perovskite. In this case,  $\text{I}^-$  and  $\text{Pb}^{2+}$  are expected to be oxidized and reduced to produce  $\text{I}^0$  and metallic  $\text{Pb}^0$ , where  $\text{Pb}^0$  generates a deep defect state. These deep trap states can induce the negative effect on charge carrier lifetime and diffusion length due to non-radiative recombination, which lowers the operational stability and efficiency as well. The redox shuttle plays the role in eliminating  $\text{I}^0$  and  $\text{Pb}^0$  defects, where  $\text{Eu}^{3+}$  acts as an oxidizing agent to oxidize  $\text{Pb}^0$  to  $\text{Pb}^{2+}$  and  $\text{Eu}^{2+}$  an reducing agent to reduce  $\text{I}^0$  to  $\text{I}^-$ . As compared to the unstable control device, the device with the  $\text{Eu}^{3+}-\text{Eu}^{2+}$  redox shuttle maintained 90% of the initial PCE for 8000 h.

## B. Anionic additives

### 1. Halide anions

Halide ions affect bandgap of  $\text{ABX}_3$  perovskite. In general, bandgap increases as the halide ion size decreases ( $\text{I} \rightarrow \text{Br} \rightarrow \text{Cl}$ ), which is accompanied by a decrease in phase transition temperature, for instance, from 330 K for  $\text{MAPbI}_3$  to 236 K for  $\text{MAPbBr}_3$  and from 423 K for  $\text{FAPbI}_3$  to 238 K for  $\text{FAPbBr}_3$ .<sup>45</sup> This indicates that the substitution of iodide with bromide might reduce the temperature to achieve a photo-active perovskite phase. On the other hand, the substitution of halide anion with smaller one increases bandgap, which decreases light harvesting efficiency. Therefore, a rational design is

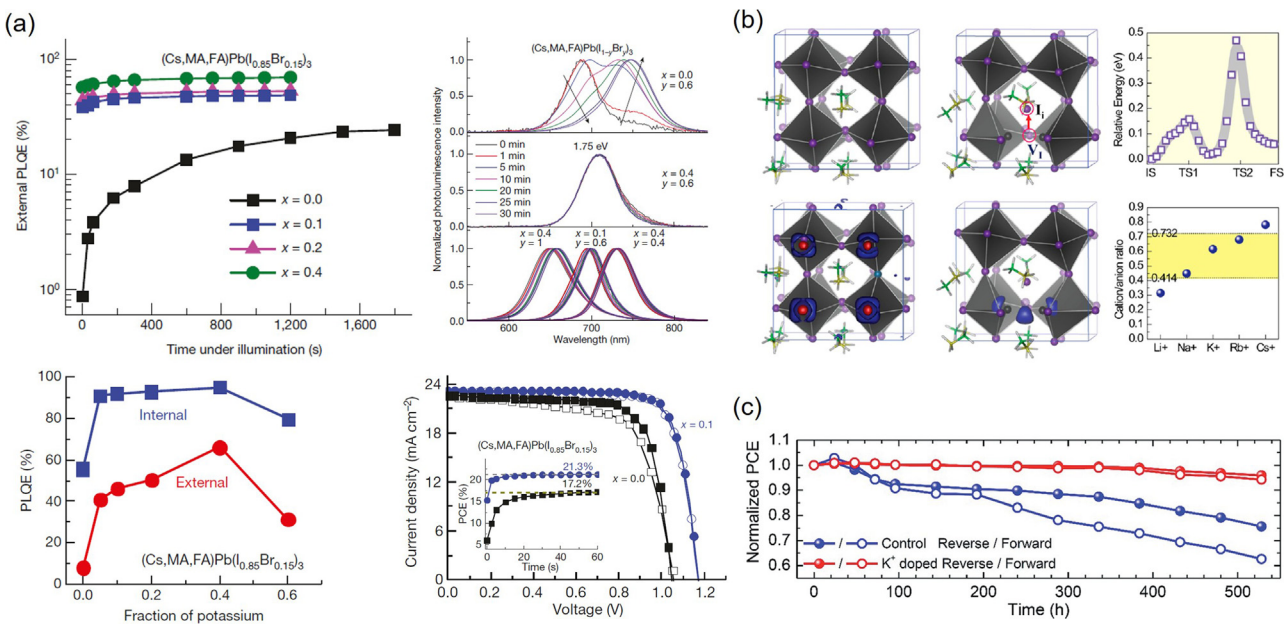


**FIG. 8.** (a) (top two panels) Photoluminescence quantum efficiency (PLQE) and steady-state photoluminescence (PL) of perovskite films. (bottom two panels) Internal and external PLQE and J-V curves (inset: time-dependent PCEs) of PSCs depending on the concentration of the KI additive. Reproduced with permission from Abdi-Jalebi *et al.*, *Nature* **555**, 497 (2018). Copyright 2018 Springer Nature.<sup>173</sup> (b) (left four panels) Simulated MAPbI<sub>3</sub> perovskite unit cells and (right top panel) relative energy profile of the iodide Frenkel defect formation. (right bottom panel) Radius ratio vs alkali metal ions. Reproduced with permission from Son *et al.*, *J. Am. Chem. Soc.* **140**, 1358 (2018). Copyright 2018 American Chemical Society.<sup>174</sup> (c) Normalized PCEs of PSCs employing perovskite layers without (control) and with KI additive measured under 1 sun illumination. Reproduced with permission from Kim *et al.*, *J. Mater. Chem. A* **7**, 18807 (2019). Copyright 2019 Royal Society of Chemistry.<sup>175</sup>

required for halide anion additive engineering to achieve both photovoltaic performance and phase stability. First, additive engineering with iodide is necessary to address the defects generated by iodide vacancies. A self-formed grain boundary healing approach was developed via non-stoichiometry precursor method.<sup>177</sup> In Fig. 9(a), the non-stoichiometry method is illustrated, where excess precursor is used instead of equimolar ratio. The excess MAI, which is regarded as an additive, in the MAI+PbI<sub>2</sub> precursor solution is found to be placed on the grain boundary, forming an *in situ* passivation layer. Conductive atomic force microscopy (c-AFM) images in Fig. 9(a) reveals that the *in situ* formed MAI layer provides a pathway for electron conduction, which is due to the ionic character of MAI. A significant reduction trap-mediated non-radiative recombination as measured by TRPL and transient absorption (TA) proved the role of the excess MAI as *in situ* grain boundary passivation. Triiodide ion (I<sub>3</sub><sup>-</sup>)-based additive engineering was reported to heal the deep-level defects of FAPbI<sub>3</sub>-based perovskite,<sup>178</sup> where the I<sub>3</sub><sup>-</sup> contained IPA solution was reacted with the pre-deposited PbI<sub>2</sub> layer via two-step process. Figure 9(b) shows deep-level transient spectroscopy (DLTS) spectra to compare the defect state before and after I<sub>3</sub><sup>-</sup> additive engineering. The control device shows three defect levels of A1, A2, and A3 placed at 0.82, 0.78, and 0.46 eV, respectively, below CB. Upon the I<sub>3</sub><sup>-</sup> treatment, A1 disappears and the defect concentration for A2 is approximately one order of magnitude reduced. This indicates that deep-level defects, probably due to interstitial Pb (Pb<sub>i</sub>) and/or antisite defects (MA<sub>Pb</sub>, Pb<sub>MA</sub>, I<sub>MA</sub>, and I<sub>Pb</sub>), are effectively passivated by the I<sub>3</sub><sup>-</sup> additive engineering. As a result, carrier lifetime is significantly enhanced as confirmed by TRPL in Fig. 9(b).

Additives having Br<sup>-</sup> anion were investigated to achieve high phase purity, smooth morphology, and high crystallinity of perovskite films. The effect of MAPbBr<sub>3</sub> additive on structural and optoelectronic properties of FAPbI<sub>3</sub> was investigated, where a small amount of MAPbBr<sub>3</sub> (~0.8 mol. %) added to the FAPbI<sub>3</sub> precursor solution exhibited an improved carrier lifetime.<sup>179</sup> Figure 10(a) shows that a gradual blue shift in the PL peak position is observed as the MAPbBr<sub>3</sub> additive concentration increases, together with a lattice contraction associated with a shift of two theta toward lower angle, which is an indicative of a gradual substitution of iodide with bromide. A stable cubic phase of FAPbI<sub>3</sub> is formed even at room temperature due to the presence of both the MA cation and bromide anion, where both ions are probably incorporated into the FA and I site, respectively. In addition, low formation temperature of cubic MAPbBr<sub>3</sub> (236 K) might contribute to lowering the temperature for cubic FAPbI<sub>3</sub>. However, an optimal concentration is required to achieve the highest carrier lifetime, which is around 0.8 mol. % as confirmed by TRPL study although an effective mobility is maximized by 2.5 mol. % MAPbBr<sub>3</sub>. The certified PCE of 25.2% with 0.0937 cm<sup>2</sup> active area was achieved by the quasi-steady state (QSS) measurement using the 0.8 mol. % MAPbBr<sub>3</sub> additive engineering [Fig. 10(b)]. This method was applied to large-area coating and led to a PCE of over 22% with 0.984 cm<sup>2</sup> active area.

Chloride in additives with the chloride anion, typically MACl, plays important role in grain growth of perovskite. Although the Cl<sup>-</sup> anion take part in the crystallization process, most of chloride remained in the wet film is readily evaporated at the annealing stage due to the relatively volatile nature. Chloride might not be placed in

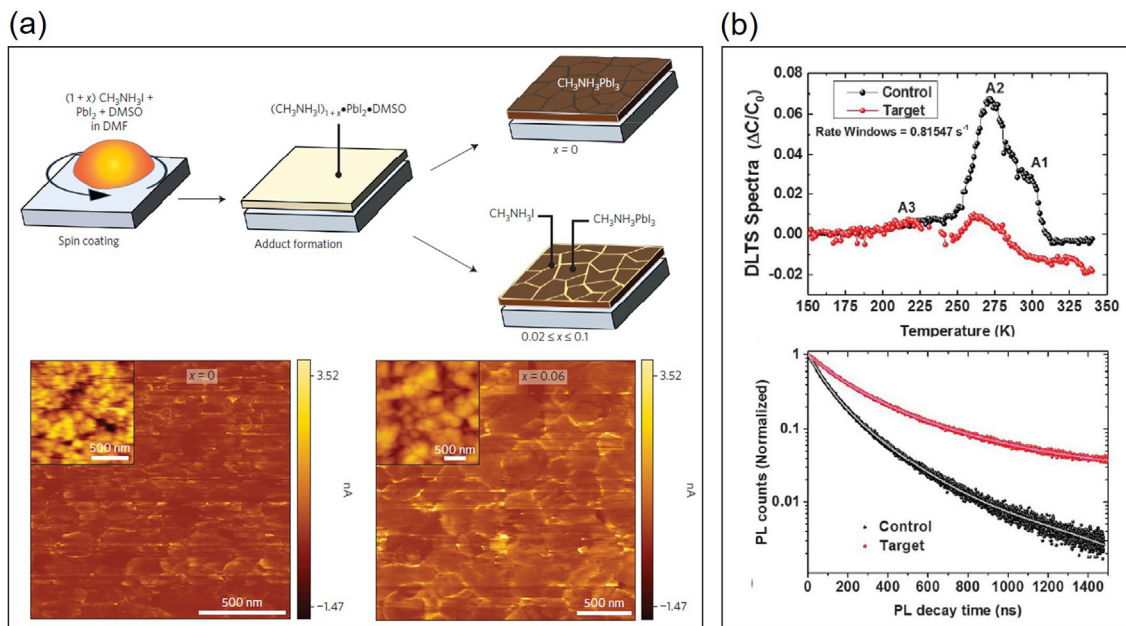


**FIG. 9.** (a) (top) Schematic illustration for the non-stoichiometry method using an excess precursor in the perovskite precursor solution. To form MAPbI<sub>3</sub> perovskite films, the perovskite coating solutions were prepared with  $(1+x)$ MAI and PbI<sub>2</sub> dissolved in DMF and DMSO solvents, where  $x$  ( $0 \leq x \leq 0.1$ ) is a molar ratio of excess MAI fraction. (bottom) c-AFM images for the surface of stoichiometric ( $x = 0$ ) and non-stoichiometric ( $x = 0.06$ ) MAPbI<sub>3</sub> perovskite film. Reproduced with permission from Son *et al.*, Nat. Energy 1, 1 (2016). Copyright 2016 Springer Nature.<sup>177</sup> (b) (top) Deep-level transient spectroscopy (DLTS) and (bottom) time-resolved photoluminescence (TRPL) spectra of perovskite films without (control) and with (target) triiodide additive engineering. In DLTS spectra, A1, A2, and A3 energy levels in terms of deep-level or semi-shallow defects are 0.78, 0.82 and 0.46 eV below the conduction band, respectively. Reproduced with permission from Yang *et al.*, Science 356, 1376 (2017). Copyright 2017 The American Association for the Advancement of Science.<sup>178</sup>

the octahedral PbI<sub>6</sub><sup>4-</sup> because of a big difference in ionic radius. However, there is possibility for the chloride ions to be placed in the axial position. In this case, lattice constant will be changed because of c-axis shrinkage due to smaller chloride size. There is no robust evidence on a substantial change in lattice constant for the MACl additive, however, was reported by far. Regarding the role of chloride in crystal growth, a systematic investigation was performed for MAPbI<sub>3</sub> perovskite.<sup>180</sup> From the TEM and electron diffraction studies on the perovskite films grown from the three different precursor solutions of (MAI + PbI<sub>2</sub>), (3MAI + PbCl<sub>2</sub>), and (MAI + 2MACl + PbI<sub>2</sub>), chloride was found to affect the complex ion equilibria in the precursor solution and thereby have influence on the nucleation of perovskite crystal. In addition, mostly absent chloride in the resulting film was suggested to be due to sublimation of MACl or decomposition of MACl into HCl and CH<sub>3</sub>NH<sub>2</sub>.

Except for MACl, FACl was investigated, where FABr and FAI were compared to understand the halide anion effect at a given cation.<sup>181</sup> In Fig. 11(a), all additives show better J-V performance than the control without additive, where the FACl additive exhibits better photovoltaic performance than the FABr and FAI ones. Lowered J<sub>SC</sub> for the FABr additive is due to the incorporation of the Br anion in the iodide site, leading to an increase in the bandgap as confirmed by blue shift in the PL peak. XRD confirms that crystallinity of FAPbI<sub>3</sub> is much improved by the FACl additive, compared to the FABr and FAI ones, which is due to the aforementioned role of chloride in nucleation. An atomically coherent interlayer formed by the reaction

between Cl-bonded SnO<sub>2</sub> ETL and Cl-additive-contained FAPbI<sub>3</sub> precursor solution was reported to have beneficial effect on performance and stability.<sup>182</sup> As can be seen in Fig. 11(b), the atomically coherent interlayer, represented by FASnCl<sub>x</sub>, is studied by the grazing-incident x-ray absorption fine structure (XAFS). After the deposition of the Cl-contained FAPbI<sub>3</sub> solution on the Cl-bearing SnO<sub>2</sub> layer, the Sn-Cl peak is detected even in the 120 °C-annealed film. This indicates that chloride ions in SnO<sub>2</sub> takes part in reaction with FA to form FASnCl<sub>x</sub>. The detailed structural analysis revealed that the interlayer is slightly deviated from the cubic FASnCl<sub>3</sub>. This technology led to a reverse scanned PCE of 25.83% and certified PCE of 25.5%, along with light soaking stability with maintaining over 90% of initial PCE for 500 h.

## 2. Non-halide anions

Non-halide anions, such as formate (HCOO<sup>-</sup>), acetate (CH<sub>3</sub>COO<sup>-</sup>), and thiocyanate (SCN<sup>-</sup>), were reported to be potential anionic additives. Since these additives contain oxygen and nitrogen with lone pair electrons, nucleation and crystal growth can be affected by these additive due to Lewis basic characteristics. For instance, methylammonium acetate (MAAc) induced by the reaction of MAI, PbI<sub>2</sub> and PbAc<sub>2</sub> to form MAPbI<sub>3</sub> perovskite film was utilized to achieve high efficiency PSCs and mini-modules via D-bar coating [Fig. 12(a)].<sup>148</sup> An adduct intermediate phase formed by the interaction between MAAc and perovskite, confirmed by the vibrational frequency shift of the acetate anion toward lower wavenumber

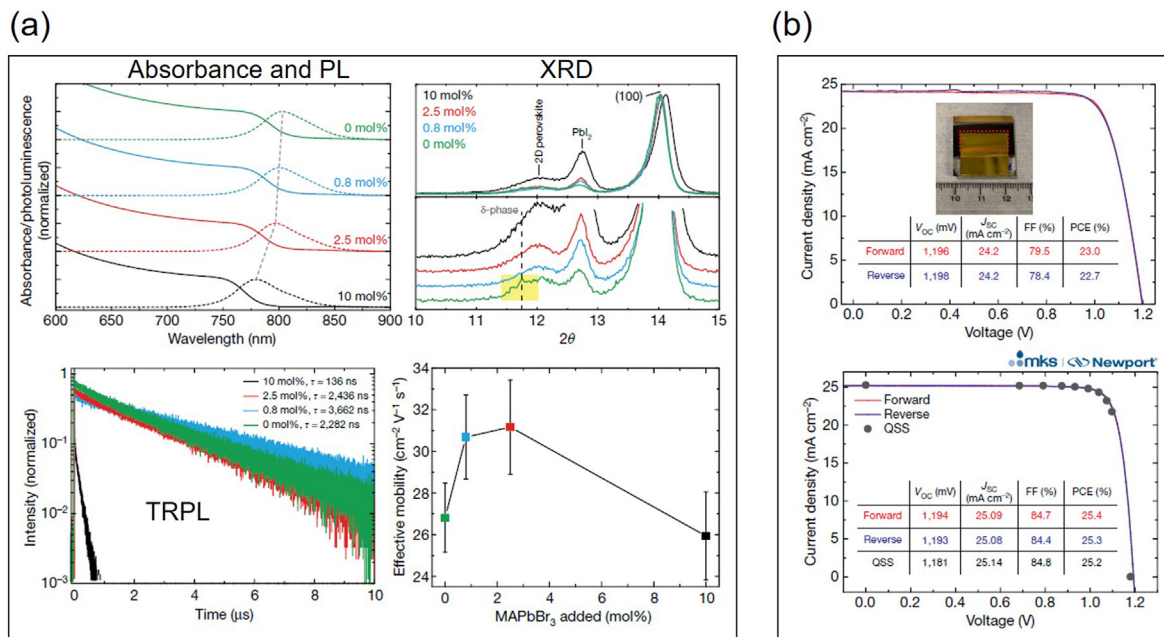


**FIG. 10.** (a) Normalized absorbance and steady-state PL spectra, XRD patterns, normalized TRPL spectra, and effective mobility of FAPbI<sub>3</sub>-based perovskite films depending on the concentration of MAPbBr<sub>3</sub> additive from 0 to 10 mol. %. In XRD patterns, the peaks of lead(II) iodide (PbI<sub>2</sub>) and (100) plane for the cubic structure of (FAPbI<sub>3</sub>)<sub>1-x</sub>(MAPbBr<sub>3</sub>)<sub>x</sub> perovskites were detected. The peak around 12.0° is indicative of the 2D perovskite formed by passivation agents on 3D perovskite films. In TRPL spectra,  $\tau$  is a carrier lifetime calculated from a mono-exponential fitting of decay curves. (b) J-V curves of the best-performing PSCs for the 0.8 mol. % MAPbBr<sub>3</sub> additive with different active areas (top: 0.984 cm<sup>2</sup>; bottom: 0.0937 cm<sup>2</sup>). Reproduced with permission from Yoo *et al.*, *Nature* **590**, 587 (2021). Copyright 2021 Springer Nature.<sup>179</sup>

[see FT-IR spectra in Fig. 12(a)], was found to play important role in large-area perovskite film formation, which suggest that the by-product MAAc acts as an anion additive. It is noted that the solvent plays also critical role in large-area coating.

For preparing the 2D perovskite film with the chemical formula of BA<sub>2</sub>MA<sub>n-1</sub>Pb<sub>n</sub>I<sub>3n+1</sub> ( $n=1-5$ ), a n-butylammonium acetate (BAAc) was used as an additive to induce a vertically oriented grains along with phase purity.<sup>183</sup> In 2D perovskite, a quantum well (QW) structure is expected due to the low bandgap inorganic sheets are separated by the large bandgap organic spacers. However, a multiple quantum wells (MQWs) due to a mixture of different  $n$  is often observed, which is problematic in the fabrication of a well-defined 2D perovskite. This problem can be solved by additive engineering. Phase-pure QW 2D perovskite film with the n-butylammonium spacer is successfully prepared by introducing BAAC, whereas the BAI precursor results in MQWs [Fig. 12(b)]. XRD patterns can distinguish QW and MQW films. The intermediate adduct formed by strongly coordinating acetate anion with perovskite precursors is responsible for phase purity, crystallinity, and well-regulated morphology. Dynamic light scattering (DLS) measurement showed the correlation between size distribution of colloidal particles in intermediate phase and quality of 2D perovskite films. Formamidinium formate (FAFo) was applied to additive engineering to control defect of FAPbI<sub>3</sub>.<sup>184</sup> The calculation of binding affinity toward iodide vacancy reveals that HCOO<sup>-</sup> ion is the strongest among the studied anions of Cl<sup>-</sup>, Br<sup>-</sup>, I<sup>-</sup>, and BF<sub>4</sub><sup>-</sup> [Fig. 12(c)]. It was verified by the ideality factor calculated from light-intensity dependence and TRPL that the charge carrier lifetime and SRH recombination can be

significantly suppressed by healing the defects via pseudo-halide anion engineering. A certified PCE of 25.2% was demonstrated via FAFo additive. Moreover, suppressed ion migration by FAFo was responsible for the improved operational stability.

SCN<sup>-</sup> is also one of the effective anionic candidates because its ionic radius of 217 pm is similar to iodide (220 pm).<sup>185,186</sup> The thiocyanate-containing additive was reported to enlarge the grain size of MAPbI<sub>3</sub> due to the delayed crystallization kinetics. The PEASCN additive is compared with PEAI and PEAI<sub>0.25</sub>SCN<sub>0.75</sub>, where PEASCN shows larger grain size because of dominant crystal growth while suppressing nucleation process [Fig. 13(a)].<sup>187</sup> The enlarged grain size by virtue of thiocyanate anion improved carrier lifetime, determined by fitting the decay rate of the product of the carrier generation yield ( $\varphi$ ), mobility ( $\mu$ ), yield product ( $\varphi\sum\mu$ ), and vertical current density [Fig. 13(a)]. It was reported that the MASCN vapor can also contribute to phase purity of FAPbI<sub>3</sub> perovskite by stabilizing the cubic phase and reducing the temperature required for phase transition.<sup>188</sup> Conversion of  $\delta$ -phase to  $\alpha$ -phase is achieved by MASCN or FASCN vapor even at temperature below the phase transition temperature. Molecular dynamic simulation supports the stabilization of the cubic phase, where adsorption of SCN<sup>-</sup> anions on the surface of  $\delta$  phase FAPbI<sub>3</sub> replaces I<sup>-</sup> and promotes the conversion of face-sharing PbI<sub>6</sub><sup>4-</sup> octahedra to corner-sharing ones [Fig. 13(b)]. It is noted that  $\delta$ -to- $\alpha$  phase transition was completed at 100 °C by either MASCN or FASCN, demonstrating clearly SCN-effect, and  $\alpha$ -phase remained after annealing at 85 °C for 500 h [Fig. 13(b)]. Under the same heat exposure condition, however, the reference FAPbI<sub>3</sub> film without MASCN vapor treatment was decomposed to PbI<sub>2</sub>. A PCE of 23.1%

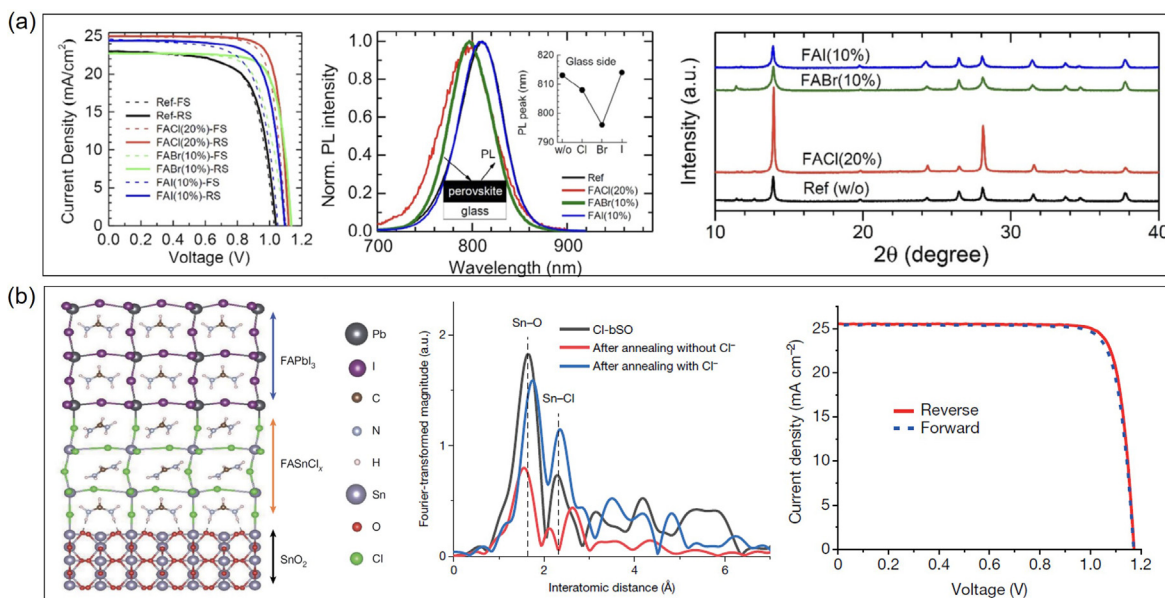


**FIG. 11.** (a) (left) J-V curves of PSCs, (middle) steady-state PL, and (right) XRD patterns of FAPbI<sub>3</sub> films depending on FAX additives ( $X = I, Br$  and  $Cl$ ). Reproduced with permission from Lyu and Park, Sol. RRL **4**, 2000331 (2020). Copyright 2021 Wiley-VCH GmbH.<sup>181</sup> (b) Simulated crystal structure for the FAPbI<sub>3</sub> perovskite film deposited on the SnO<sub>2</sub> layer with interlayer FASnCl<sub>x</sub>. Fourier-transformed radial distribution of Sn K-edge extended x-ray absorption fine structure (XAFS) spectra of Cl-bearing SnO<sub>2</sub> (Cl-bSnO) and annealed films after deposition of perovskite precursor solution with and without Cl<sup>-</sup> ion. Reverse (solid) and forward (dotted) scanned J-V curve of the best-performing PSC. Reproduced with permission from Min et al., Nature **598**, 444 (2021). Copyright 2021 Springer Nature.<sup>182</sup>

was achieved together with high light soaking stability by the additive engineering via MASCN vapor treatment.

### C. Multifunctional additives

#### 1. Molecules and polymers as Lewis base additives

Adduct approach is an effective methodology to regulate the crystallization process of the perovskite film by using Lewis base additives. Stable and well-established intermediate phase, composed of Lewis acid-base adduct, can induce homogeneous crystallization. Typically, the dimethyl sulfoxide (DMSO) polar aprotic solvent has been widely used as the Lewis base additive to form the high-quality perovskite film, regardless of the perovskite composition. The lone-pair electrons on the oxygen atom of DMSO can interact with Pb<sup>2+</sup> (Lewis acid) of perovskite precursors, which leads to a MAI-PbI<sub>2</sub>-DMSO adduct in an as-spun film.<sup>189</sup>

The Lewis base additives for adduct approach include small molecules or polymers having O-, S-, and N-atom with strong donor ability. Polar solvent additives such as DMSO are able to form a stable intermediate by the selective elimination of the solvent [such as dimethylformamide (DMF)] via anti-solvent dripping or blowing process. The adduct formation can be confirmed by FT-IR, where the stretching frequency of the oxygen-bearing functional group of the Lewis base additive (S=O for DMSO case) shifts to lower wavenumber because bond strength is weekend by adduct formation [Fig. 14(a)]. Since the adduct is not perovskite phase, the adduct film is transparent. A design rule for adduct formation was suggested to answer how to select the Lewis base.<sup>190</sup> First, there is little steric hindrance around high electron donating elements of Lewis base additives in order to

induce well-interaction with Lewis acidic species such as Pb<sup>2+</sup>. Second, Lewis bases have hydrogen bonding capability to interact well with the AX precursor for APbX<sub>3</sub> perovskite. Finally, Lewis bases are considered to be selected based on hard and soft (Lewis) acids and bases (HSAB) theory,<sup>191</sup> in order to form more stable (strong) interaction between Lewis acids and bases and to promote the metathesis reaction for conversion of adducts to the perovskite phase. DMSO is working well for MAPbI<sub>3</sub>, which might be less effective for FAPbI<sub>3</sub>. This is due to the weaker interaction between DMSO and FAI compared with the interaction between DMSO and MAI, resulting in unreacted PbI<sub>2</sub> and poor morphology. It was found that NMP (N-methyl-2-pyrrolidone) is better than DMSO for better quality of FAPbI<sub>3</sub> film due to the stronger interaction of NMP with FAI and PbI<sub>2</sub> as well as confirmed by DFT calculation and experimental results.<sup>190</sup> Nevertheless, DMSO is still used for FAPbI<sub>3</sub> especially when using the MACl additive because the Cl<sup>-</sup> Lewis base contributes more than DMSO in forming a stable intermediate.

For large-area coating, the solvent and Lewis base should be simultaneously considered, where vapor pressure is an important parameter to achieve the homogenous film on the large-area substrate. In addition, an air-blowing process in D-bar coating can replace the anti-solvent treatment used in small-area coating. The Lewis base with low vapor pressure, such as 1,3-dimethyl-3,4,5,6-tetrahydro-2(1H)-pyrimidinone (DMPU), is better than the ones (for instance, DMSO) with high vapor pressure for large-area coating employing air-knife because of non-volatility under the air-blowing process, which is beneficial for the selective removal of the solvent such as DMF [Fig. 14(b)].<sup>192</sup> XRD shows that the a robust adduct is formed by DMPU compared with those formed from other Lewis bases, which is

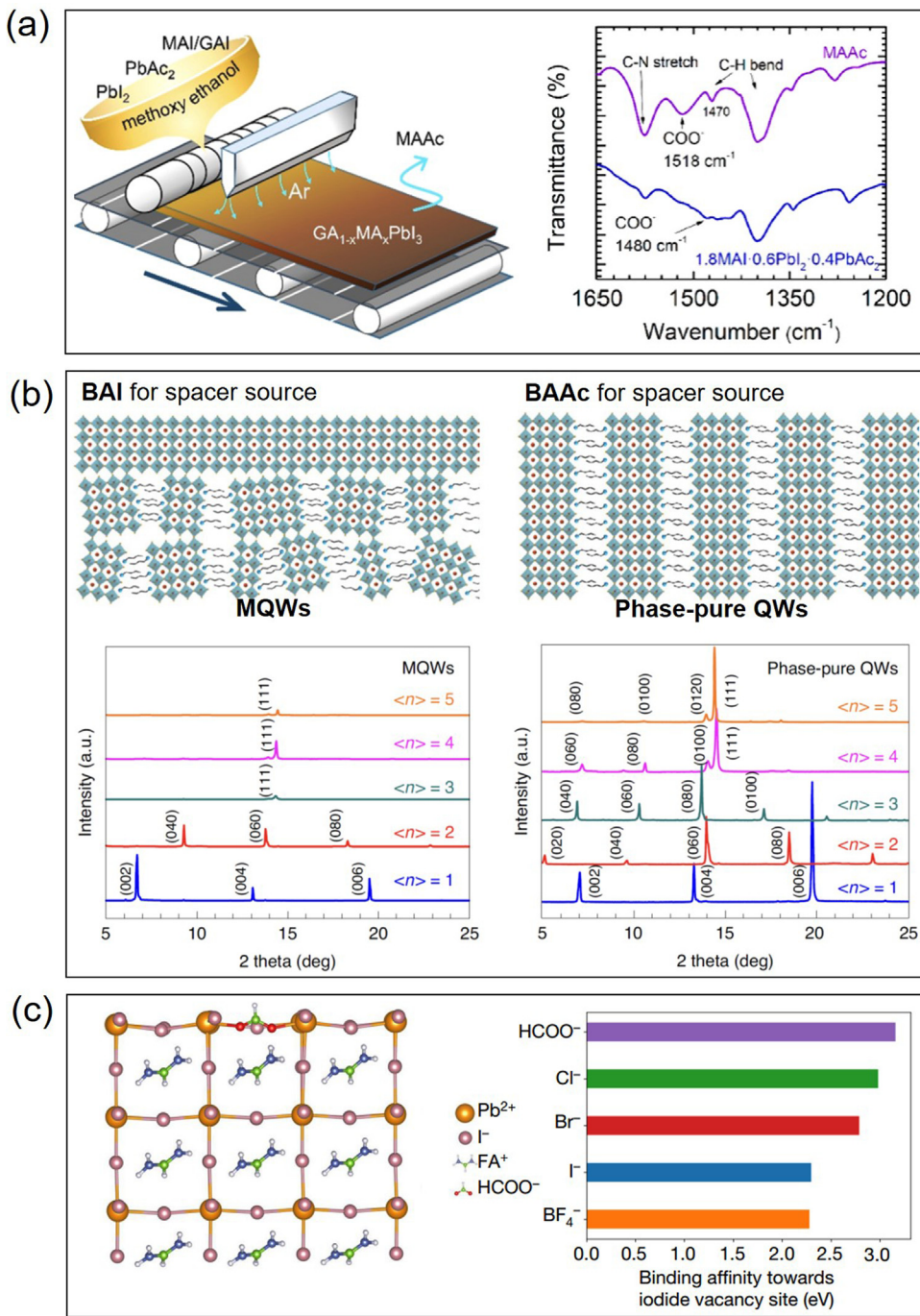


**FIG. 12.** (a) (left) A schematic illustration of D-bar coating via evaporation of the by-product MAAc. (right) FT-IR spectra of MAAc and MAAc-coordinated MAPbI<sub>3</sub> adduct powders. Reproduced with permission from Lee *et al.*, ACS Energy Lett. 4, 2393 (2019). Copyright 2021 American Chemical Society.<sup>148</sup> (b) Schematic illustration and XRD patterns of MQW and QW 2D  $\text{BA}_2\text{MA}_{n-1}\text{Pb}_n\text{I}_{3n+1}$  ( $n = 1-5$ ) perovskites induced by BAI and BAAc, respectively. Reproduced with permission from Liang *et al.*, Nat. Energy 6, 38 (2021). Copyright 2021 Springer Nature.<sup>183</sup> (c) (left) Calculated crystal structure of FAPbI<sub>3</sub> with the formate anion and (right) binding affinity toward iodide vacancy site for different anions. Reproduced with permission from Jeong *et al.*, Nature 592, 381 (2021). Copyright 2021 Springer Nature.<sup>184</sup>

related to the vapor pressure and donor number of Lewis bases [Fig. 14(b)]. This idea results in a high crystallinity large-area perovskite film and thereby high performance via a stable adduct intermediate between DMPU and precursor materials.

Unlike the polar solvent additives as Lewis bases, the Lewis base additives having solid phase at room temperature can passivate surface

and grain boundary defects. For this purpose, thiourea<sup>193</sup> and urea<sup>194</sup> were found to be useful additives. Compared with the 100% DMSO, bulk carrier lifetime is significantly improved by introduction of thiourea into the FAPbI<sub>3</sub> perovskite precursor solution because of large crystals formed via more stable adduct of FAI·PbI<sub>2</sub>·(DMSO<sub>0.8</sub>thiourea<sub>0.2</sub>) than FAI·PbI<sub>2</sub>·DMSO [Fig. 15(a)].<sup>193</sup>

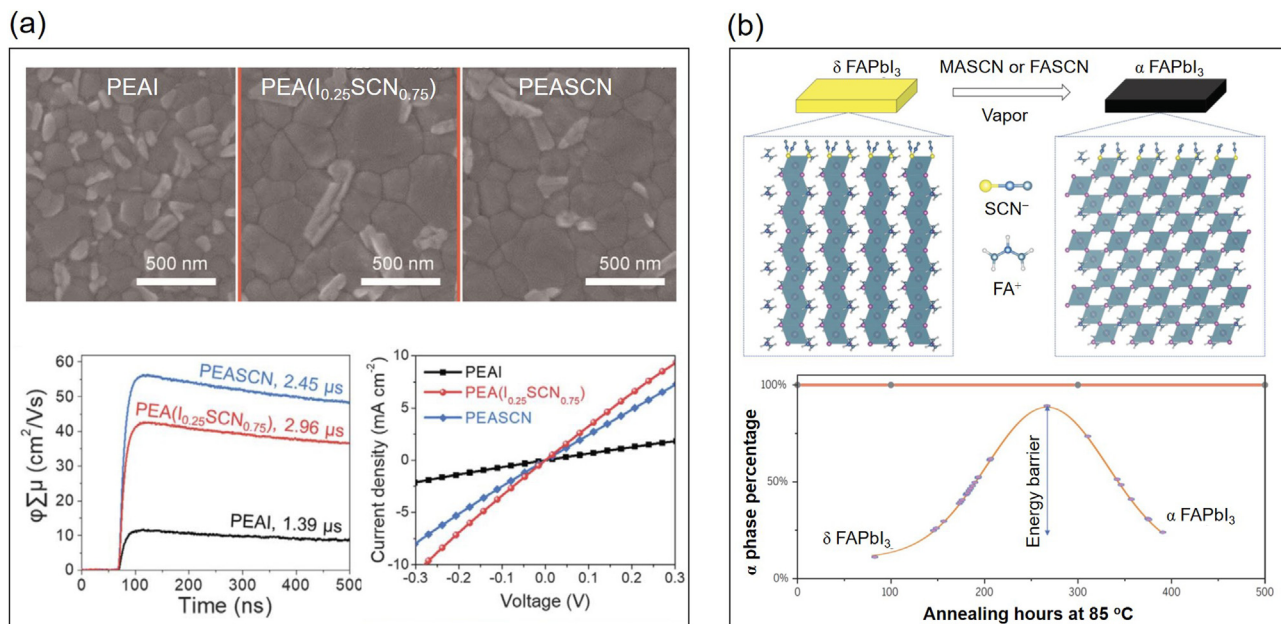


**FIG. 13.** (a) (top) Top-viewed SEM images of perovskite films formed by PEA1, PEA<sub>0.25</sub>SCN<sub>0.75</sub>, and PEASCN additives. (bottom left) Photoconductivity transient obtained by time-resolved microwave conductivity and (bottom right) vertical J-V curves of perovskite films formed from different additives. Reproduced with permission from Kim *et al.*, Science 368, 155 (2020). Copyright 2020 The American Association for the Advancement of Science.<sup>187</sup> (b) (top) Schematic illustration of  $\delta$ -to- $\alpha$  phase conversion by MASCN (or FASCN) vapor treatment on the  $\delta$ -FAPbI<sub>3</sub> film. (bottom) Annealing the vapor-treated FAPbI<sub>3</sub> film at 85 °C for 500 h. Reproduced with permission from Lu *et al.*, Science 370, 74 (2020). Copyright 2020 The American Association for the Advancement of Science.<sup>188</sup>

A highly uniform FAPbI<sub>3</sub> perovskite film is obtained via thiourea additive engineering. Introduction of urea was found to improve carrier lifetime of MAPbI<sub>3</sub> perovskite film due to both the enlarged grains and the grain boundary passivation by the solid urea layer formed on the grain boundaries [Fig. 15(b)].<sup>194</sup> The increased activation energy by the presence of urea results in an enlargement of MAPbI<sub>3</sub> grains. In addition, the remnant urea on the grain boundaries plays a passivation role in protecting charge traps.

Polymers, as well as small molecules, are candidates for additive engineering because macromolecular intermediate phase can contribute to high quality perovskite films. Polymers comprising dipolar repeating unit were reported to synergistically improve morphology and environmental durability of perovskite films.<sup>195</sup> Poly(propylene carbonate) (PPC) was used as a polymeric Lewis base additive. PPC leads to an adduct intermediate with chemical formula of MAI·PbI<sub>2</sub>·PPC in the as-deposited film, which is eventually converted to a cross-linked MAPbI<sub>3</sub> perovskite [Fig. 16(a)]. As can be seen in Fig. 16(a), inter-grain cross-linking process is assumed to be as follows. At stage I, DMSO in the intermediate phase is evaporated at low temperature of about 70 °C. Unlike small molecular additive such as propylene carbonate, nucleation occurs at slow rate in the macromolecular adduct intermediate due to the decreased nucleation probability, associated with relatively high energy barrier for nucleation. At stage II, the elevated temperature initiates crystallization of perovskite precursors and the immobilized crystals grown in the vicinity of PPC are enlarged by interconnection of grains. The interconnected grains are confirmed by TEM analysis, where an interplanar spacing of 3.1 Å is in good agreement with the (110) plane of cubic

MAPbI<sub>3</sub>. By controlling the crystallization kinetics with aid of multi-functional polymer additive, grain boundaries were effectively passivated and thereby charge carrier lifetime was prolonged. DFT calculation revealed that polymer PPC additive could passivate perovskite crystals more effectively compared to small molecules with the same functional groups. Furthermore, non-radiative recombination was significantly suppressed as measured by PL. Thanks to the effective passivation of surface defects and grain boundaries with enlarged grain size, higher PCE of 20.06% than the 17.88% without additive was achieved. Since hydrophobic nature of PPC, almost no degradation in PCE in ambient conditions was observed from the device with the PPC-embedded perovskite film.

Polyhedral oligomeric silsequioxane-poly(trifluoroethyl methacrylate)-b-poly(methyl methacrylate) (PPP) is another polymeric additive.<sup>196</sup> The core Si–O–Si cubic cage in PPP provide a stable 3D structure and poly(trifluoroethyl methacrylate) functional group has hydrophobic nature with Lewis basic characteristics [Fig. 16(b)]. Oxygen in carbonyl group in poly(trifluoroethyl methacrylate) moiety is expected to interact with Pb<sup>2+</sup> and fluorine in –CF<sub>3</sub> functional group will interact with FA or MA cation via hydrogen bonding, which induce a strong interaction between perovskite grain surface and PPP. The used PPP additive is confirmed to be placed in between perovskite grains according to TEM analysis [Fig. 16(b)], which enhances FF and V<sub>OC</sub> and stability as well. Non-radiative recombination was suppressed by the PPP polymer due to defect passivation effect as confirmed by TRPL. PPP was found to cross-link grains, resulting in large grains. PCE was enhanced from 18.62% to 22.11% after PPP treatment. Environmental stability in the dark with 40%

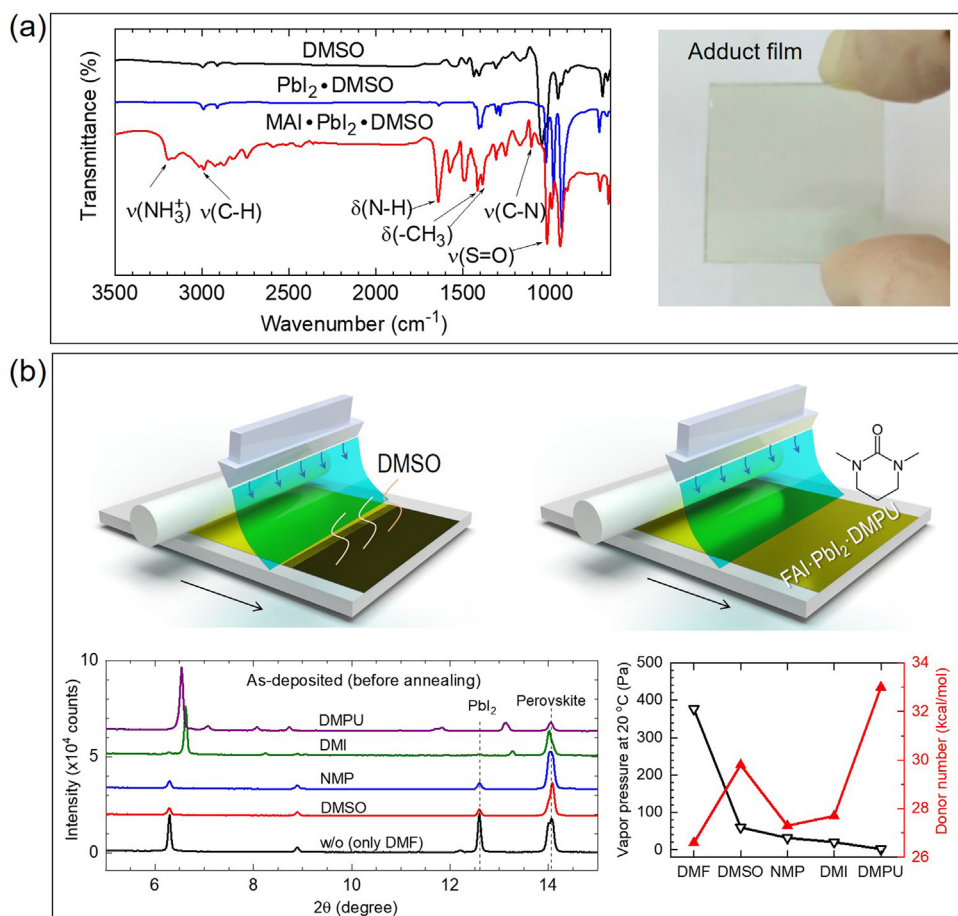


**FIG. 14.** (a) (left) FT-IR spectra for  $\text{MAI}\cdot\text{PbI}_2\text{-DMSO}$  and  $\text{PbI}_2\text{-DMSO}$  powders along with DMSO solvent as a reference. (right) Digital photo of the adduct intermediate phase of as-coated film formed from the  $\text{MAPbI}_3\text{-DMSO}$  perovskite precursor. Reproduced with permission from Ahn *et al.*, *J. Am. Chem. Soc.* **137**, 8696 (2015). Copyright 2015 American Chemical Society.<sup>189</sup> (b) (top) Schematic illustration of D-bar coating using precursor solution with DMSO and DMPU, showing a stable adduct formed by DMPU whereas an immediate formation of perovskite phase without adduct for DMSO case. (bottom left) XRD patterns of the as-deposited large-area  $\text{FAPbI}_3$  perovskite films depending on Lewis bases. DMI represents 1,3-dimethyl-2-imidazolidinone. (bottom right) Vapor pressure and donor number of Lewis bases. Reproduced with permission from Lee *et al.*, *J. Mater. Chem. A* **9**, 3018 (2021). Copyright 2021 Royal Society of Chemistry.<sup>192</sup>

relative humidity and operational stability for 1000 h at maximum power point tracking (MPPT) under 1 sun illumination at 45 °C were improved by modification with PPP. The improved environmental stability was due in part to hydrophobic nature of PPC.

## 2. Organosilane-based cross-linking additives

Organosilane-based additives were applied to passivate grain boundaries. Since the methoxy ( $-\text{OCH}_3$ ) group in organosilane can be easily cross-linked by hydrolysis to form inorganic polymer, organosilane might be beneficial to long-term stability. Effect of three different functional groups in organosilane on photovoltaic performance and stability was investigated, where 3-cyanopropyl-triethoxysilane (CPTS) with electron withdrawing CN group, trimethoxy(propyl)silane (PTS) with a weak electron donating  $-\text{CH}_3$  group and (3-mercaptopropyl)trimethoxysilane (MPTS) with a strong electron donating thiol group [Fig. 17(a)].<sup>197</sup> Two-step deposition process was utilized, where a certain amount of functionalized methoxysilane was introduced to the  $\text{PbI}_2$  precursor solution dissolved in DMSO. The deposited  $\text{PbI}_2\text{-}(silane)\text{-DMSO}$  adduct film was further treated with FA- and MA-halide solution [Fig. 17(b)]. It is interesting to see J-V curves in Fig. 17(c) that the MPTS-treated device shows improved photovoltaic parameters, whereas the CPTS-treated one declines photovoltaic performance as compared

to the control device. This indicates that photovoltaic performance is strongly dependent on functional group in organosilane, in which electron donating  $-\text{SH}$  group is beneficial for improving J-V property, that is, however decreased by electron withdrawing CN group. As compared to the untreated sample, MPTS additive improves carrier lifetime, while carrier lifetime is deteriorated by CPTS additive. Space charge limited current (SCLC) measurement showed that trap density in perovskite layers was significantly reduced from  $1.08 \times 10^{16} \text{ cm}^{-3}$  for control to  $0.65 \times 10^{16} \text{ cm}^{-3}$  for MPTS treatment, leading to the improvement of charge carrier lifetime. The prolonged charge carrier lifetime and reduced defect density resulted in a significant improvement of  $V_{\text{OC}}$  for the MPTS-based device. This is clearly indicative of passivation of undercoordinated  $\text{Pb}^{2+}$  (iodide vacancy) by electron donor. Moreover, perovskite grains are enlarged by MPTS, which is probably responsible for the improved stability. Therefore, additive engineering with organosilane substances is one of the effective strategies to improve efficiency and stability of PSCs. It is worthwhile to mention that choice of functional group depends on species of defects.

## 3. Surfactant additives

Surfactants are excellent additives for large-area coating because surface or interfacial tension can be reduced.<sup>52</sup> L- $\alpha$ -phosphatidylcholine (LP)

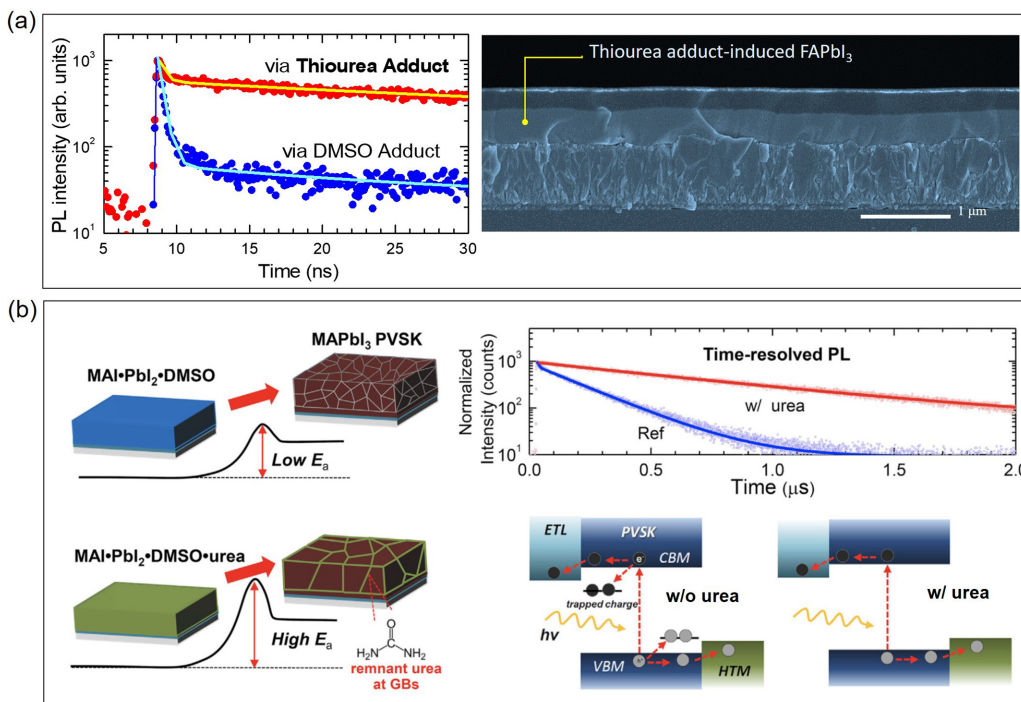


**FIG. 15.** (a) (left) TRPL spectra of FAPbI<sub>3</sub> film formed via thiourea adduct and DMSO adduct. (right) Cross-sectional SEM image of the thiourea adduct-induced FAPbI<sub>3</sub> perovskite film. Reproduced with permission from Lee *et al.*, *Acc. Chem. Res.* **49**, 311 (2016). Copyright 2016 American Chemical Society.<sup>193</sup> (b) (left) Schematic illustration of MAPbI<sub>3</sub> perovskite (PVSK) grain size evolution for only DMSO and urea-incorporated DMSO. Large grains obtained by the presence of urea are associated with the increased activation energy ( $E_a$ ). (right top) TRPL spectra for perovskite films with and without urea. (right bottom) Schematic band diagrams with and without traps for DMSO only and urea-DMSO system, respectively. Reproduced with permission from Lee *et al.*, *Chem* **3**, 290 (2017). Copyright 2017 Elsevier, Inc.<sup>194</sup>

with fatty acid residues is one of the effective surfactants, which was applied to large-area bar coating to make homogeneous perovskite film.<sup>198</sup> When the wet film is dried, the microscale fluid tends to flow toward perovskite islands [Fig. 18(a), left]. In the presence of surfactant, a surfactant gradient with a higher concentration near the perovskite islands is established by the directional fluidic flows, which decreases surface tension gradient in the same direction and thereby a Marangoni flow is formed [Fig. 18(a), right]. This Marangoni flow reduces the original fluidic flow, leading to a uniform film. For the case of using hydrophobic substrate such as poly(triaryl amine) (PTAA)-coated substrate, wetting the perovskite precursor solution is substantially improved by LP surfactant via a great reduction of the contact line, defined as the edge of droplet [Fig. 18(b)]. As a result, the surfactant additive engineering produces a uniform large area perovskite film [Fig. 18(c)].

Zwitterionic materials with hydrophobic and hydrophilic property are also one of effective additives. Tetradecyldimethyl(3-sulfopropyl)ammonium hydroxide inner salt (TAH) was reported to be an effective zwitterionic surfactant additive to form a uniform large-area perovskite film at room temperature.<sup>199</sup> As mentioned previously, TAH improves wettability of perovskite ink on the hydrophobic substrate because of the reduced contact line [Fig. 18(d)]. In addition, TAH additive promotes chemical interaction with charged defects in perovskite layer thanks to the intrinsic zwitterionic property with positive and negative ions [Fig. 18(e)], which is beneficial to passivation of defects. The 0.1 wt. % TAH in the precursor solution retards

significantly crystal growth kinetics [Fig. 18(f), left], leading to large grains. It was also confirmed from external quantum efficiency of electroluminescence (EQE<sub>EL</sub>) that the EQE<sub>EL</sub> of 0.14% at driving current equal to  $J_{SC}$  is observed by the TAH-induced perovskite film, which is much higher than the EQE<sub>EL</sub> of 0.0044% for the film without TAH [Fig. 18(f), right]. This indicates that non-radiative recombination, associated with traps, is significantly reduced by the TAH additive.

#### IV. SUMMARY AND PERSPECTIVE

Additive engineering approaches were reviewed according to additive materials and methods. Cationic, anionic, and multifunctional additives are classified, and their effects are investigated. In Table I, we summarize the enhanced photovoltaic parameters and PCE after additive engineering depending on additive types and materials. Most of the additives are found to be able to improve photovoltaic parameters of FA- and MA-based lead halide perovskites. As can be seen in Table I, the improvement of  $V_{OC}$  and FF is pronounced, rather than  $J_{SC}$ . Although defect passivation and controlling crystallization kinetics via additive engineering contribute to the improvement of  $J_{SC}$  due to the increase in charge collection efficiency, the improvement of  $V_{OC}$  and FF seems to be dominant because charge carrier lifetime and diffusion length are relatively more pronounced. Defect passivation and enlargement of grain size commonly achieved by additive engineering are responsible for such improvements in efficiency and operational stability. For stability, suppressing ion migration and stabilizing crystal

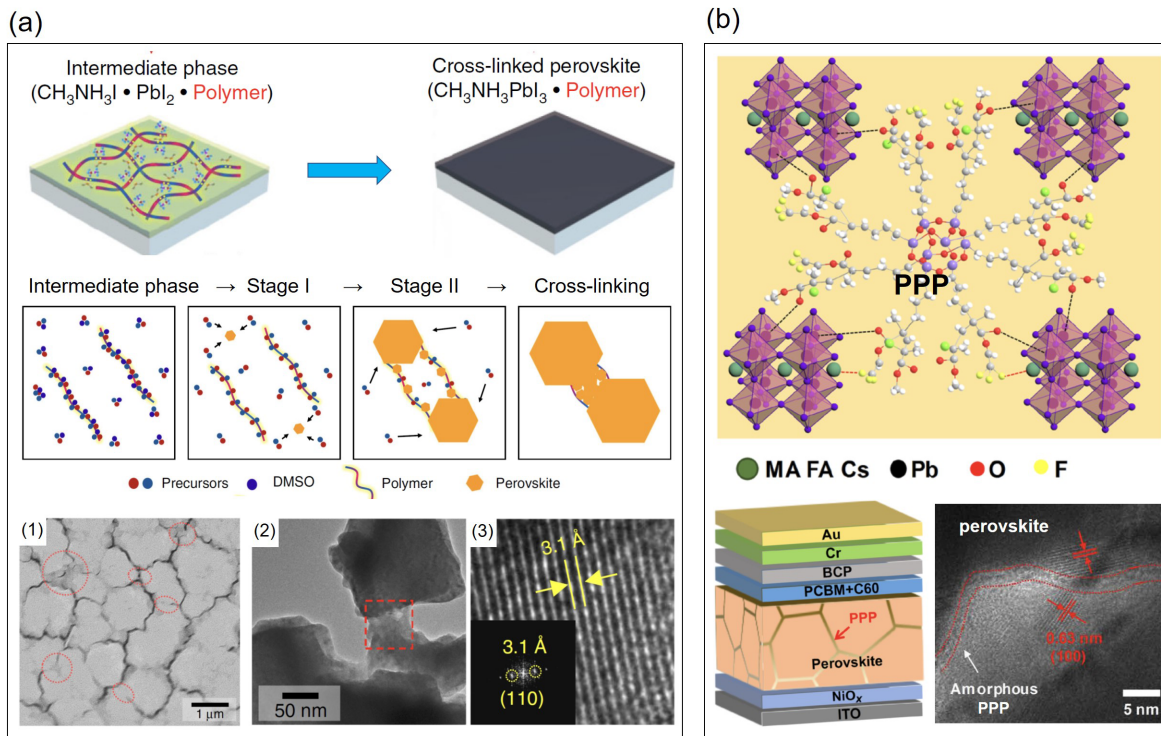


**FIG. 16.** (a) (top) Conversion of an adduct intermediate to cross-linked perovskite, where the PPC additive was embedded in the resulting film. (middle) Schematic illustration of perovskite grain growth via inter-grain connection. (bottom) (1) Top-view SEM images showing PPC between perovskite grains, (2) TEM showing interconnected perovskite grains (red dotted box) and (3) inverse fast Fourier transform (IFFT) image of the perovskite-PPC bridge region (inset is FFT analysis). Reproduced with permission from Han *et al.*, Nat. Commun. **10**, 520 (2019). Copyright 2019 Springer Nature.<sup>195</sup> (b) (top) Schematic illustration of interaction of PPP additive with perovskite, showing  $-\text{C}=\text{O} \cdots \text{Pb}^{2+}$  and  $-\text{CF}_3 \cdots \text{FA}^+$  interaction. (bottom) Device structure with PPP-induced perovskite and TEM image showing amorphous PPP between perovskite grains. Reproduced with permission from Cao *et al.*, Sci. Adv. **7**, eabg0633 (2021). Copyright 2021 The American Association for the Advancement of Science.<sup>196</sup>

structure are thermodynamically critical. Recently, PCEs higher than 25% were achieved by anionic additives containing  $\text{Cl}^-$  or  $\text{HCOO}^-$ , which underlines that the role of anions in additives should be carefully considered in additive engineering. When designing additives with small-size ions, the phase stability of perovskite should be taken into account because of the possibility of incorporation of additive ions into the perovskite lattice. Among the studied additives, chlorine (Cl)-containing additives have been frequently used. The presence of chloride is beneficial for crystal growth. In this case, residual chloride in the annealed perovskite film should be carefully controlled. Otherwise, residual chloride may have a negative effect on stability. For the cations in additives, their main roles are to improve phase stability, passivate grain boundaries, and suppress ion migration. In addition, bulk or long-chained organic cations both Ruddlesden-Popper and Dion-Jacobson precursors can enlarge grain size by suppressing heterogeneous nucleation and promoting crystal growth and mitigate ion migration and defect formation. The adduct approach via Lewis base additive engineering has been broadly applied to form high-quality perovskite films, which is a powerful technology for highly efficient and stable PSCs. Since the adduct intermediate tends to be easily decomposed due to weak acid-base interaction, careful control of the adduct intermediate is important in order to convert it to a well-defined perovskite phase. For small-molecular or polymeric additives, acidic

substances are often used. However, the unreacted additive might destabilize perovskite phase. When using multifunctional additives, each function should be carefully considered in terms of type and species of defects.

Overall, much effort has been devoted to improve the efficiency and stability of PSCs. In order to approach the theoretical performance, considerable effort has been made to minimize the grain boundaries by enlarging grain size along with high crystallinity and suppressing surface-localized defects in perovskite films. As a result, charge carrier lifetime and diffusion length were significantly enhanced. Polycrystalline perovskite has lower charge carrier lifetime ( $< 1 \mu\text{s}$ ) and diffusion length ( $> 10 \mu\text{m}$ ) and higher defect density ( $10^{16} \sim 10^{20} \text{ cm}^{-3}$ ) than single crystal one (lifetime =  $> 10 \mu\text{s}$ , diffusion length =  $\sim 100 \mu\text{m}$ , and defect density =  $10^9 \sim 10^{11} \text{ cm}^{-3}$ ).<sup>41,43,117,208,209</sup> It is one of the main limit of further improvement of efficiency of PSCs based on polycrystalline films. Currently, the certified PCE of 25.7% for PSC is almost comparable to that for silicon solar cells (26.7%). However, the stability is inferior to the silicon solar cell. There are factors affecting the operational stability of PSCs, such as moisture, oxygen, heat, light, and thermodynamic phase stability. Instability due to moisture and oxygen can be sufficiently overcome by encapsulation or lamination. Stability under illumination is concerned due to ion migration under the built-in electric field driven by the localization of generated charge carriers at surface and grain

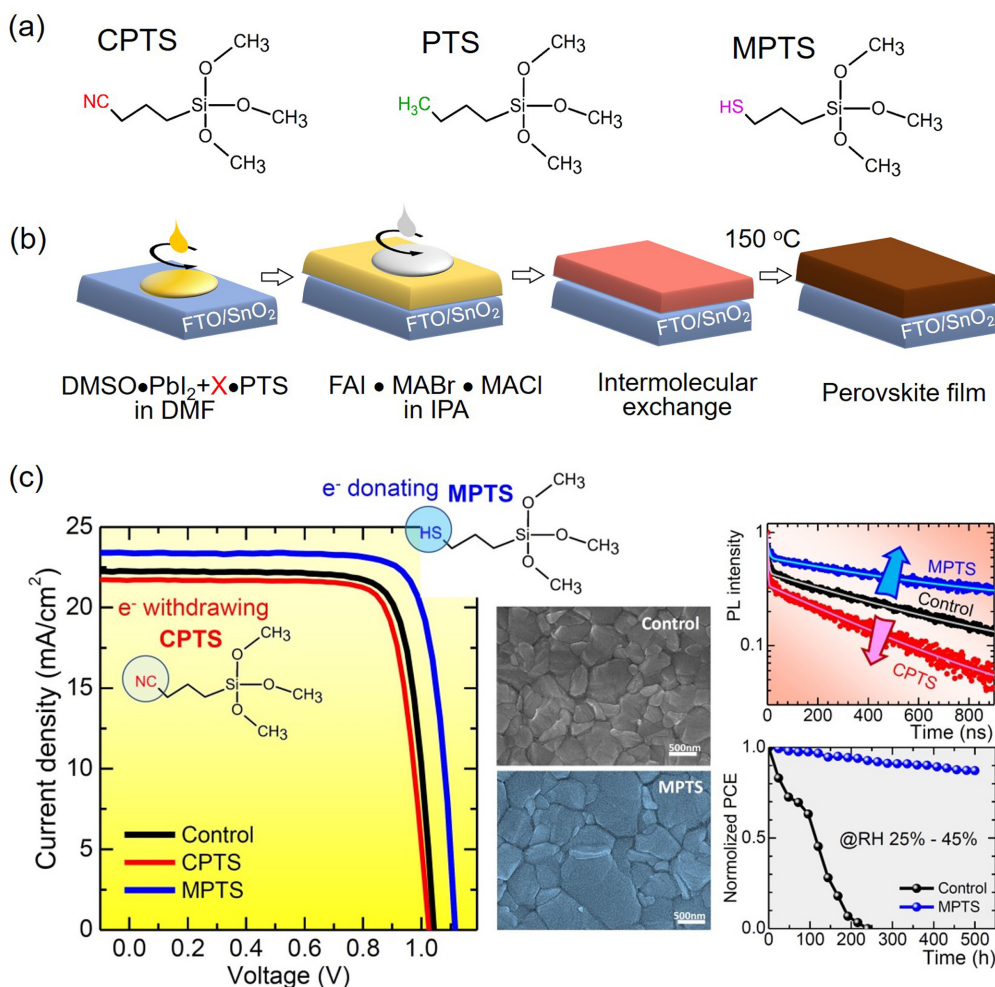


**FIG. 17.** (a) Chemical structure of cross-linking methoxysilane additives (CPTS, PTS and MPTS) with different functional groups. (b) Schematic illustration of organosilane additive engineering via two-step deposition, where cross-linking methoxysilane additives were introduced in PbI<sub>2</sub> layers (denoted as X in DMSO•PbI<sub>2</sub>+X•PTS) (c) J-V curves, SEM images, TRPL and long-term stability of PSCs or films before (control) and after additive engineering with CPTS and MPTS. For long-term stability of PSCs, the devices without or with MPTS additive were exposed under ambient conditions with 25%–45% relative humidity at room temperature in the dark. Reproduced with permission from Xie et al., ACS Energy Lett. 4, 2192 (2019). Copyright 2019 American Chemical Society.<sup>197</sup>

boundaries, which can accelerate the deterioration of perovskite films. Thermodynamic phase stability is influenced by heat and internal/external stresses due to the relative weak chemical bonding nature of M-X in perovskite materials as well as low Gibb's free energy for phase transition. Therefore, stability related to defects should be improved. The modification of A-site cationic additives seems one of the most effective strategies. The bulky organic cations are capable of mitigating ion migration by passivating surfaces and grain boundaries and simultaneously stabilizing the photo-active perovskite phase by strong hydrogen bond thanks to consisting of a lot of hydrogen atoms in the carbonaceous organic additives. Novel multifunctional additives may be developed to realize single-crystal-like perovskite films, where additive should satisfy the functions regulating defects and crystallization kinetics simultaneously. Facet manipulation and epitaxial growth of perovskite films via additive engineering can be one of the effective methods to

realize high-quality single-crystal-like perovskite films with superior features of high-charge carrier lifetime, long-diffusion length, and low-defect density. Strategies for post-treatment methods by manipulating the interface and surface engineering to suppress defects are certainly useful to maximize efficiency and stability of PSCs. Nevertheless, interface/surface engineering is better to be combined with additive engineering to further improve photovoltaic performance approaching the theoretical PCE and operational stability.

Although we have focused on Pb-based PSCs in this review, additive engineering can be extended to Sn-based and Pb/Sn-alloyed PSCs.<sup>83,210–212</sup> Since Sn can be spontaneously oxidized from 2+ to 4+, methodology for preventing the oxidation of Sn<sup>2+</sup> is of critical importance to chemically stabilize Sn-based PSCs. Additives, such as Sn powder, SnF<sub>2</sub> and GASN, have been suggested for the purpose of inhibition of oxidation.<sup>212–215</sup> Despite efforts, Sn-based PSCs are still

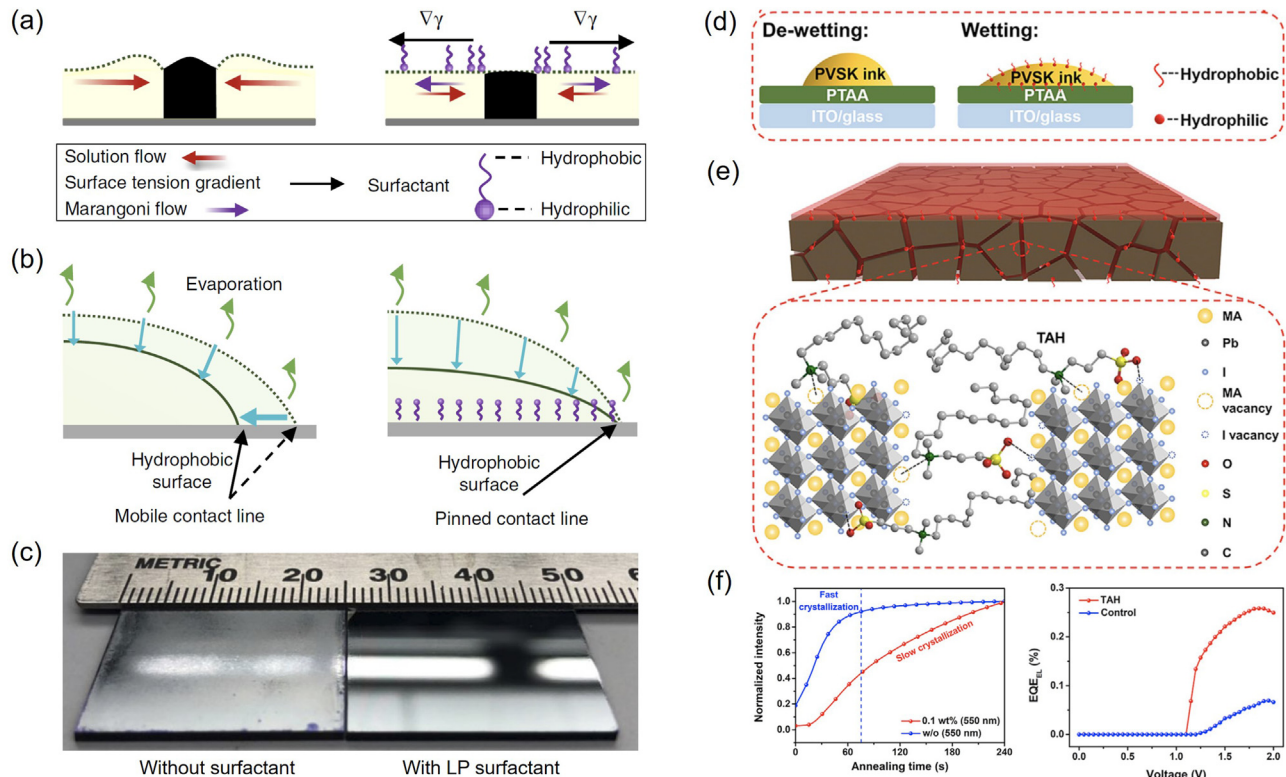


**FIG. 18.** (a) Schematic illustration of drying process showing the directional microscale fluidic behavior pointing toward perovskite islands, which is reduced by Marangoni flow formed by surface tension gradient  $\nabla\gamma$  in the presence of surfactant. (b) Contact line on the hydrophobic substrate is reduced (pinned) by surfactant. (c) Photos of large-area perovskite films formed by bar coating, showing uniform film in the presence of LP surfactant. Reproduced with permission from Deng *et al.*, Nat. Energy 3, 560 (2018). Copyright 2018 Springer Nature.<sup>198</sup> (d) Schematic illustration of de-wetting and wetting of perovskite ink droplet without and with TAH surfactant. (e) Grain boundary passivation by chemical interaction of TAH with perovskite charged defects. (f) (left) UV-visible peak intensity at 550 nm as a function of annealing time and (right) EQE<sub>EL</sub> vs applied voltage for the perovskite films with and without 0.1 wt. % TAH. Reproduced with permission from Liu *et al.*, Joule 4, 2404 (2020). Copyright 2020 Elsevier, Inc.<sup>199</sup>

**TABLE I.** Enhancement of photovoltaic parameters of  $J_{SC}$  ( $\text{mA}/\text{cm}^2$ ),  $V_{OC}$  (V), FF (%), and PCE (%) for the best-performing PSCs after additive engineering. Average values in PV parameters are denoted as asterisk. Note: FA: Formamidinium; MA: Methylammonium; AA: Acetamidinium; GA: Guanidinium. DMA: Dimethylammonium; FPEA: 4-fluorophenylammonium. PEA: Penetylammonium; BA: n-Butylammonium; PA: n-Propylammonium. DAP: 1,3-diaminopropane; MDA: Methylenediammonium; Ac: Acetate; Fo: Formate. SCN: Thiocyanate; NMP: N-Methyl-2-pyrrolidone. DMPU: N,N'-Dimethylpropyleneurea; PPC: Poly(propylene carbonate). PPP: Polyhedral oligomeric silsesquioxane-poly(trifluoroethyl methacrylate)-b-poly(methylmethacrylate). PTFEMA: Poly(2,2,2-trifluoroethyl methacrylate); DI: Dimethyl itaconate. MPTS: (3-mercaptopropyl)trimethoxysilane. TAH: Tetradecyldimethyl(3-sulfopropyl)ammonium hydroxide.

| Additive type | Additive materials         | Perovskite composition                   | PV parameter enhancement  | PCE (%)                        | Reference  |
|---------------|----------------------------|--|---|--------------------------------|------------|
| Cationic      | MACl                       | FAPbI <sub>3</sub>                       | $J_{SC}$ : 24.84 → 25.38<br>$V_{OC}$ : 1.027 → 1.130<br>FF: 77.08 → 82.02                         | 19.66 → 24.02                  | 136        |
|               | NH <sub>4</sub> I<br>GASCN | CsPbI <sub>3</sub><br>MAPbI <sub>3</sub> | $V_{OC}$ : 1.03 → 1.10<br>$J_{SC}$ : 19.62 → 21.66<br>$V_{OC}$ : 1.04 → 1.10<br>FF: 73.04 → 75.18 | 17.04 → 18.71<br>15.24 → 16.92 | 137<br>144 |
|               | AABr                       | MAPbI <sub>3</sub>                       | $J_{SC}$ : 22.20 → 23.24<br>$V_{OC}$ : 1.091 → 1.133  | 18.32 → 20.18                  | 146        |
|               | DMAI                       | CsPbI <sub>3</sub>                       | $J_{SC}$ : 17.84 → 20.09<br>$V_{OC}$ : 1.013 → 1.066<br>FF: 65.5 → 77.6                           | 11.84 → 16.62                  | 151        |

TABLE I. (Continued.)

| Additive type | Additive materials                 | Perovskite composition  | PV parameter enhancement  | PCE (%)                                 | Reference |
|---------------|------------------------------------|---|---|---|-----------|
| Anionic       | MACl                               | CsPbI <sub>3</sub>  | V <sub>OC</sub> : 1.158 → 1.198<br>FF: 79.8 → 82.5  | 19.03 → 20.37                           | 152       |
|               | FPEA <sub>2</sub> PbI <sub>4</sub> | FAPbI <sub>3</sub>  | J <sub>SC</sub> : 23.69 → 24.93<br>V <sub>OC</sub> : 1.040 → 1.101<br>FF: 64.9 → 78.8     | 15.99 → 21.64                           | 156       |
|               | BA <sub>2</sub> PbI <sub>4</sub>   | (FA,Cs) Pb(I,Br) <sub>3</sub>                                   | V <sub>OC</sub> : 1.14 → 1.18   | 16.9 → 17.2                             | 157       |
|               | PEACl                              | (C,FA,MA)PbI <sub>3</sub>                                       | V <sub>OC</sub> : 1.12 → 1.18<br>FF: 70.8 → 79.0  | 18.2 → 22.0                             | 159       |
|               | PACl                               | FAPbI <sub>3</sub>  | J <sub>SC</sub> : 22.20 → 24.79<br>V <sub>OC</sub> : 1.07 → 1.10<br>FF: 74.4 → 81.5       | 17.67 → 22.22                           | 160       |
|               | DAP                                | MAPbI <sub>3</sub>  | V <sub>OC</sub> : 1.08 → 1.18<br>FF: 77.2 → 81.7  | 18.3 → 21.7                             | 162       |
|               | MDACl <sub>2</sub>                 | FAPbI <sub>3</sub>  | J <sub>SC</sub> : 25.14 → 26.50<br>FF: 80.55 → 81.77                                      | 23.05 → 24.66                           | 163       |
|               | (MDACl <sub>2</sub> ) + (CsI)      | FAPbI <sub>3</sub>  | V <sub>OC</sub> : 1.138 → 1.168   | 24.48 → 25.17                           | 165       |
|               | (MACl) + (CsCl)                    | (FA,MA)Pb(I,Br) <sub>3</sub>                                    | V <sub>OC</sub> <sup>*</sup> : 1.064 → 1.145  | 19.66 <sup>*</sup> → 21.76 <sup>*</sup> | 167       |
|               | CsCl                               | FAPbI <sub>3</sub>  | J <sub>SC</sub> : 23.64 → 25.17<br>V <sub>OC</sub> : 1.039 → 1.122<br>FF: 75.10 → 82.45   | 18.44 → 23.28                           | 120       |
|               | KI                                 | (Cs,FA,MA,Pb(I,Br) <sub>3</sub>                                 | V <sub>OC</sub> : 1.05 → 1.17<br>FF: 73 → 79  | 17.3 → 21.5                             | 173       |
|               | KI                                 | (FA,Cs)Pb(I,Br) <sub>3</sub>                                    | V <sub>OC</sub> : 1.078 → 1.151   | 18.45 → 18.56                           | 174       |
|               | MAI                                | MAPbI <sub>3</sub>  | V <sub>OC</sub> <sup>*</sup> : 1.039 → 1.127<br>FF*: 71.4 → 77.7                          | 17.69 <sup>*</sup> → 20.70 <sup>*</sup> | 177       |
|               | I <sub>3</sub> <sup>-</sup>        | (FA,MA)Pb(I,Br) <sub>3</sub>                                    | J <sub>SC</sub> : 23.5 → 24.1<br>V <sub>OC</sub> : 1.07 → 1.10<br>FF: 80.8 → 81.9         | 20.3 → 21.6                             | 178       |
| Cationic      | FACl                               | FAPbI <sub>3</sub>  | J <sub>SC</sub> : 23.00 → 24.97<br>V <sub>OC</sub> : 1.04 → 1.12<br>FF: 0.69 → 0.81       | 16.55 → 22.51                           | 181       |
|               | FACl                               | (Cs,FA,MA) Pb(I,Br) <sub>3</sub>                                | J <sub>SC</sub> : 22.53 → 23.63<br>V <sub>OC</sub> : 1.152 → 1.183<br>FF: 71.79 → 75.21   | 18.60 → 21.02                           | 200       |
|               | FACl                               | (Cs,FA)Pb(I,Br) <sub>3</sub>                                    | J <sub>SC</sub> : 18.47 → 19.83<br>V <sub>OC</sub> : 1.15 → 1.24<br>FF: 0.71 → 0.77       | 15.07 → 19.02                           | 201       |
|               | PbCl <sub>2</sub>                  | MAPbI <sub>3</sub>  | J <sub>SC</sub> : 16.16 → 19.57<br>V <sub>OC</sub> : 1.02 → 1.06                          | 12.3 → 15.5                             | 202       |
|               | PbCl <sub>2</sub>                  | MAPbI <sub>3</sub>  | J <sub>SC</sub> : 21.74 → 23.60   | 18.36 → 20.05                           | 203       |
|               | MAAc                               | MAPbI <sub>3</sub>  | J <sub>SC</sub> : 15.001 → 20.570<br>V <sub>OC</sub> : 0.490 → 1.128<br>FF: 0.358 → 0.653 | 2.63 → 15.14                            | 148       |
|               | BAAc                               | BA <sub>2</sub> MA <sub>3</sub> Pb <sub>4</sub> I <sub>13</sub> | V <sub>OC</sub> : 1.12 → 1.31<br>FF: 66.95 → 74.07  | 13.81 → 16.25                           | 183       |
|               | FAFo                               | FAPbI <sub>3</sub>  | V <sub>OC</sub> : 1.153 → 1.189<br>FF: 80.69 → 81.70                                      | 23.92 → 25.59                           | 184       |
|               | PEAI + Pb(SCN) <sub>2</sub>        | (FA,MA,Cs)Pb(I,Br) <sub>3</sub>                                 | V <sub>OC</sub> : 1.10 → 1.15<br>FF: 74.8 → 79.8  | 16.4 → 18.9                             | 185       |

TABLE I. (Continued.)

| Additive type   | Additive materials   | Perovskite composition   | PV parameter enhancement   | PCE (%)         | Reference |
|-----------------|----------------------|--|--|-----------------|-----------|
| Multifunctional | MASN                 | FAI/MABr/MACl + PbI <sub>2</sub> /PbBr <sub>2</sub> (two-step) | V <sub>OC</sub> : 1.04 → 1.06<br>FF: 72.11 → 77.75                                       | 18.36 → 20.43   | 204       |
|                 | Pb(SCN) <sub>2</sub> | (FA,Cs)Pb(I,Br) <sub>3</sub>                                   | V <sub>OC</sub> *: 1.15 → 1.19<br>FF*: 67.55 → 75.55                                     | 13.44* → 16.46* | 205       |
|                 | NMP                  | FAPbI <sub>3</sub>   | V <sub>OC</sub> *: 0.995 → 1.032<br>FF*: 60.4 → 69.6                                     | 13.97* → 16.64* | 190       |
|                 | DMPU                 | (FA,Cs)Pb(I,Br) <sub>3</sub>                                   | J <sub>SC</sub> *: 16.73 → 23.83<br>V <sub>OC</sub> *: 0.489 → 1.089<br>FF*: 37.6 → 77.4 | 3.21* → 20.08*  | 192       |
|                 | Thiourea             | FAPbI <sub>3</sub>   | J <sub>SC</sub> *: 20.4 → 21.5<br>FF*: 0.545 → 0.659                                     | 11.5* → 13.6*   | 193       |
|                 | Urea                 | MAPbI <sub>3</sub>   | V <sub>OC</sub> : 1.048 → 1.092  | 17.34 → 18.55   | 194       |
|                 | PPC polymer          | MAPbI <sub>3</sub>   | V <sub>OC</sub> *: 1.084 → 1.129<br>FF*: 71.9 → 0.767                                    | 16.97* → 19.35* | 195       |
|                 | PPP polymer          | (Cs,FA,MA)Pb(I,Br) <sub>3</sub>                                | V <sub>OC</sub> : 1.082 → 1.131<br>FF: 77.0 → 84.1                                       | 18.62 → 22.11   | 196       |
|                 | PTFEMA polymer       | (Cs,FA,MA)Pb(I,Br) <sub>3</sub>                                | V <sub>OC</sub> : 1.08 → 1.11<br>FF: 0.734 → 0.785                                       | 17.94 → 20.18   | 206       |
|                 | DI polymer           | FAI/MAI/MACl + PbI <sub>2</sub> (two-step)                     | V <sub>OC</sub> : 1.096 → 1.145<br>FF: 77.5 → 80.8                                       | 20.9 → 23.0     | 207       |
|                 | MPTS                 | FAI/MABr/MACl + PbI <sub>2</sub> (two-step)                    | J <sub>SC</sub> : 22.25 → 23.39<br>V <sub>OC</sub> : 1.04 → 1.12                         | 18.36 → 20.81   | 197       |
|                 | TAH                  | MAPbI <sub>3</sub>   | V <sub>OC</sub> : 1.067 → 1.126<br>FF: 77.90 → 81.22                                     | 19.34 → 22.07   | 199       |

suffering from instability under the ambient air condition. Thus, discovery of additive materials is required for air-stable Sn-based PSCs.

## ACKNOWLEDGMENTS

This work was supported by the National Research Foundation of Korea (NRF) grant funded by the Ministry of Science and ICT (MSIT) of Korea under Contract No. NRF-2021R1A3B1076723 (Research Leader Program).

## AUTHOR DECLARATIONS

### Conflict of Interest

The authors have no conflicts to disclose.

### Author Contributions

**Do-Kyoung Lee:** Conceptualization (equal); Writing – original draft (equal); Writing – review & editing (equal). **Nam-Gyu Park:** Conceptualization (lead); Writing – original draft (equal); Writing – review & editing (lead).

## DATA AVAILABILITY

Data sharing is not applicable to this article as no new data were created or analyzed in this study.

## REFERENCES

- <sup>1</sup>See <https://www.nrel.gov/pv/cell-efficiency.html> for NREL best research-cell efficiency chart; accessed 30 April 2022.
- <sup>2</sup>H. Wenk and A. Bulakh, *Minerals: Their Constitution and Origin*, 2nd ed. (Cambridge University Press, 2016), p. 526.
- <sup>3</sup>N.-G. Park, *Mater. Today* **18**(2), 65–72 (2015).
- <sup>4</sup>H. S. Jung and N.-G. Park, *Small* **11**(1), 10–25 (2015).
- <sup>5</sup>J. Junquera and P. Ghosez, *Nature* **422**, 506–509 (2003).
- <sup>6</sup>E. Bousquet, M. Dawber, N. Stucki, C. Lichtensteiger, P. Hermet, S. Gariglio, J.-M. Triscone, and P. Ghosez, *Nature* **452**, 732–736 (2008).
- <sup>7</sup>I. Grinberg, D. V. West, M. Torres, G. Gou, D. M. Stein, L. Wu, G. Chen, E. M. Gallo, A. R. Akbashev, and P. K. Davies, *Nature* **503**, 509–512 (2013).
- <sup>8</sup>A. Bhalla, R. Guo, and R. Roy, *Mater. Res. Innovations* **4**(1), 3–26 (2000).
- <sup>9</sup>J. G. Bednorz and K. A. Müller, *Rev. Mod. Phys.* **60**, 585 (1988).
- <sup>10</sup>Y. Maeno, H. Hashimoto, K. Yoshida, S. Nishizaki, T. Fujita, J. Bednorz, and F. Lichtenberg, *Nature* **372**, 532–534 (1994).
- <sup>11</sup>M. Pena and J. Fierro, *Chem. Rev.* **101**(7), 1981–2018 (2001).
- <sup>12</sup>J. Suntivich, K. J. May, H. A. Gasteiger, J. B. Goodenough, and Y. Shao-Horn, *Science* **334**(6061), 1383–1385 (2011).
- <sup>13</sup>D. Weber, *Z. Naturforsch., B* **33**(12), 1443–1445 (1978).
- <sup>14</sup>D. Weber, *Z. Naturforsch., B* **33**(8), 862–865 (1978).
- <sup>15</sup>A. Kojima, K. Teshima, Y. Shirai, and T. Miyasaka, *J. Am. Chem. Soc.* **131**(17), 6050–6051 (2009).
- <sup>16</sup>J.-H. Im, C.-R. Lee, J.-W. Lee, S.-W. Park, and N.-G. Park, *Nanoscale* **3**(1), 4088–4093 (2011).
- <sup>17</sup>H.-S. Kim, C.-R. Lee, J.-H. Im, K.-B. Lee, T. Moehl, A. Marchioro, S.-J. Moon, R. Humphry-Baker, J.-H. Yum, J. E. Moser, M. Grätzel, and N.-G. Park, *Sci. Rep.* **2**(591), 1–7 (2012).

- <sup>18</sup>D.-H. Kang, S.-G. Kim, Y. C. Kim, I. T. Han, H. J. Jang, J. Y. Lee, and N.-G. Park, *ACS Energy Lett.* **5**(7), 2191–2199 (2020).
- <sup>19</sup>J.-W. Lee, Y. J. Choi, J.-M. Yang, S. Ham, S. K. Jeon, J. Y. Lee, Y.-H. Song, E. K. Ji, D.-H. Yoon, S. Seo, H. Shin, G. S. Han, H. S. Jung, D. Kim, and N.-G. Park, *ACS Nano* **11**(3), 3311–3319 (2017).
- <sup>20</sup>D.-K. Lee, Y. Shin, H. J. Jang, J.-H. Lee, K. Park, W. Lee, S. Yoo, J. Y. Lee, D. Kim, J.-W. Lee, and N.-G. Park, *ACS Energy Lett.* **6**(5), 1821–1830 (2021).
- <sup>21</sup>H. Cho, S.-H. Jeong, M.-H. Park, Y.-H. Kim, C. Wolf, C.-L. Lee, J. H. Heo, A. Sadhanala, N. Myoung, S. Yoo, S. H. Im, R. H. Friend, and T.-W. Lee, *Science* **350**(6265), 1222–1225 (2015).
- <sup>22</sup>K. Lin, J. Xing, L. N. Quan, F. De Arquer, X. Gong, J. Lu, L. Xie, W. Zhao, D. Zhang, C. Yan, W. Li, X. Liu, Y. Lu, J. Kirman, E. H. Sargent, W. Xiong, and Z. Wei, *Nature* **562**, 245–248 (2018).
- <sup>23</sup>J.-M. Yang, Y.-K. Jung, J.-H. Lee, Y. C. Kim, S.-Y. Kim, S. Seo, D.-A. Park, J.-H. Kim, S.-Y. Jeong, I.-T. Han, J.-H. Park, A. Walsh, and N.-G. Park, *Nanoscale Horiz.* **6**(12), 987–997 (2021).
- <sup>24</sup>S.-Y. Kim, J.-M. Yang, E.-S. Choi, and N.-G. Park, *Nanoscale* **11**(30), 14330–14338 (2019).
- <sup>25</sup>Z. Xiao and J. Huang, *Adv. Electron. Mater.* **2**(7), 1600100 (2016).
- <sup>26</sup>R. A. John, N. Shah, S. K. Vishwanath, S. E. Ng, B. Febriansyah, M. Jagadeeswararao, C.-H. Chang, A. Basu, and N. Mathews, *Nat. Commun.* **12**, 3681 (2021).
- <sup>27</sup>S.-Y. Kim, J.-M. Yang, E.-S. Choi, and N.-G. Park, *Adv. Funct. Mater.* **30**(27), 2002653 (2020).
- <sup>28</sup>J.-M. Yang, E.-S. Choi, S.-Y. Kim, J.-H. Kim, J.-H. Park, and N.-G. Park, *Nanoscale* **11**(13), 6453–6461 (2019).
- <sup>29</sup>Y. C. Kim, K. H. Kim, D.-Y. Son, D.-N. Jeong, J.-Y. Seo, Y. S. Choi, I. T. Han, S. Y. Lee, and N.-G. Park, *Nature* **550**, 87–91 (2017).
- <sup>30</sup>L. Dou, Y. M. Yang, J. You, Z. Hong, W.-H. Chang, G. Li, and Y. Yang, *Nat. Commun.* **5**, 5404 (2014).
- <sup>31</sup>H. Zhu, Y. Fu, F. Meng, X. Wu, Z. Gong, Q. Ding, M. V. Gustafsson, M. T. Trinh, S. Jin, and X.-Y. Zhu, *Nat. Mater.* **14**, 636–642 (2015).
- <sup>32</sup>S. A. Veldhuis, P. P. Boix, N. Yantara, M. Li, T. C. Sum, N. Mathews, and S. G. Mhaisalkar, *Adv. Mater.* **28**(32), 6804–6834 (2016).
- <sup>33</sup>S. A. Kulkarni, T. Baikie, P. P. Boix, N. Yantara, N. Mathews, and S. Mhaisalkar, *J. Mater. Chem. A* **2**(24), 9221–9225 (2014).
- <sup>34</sup>D. M. Jang, K. Park, D. H. Kim, J. Park, F. Shojaei, H. S. Kang, J.-P. Ahn, J. W. Lee, and J. K. Song, *Nano Lett.* **15**(8), 5191–5199 (2015).
- <sup>35</sup>V. D’Innocenzo, A. R. Srimath Kandada, M. De Bastiani, M. Gandini, and A. Petrozza, *J. Am. Chem. Soc.* **136**(51), 17730–17733 (2014).
- <sup>36</sup>N.-G. Park, *J. Phys. Chem. Lett.* **4**(15), 2423–2429 (2013).
- <sup>37</sup>S. Dec Wolf, J. Holovsky, S.-J. Moon, P. Löper, B. Niesen, M. Ledinsky, F.-J. Haug, J.-H. Yum, and C. Ballif, *J. Phys. Chem. Lett.* **5**(6), 1035–1039 (2014).
- <sup>38</sup>W.-J. Yin, T. Shi, and Y. Yan, *Adv. Mater.* **26**(27), 4653–4658 (2014).
- <sup>39</sup>A. Miyata, A. Mitioglu, P. Plochocka, O. Portugall, J. T.-W. Wang, S. D. Stranks, H. J. Snaith, and R. J. Nicholas, *Nat. Phys.* **11**, 582–587 (2015).
- <sup>40</sup>V. D’Innocenzo, G. Grancini, M. J. P. Alcocer, A. R. S. Kandada, S. D. Stranks, M. M. Lee, G. Lanzani, H. J. Snaith, and A. Petrozza, *Nat. Commun.* **5**, 3586 (2014).
- <sup>41</sup>Q. Dong, Y. Fang, Y. Shao, P. Mulligan, J. Qiu, L. Cao, and J. Huang, *Science* **347**(6225), 967–970 (2015).
- <sup>42</sup>S. D. Stranks, G. E. Eperon, G. Grancini, C. Menelaou, M. J. P. Alcocer, T. Leijtens, L. M. Herz, A. Petrozza, and H. J. Snaith, *Science* **342**(6156), 341–344 (2013).
- <sup>43</sup>A. A. Zhumekeenov, M. I. Saidaminov, M. A. Haque, E. Alarousu, S. P. Sarmah, B. Murali, I. Dursun, X.-H. Miao, A. L. Abdelhady, T. Wu, O. F. Mohammed, and O. M. Bakr, *ACS Energy Lett.* **1**(1), 32–37 (2016).
- <sup>44</sup>N.-G. Park, *Adv. Energy Mater.* **10**(13), 1903106 (2020).
- <sup>45</sup>J. Y. Kim, J.-W. Lee, H. S. Jung, H. Shin, and N.-G. Park, *Chem. Rev.* **120**(15), 7867–7918 (2020).
- <sup>46</sup>K. X. Steirer, P. Schulz, G. Teeter, V. Stevanovic, M. Yang, K. Zhu, and J. J. Berry, *ACS Energy Lett.* **1**(2), 360–366 (2016).
- <sup>47</sup>J. Kang and L.-W. Wang, *J. Phys. Chem. Lett.* **8**(2), 489–493 (2017).
- <sup>48</sup>H. Huang, M. I. Bodnarchuk, S. V. Kershaw, M. V. Kovalenko, and A. L. Rogach, *ACS Energy Lett.* **2**(9), 2071–2083 (2017).
- <sup>49</sup>Y. Rong, Y. Hu, A. Mei, H. Tan, M. I. Saidaminov, S. I. Seok, M. D. McGehee, E. H. Sargent, and H. Han, *Science* **361**(6408), eaat8235 (2018).
- <sup>50</sup>L. K. Ono, N.-G. Park, K. Zhu, W. Huang, and Y. Qi, *ACS Energy Lett.* **2**(8), 1749–1751 (2017).
- <sup>51</sup>N. Li, X. Niu, Q. Chen, and H. Zhou, *Chem. Soc. Rev.* **49**(22), 8235–8286 (2020).
- <sup>52</sup>N.-G. Park and K. Zhu, *Nat. Rev. Mater.* **5**, 333–350 (2020).
- <sup>53</sup>Z. Li, T. R. Klein, D. H. Kim, M. Yang, J. J. Berry, M. F. A. M. van Hest, and K. Zhu, *Nat. Rev. Mater.* **3**, 18017 (2018).
- <sup>54</sup>D. Zhao, Y. Yu, C. Wang, W. Liao, N. Shrestha, C. R. Grice, A. J. Cimaroni, L. Guan, R. J. Ellingson, K. Zhu, X. Zhao, R.-G. Xiong, and Y. Yan, *Nat. Energy* **2**, 17018 (2017).
- <sup>55</sup>G. E. Eperon, T. Leijtens, K. A. Bush, R. Prasanna, T. Green, J. T.-W. Wang, D. P. McMeekin, G. Volonakis, R. L. Milot, R. May, A. Palmstrom, D. J. Slotcavage, R. A. Belisle, J. B. Patel, E. S. Parrott, R. J. Sutton, W. Ma, F. Moghadam, B. Conings, A. Babayigit, H.-G. Boyen, S. Bent, F. Giustino, L. M. Herz, M. B. Johnston, M. D. McGehee, and H. J. Snaith, *Science* **354**(6314), 861–865 (2016).
- <sup>56</sup>J.-W. Lee and N.-G. Park, *Adv. Energy Mater.* **10**(1), 1903249 (2020).
- <sup>57</sup>L. Meng, J. You, and Y. Yang, *Nat. Commun.* **9**, 5265 (2018).
- <sup>58</sup>H.-S. Kim, J.-Y. Seo, and N.-G. Park, *ChemSusChem* **9**(18), 2528–2540 (2016).
- <sup>59</sup>C. Ma and N.-G. Park, *Chem* **6**(6), 1254–1264 (2020).
- <sup>60</sup>N.-G. Park and H. Segawa, *ACS Photonics* **5**(8), 2970–2977 (2018).
- <sup>61</sup>A. Rao and R. H. Friend, *Nat. Rev. Mater.* **2**, 17063 (2017).
- <sup>62</sup>B. Ehrler, E. Alarcón-Lladó, S. W. Tabernig, T. Veeken, E. C. Garnett, and A. Polman, *ACS Energy Lett.* **5**(9), 3029–3033 (2020).
- <sup>63</sup>S. Rühle, *Sol. Energy* **130**, 139–147 (2016).
- <sup>64</sup>J. Chen and N.-G. Park, *Adv. Mater.* **31**(47), 1803019 (2019).
- <sup>65</sup>X. Wen, Y. Feng, S. Huang, F. Huang, Y.-B. Cheng, M. Green, and A. Ho-Baillie, *J. Mater. Chem. C* **4**(4), 793–800 (2016).
- <sup>66</sup>D. Shin, B. Saparov, and D. B. Mitzi, *Adv. Energy Mater.* **7**(11), 1602366 (2017).
- <sup>67</sup>Y. Yan, K. M. Jones, C. S. Jiang, X. Z. Wu, R. Noufi, and M. M. Al-Jassim, *Physica B* **401–402**(15), 25–32 (2007).
- <sup>68</sup>M. V. Khenkin, E. A. Katz, A. Abate, G. Bardizza, J. J. Berry, C. Brabec, F. Brunetti, V. Bulović, Q. Burlingame, A. Di Carlo, R. Cheacharoen, Y.-B. Cheng, A. Colsmann, S. Cros, K. Domanski, M. Dusza, C. J. Fell, S. R. Forrest, Y. Galagan, D. Di Girolamo, M. Grätzel, A. Hagfeldt, E. von Hauff, H. Hoppe, J. Kettle, H. Köbler, M. S. Leite, S. Liu, Y.-L. Loo, J. M. Luther, C.-Q. Ma, M. Madsen, M. Manceau, M. Matheron, M. McGehee, R. Meitzner, M. K. Nazeeruddin, A. F. Nogueira, Ç. Odabaşı, A. Oshero, N.-G. Park, M. O. Reese, F. De Rossi, M. Saliba, U. S. Schubert, H. J. Snaith, S. D. Stranks, W. Tress, P. A. Troshin, V. Turkovic, S. Veenstra, I. Visoly-Fisher, A. Walsh, T. Watson, H. Xie, R. Yıldırım, S. M. Zakeeruddin, K. Zhu, and M. Lira-Cantu, *Nat. Energy* **5**, 35–49 (2020).
- <sup>69</sup>R. Brenes, D. Guo, A. Oshero, N. K. Noel, C. Eames, E. M. Hutter, S. K. Pathak, F. Niroui, R. H. Friend, M. S. Islam, H. J. Snaith, V. Bulović, T. J. Savenije, and S. D. Stranks, *Joule* **1**(1), 155–167 (2017).
- <sup>70</sup>Q. Lin, A. Armin, R. C. R. Nagiri, P. L. Burn, and P. Meredith, *Nat. Photonics* **9**, 106–112 (2015).
- <sup>71</sup>Q. Wang, B. Chen, Y. Liu, Y. Deng, Y. Bai, Q. Dong, and J. Huang, *Energy Environ. Sci.* **10**(2), 516–522 (2017).
- <sup>72</sup>B. Conings, J. Drijkoningen, N. Gauquelin, A. Babayigit, J. D’Haen, L. D’Olieslaeger, A. Ethirajan, J. Verbeeck, J. Manca, E. Mosconi, F. D. Angelis, and H.-G. Boyen, *Adv. Energy Mater.* **5**(15), 1500477 (2015).
- <sup>73</sup>M. Bag, L. A. Renna, R. Y. Adhikari, S. Karak, F. Liu, P. M. Lahti, T. P. Russell, M. T. Tuominen, and D. Venkataraman, *J. Am. Chem. Soc.* **137**(40), 13130–13137 (2015).
- <sup>74</sup>Z. Zhu, V. G. Hadjiev, Y. Rong, R. Guo, B. Cao, Z. Tang, F. Qin, Y. Li, Y. Wang, F. Hao, S. Venkatesan, W. Li, S. Baldelli, A. M. Guloy, H. Fang, Y. Hu, Y. Yao, Z. Wang, and J. Bao, *Chem. Mater.* **28**(20), 7385–7393 (2016).
- <sup>75</sup>A. A. Bakulin, O. Selig, H. J. Bakker, Y. L. A. Rezus, C. Müller, T. Glaser, R. Lovrinicic, Z. Sun, Z. Chen, A. Walsh, J. M. Frost, and T. L. C. Jansen, *J. Phys. Chem. Lett.* **6**(18), 3663–3669 (2015).
- <sup>76</sup>K. Domanski, E. A. Alharbi, A. Hagfeldt, M. Grätzel, and W. Tress, *Nat. Energy* **3**, 61–67 (2018).
- <sup>77</sup>Y. Cheng and L. Ding, *Energy Environ. Sci.* **14**(6), 3233–3255 (2021).
- <sup>78</sup>M. Becker, T. Klüner, and M. Wark, *Dalton Trans.* **46**(11), 3500–3509 (2017).

- <sup>79</sup>H. Chen, Y. Chen, T. Zhang, X. Liu, X. Wang, and Y. Zhao, *Small Struct.* **2**(5), 2000130 (2021).
- <sup>80</sup>B. Kim, J. Kim, and N. Park, *Sci. Rep.* **10**, 19635 (2020).
- <sup>81</sup>T. Miyasaka, A. Kulkarni, G. M. Kim, S. Öz, and A. K. Jena, *Adv. Energy Mater.* **10**(13), 1902500 (2020).
- <sup>82</sup>F. Zhang and K. Zhu, *Adv. Energy Mater.* **10**(13), 1902579 (2020).
- <sup>83</sup>T. Wu, D. Cui, X. Liu, X. Luo, H. Su, H. Segawa, Y. Zhang, Y. Wang, and L. Han, *Sol. RRL* **5**(5), 2100034 (2021).
- <sup>84</sup>D. T. J. Hurle, *J. Appl. Phys.* **85**(10), 6957 (1999).
- <sup>85</sup>D. T. J. Hurle, *J. Appl. Phys.* **107**(12), 121301 (2010).
- <sup>86</sup>V. M. Caselli, Z. Wei, M. M. Ackermans, E. M. Hutter, B. Ehrler, and T. J. Savenije, *ACS Energy Lett.* **5**(12), 3821–3827 (2020).
- <sup>87</sup>H. J. Queisser and E. E. Haller, *Science* **281**(5379), 945–950 (1998).
- <sup>88</sup>R. J. Stewart, C. Grieco, A. V. Larsen, G. S. Doucette, and J. B. Asbury, *J. Phys. Chem. C* **120**(23), 12392–12402 (2016).
- <sup>89</sup>H. Jin, E. Debroye, M. Keshavarz, I. G. Scheblykin, M. B. J. Roeffaers, J. Hofkens, and J. A. Steele, *Mater. Horiz.* **7**(2), 397–410 (2020).
- <sup>90</sup>T. Goudon, V. Miljanović, and C. Schmeiser, *SIAM J. Appl. Math.* **67**(4), 1183 (2007).
- <sup>91</sup>M. Kuik, L. J. A. Koster, G. A. H. Wetzelaer, and P. W. M. Blom, *Phys. Rev. Lett.* **107**, 256805 (2011).
- <sup>92</sup>M. J. Trimpl, A. D. Wright, K. Schutt, L. R. V. Buizza, Z. Wang, M. B. Johnston, H. J. Snaith, P. Müller-Buschbaum, and L. M. Herz, *Adv. Funct. Mater.* **30**(42), 2004312 (2020).
- <sup>93</sup>P. Stoltze, *J. Phys.: Condens. Matter* **6**(45), 9495 (1994).
- <sup>94</sup>S. M. Oner, E. Sezen, M. S. Yordanli, E. Karakoc, C. Deger, and I. Yavuz, *J. Phys. Chem. Lett.* **13**(1), 324–330 (2022).
- <sup>95</sup>P. Ehrhart, *J. Nucl. Mater.* **69–70**, 200–214 (1978).
- <sup>96</sup>J. Kotakoski, A. V. Krasheninnikov, U. Kaiser, and J. C. Meyer, *Phys. Rev. Lett.* **106**, 105505 (2011).
- <sup>97</sup>J. Endres, D. A. Egger, M. Kulbak, R. A. Kerner, L. Zhao, S. H. Silver, G. Hodes, B. P. Rand, D. Cahen, L. Kronik, and A. Kahn, *J. Phys. Chem. Lett.* **7**(14), 2722–2729 (2016).
- <sup>98</sup>S. X. Tao, X. Cao, and P. A. Bobbert, *Sci. Rep.* **7**, 14386 (2017).
- <sup>99</sup>R. Kikuchi, T. Nakamura, T. Kurabuchi, Y. Kaneko, Y. Kumagai, and F. Oba, *Chem. Mater.* **33**(21), 8205–8211 (2021).
- <sup>100</sup>J. Xu, A. Maxwell, M. Wei, Z. Wang, B. Chen, T. Zhu, and E. H. Sargent, *ACS Energy Lett.* **6**(12), 4220–4227 (2021).
- <sup>101</sup>H. Xue, G. Brocks, and S. Tao, *Phys. Rev. Mater.* **5**(12), 125408 (2021).
- <sup>102</sup>R. C. Kurchin, P. Gorai, T. Buonassisi, and V. Stevanoć, *Chem. Mater.* **30**(16), 5583–5592 (2018).
- <sup>103</sup>D. Meggiolaro, E. Mosconi, and F. De Angelis, *ACS Energy Lett.* **4**(3), 779–785 (2019).
- <sup>104</sup>S. G. Motti, D. Meggiolaro, S. Martani, R. Sorrentino, A. J. Barker, F. De Angelis, and A. Petrozza, *Adv. Mater.* **31**(47), 1901183 (2019).
- <sup>105</sup>J. M. Azpiroz, E. Mosconi, J. Bisquert, and F. De Angelis, *Energy Environ. Sci.* **8**(7), 2118–2127 (2015).
- <sup>106</sup>C. G. V. de Walle and J. Neugebauer, *J. Appl. Phys.* **95**(8), 3851 (2004).
- <sup>107</sup>D. Meggiolaro, D. Ricciarelli, A. A. Alasmari, F. A. S. Alasmary, and F. De Angelis, *J. Phys. Chem. Lett.* **11**(9), 3546–3556 (2020).
- <sup>108</sup>N. Li, Y. Jia, Y. Guo, and N. Zhao, *Adv. Mater.* **34**(19), 2108102 (2022).
- <sup>109</sup>Y. Yuan and J. Huang, *Acc. Chem. Res.* **49**(2), 286–293 (2016).
- <sup>110</sup>C. Eames, J. M. Frost, P. R. F. Barnes, B. C. O'Regan, A. Walsh, and M. S. Islam, *Nat. Commun.* **6**, 7497 (2015).
- <sup>111</sup>J. Xing, Q. Wang, Q. Dong, Y. Yuan, Y. Fang, and J. Huang, *Phys. Chem. Chem. Phys.* **18**(44), 30484–30490 (2016).
- <sup>112</sup>D.-H. Kang and N.-G. Park, *Adv. Mater.* **31**(34), 1805214 (2019).
- <sup>113</sup>N. Ahn, K. Kwak, M. S. Jang, H. Yoon, B. Y. Lee, J.-K. Lee, P. V. Pikhitsa, J. Byun, and M. Choi, *Nat. Commun.* **7**, 13422 (2016).
- <sup>114</sup>J. Byeon, J. Kim, J.-Y. Kim, G. Lee, K. Bang, N. Ahn, and M. Choi, *ACS Energy Lett.* **5**(8), 2580–2589 (2020).
- <sup>115</sup>Y. Liu, Z. Yang, and S. Liu, *Adv. Sci.* **5**(1), 1700471 (2018).
- <sup>116</sup>Y. Lei, Y. Chen, and S. Xu, *Matter* **4**(7), 2266–2308 (2021).
- <sup>117</sup>D. Shi, V. Adinolfi, R. Comin, M. Yuan, E. Alarousu, A. Buin, Y. Chen, S. Hoogland, A. Rothenberger, K. Katsiev, Y. Losovoj, X. Zhang, P. A. Dowben, O. F. Mohammed, E. H. Sargent, and O. M. Bakr, *Science* **347**(6221), 519–522 (2015).
- <sup>118</sup>W. Metaferia, K. L. Schulte, J. Simon, S. Johnston, and A. J. Ptak, *Nat. Commun.* **10**, 3361 (2019).
- <sup>119</sup>J. Polte, *CrystEngComm* **17**(36), 6809–6830 (2015).
- <sup>120</sup>C. B. Whitehead, S. Özkar, and R. G. Finke, *Mater. Adv.* **2**(1), 186–235 (2021).
- <sup>121</sup>J.-W. Lee, D.-K. Lee, D.-N. Jeong, and N.-G. Park, *Adv. Funct. Mater.* **29**(47), 1807047 (2019).
- <sup>122</sup>W. Nie, H. Tsai, R. Asadpour, J.-C. Blanc, A. J. Neukirch, G. Gupta, J. J. Crochet, M. Chhowalla, S. Tretiak, M. A. Alam, H.-L. Wang, and A. D. Mohite, *Science* **347**(6221), 522–525 (2015).
- <sup>123</sup>L.-Q. Xie, L. Chen, Z.-A. Nan, H.-X. Lin, T. Wang, D.-P. Zhan, J.-W. Yan, B.-W. Mao, and Z.-Q. Tian, *J. Am. Chem. Soc.* **139**(9), 3320–3323 (2017).
- <sup>124</sup>D. P. McMeekin, Z. Wang, W. Rehman, F. Pulvirenti, J. B. Patel, N. K. Noel, M. B. Johnston, S. R. Marder, L. M. Herz, and H. J. Snaith, *Adv. Mater.* **29**(29), 1607039 (2017).
- <sup>125</sup>J. S. Manser, M. I. Saidaminov, J. A. Christians, O. M. Bakr, and P. V. Kamat, *Acc. Chem. Res.* **49**(2), 330–338 (2016).
- <sup>126</sup>Y. Chen and H. Zhou, *J. Appl. Phys.* **128**(6), 060903 (2020).
- <sup>127</sup>Y. Zhou, I. Poli, D. Meggiolaro, F. D. Angelis, and A. Petrozza, *Nat. Rev. Mater.* **6**, 986–1002 (2021).
- <sup>128</sup>K. L. Svane, A. C. Forse, C. P. Grey, G. Kieslich, A. K. Cheetham, A. Walsh, and K. T. Butler, *J. Phys. Chem. Lett.* **8**(24), 6154–6159 (2017).
- <sup>129</sup>W. Gao, C. Chen, C. Ran, H. Zheng, H. Dong, Y. Xia, Y. Chen, and W. Huang, *Adv. Funct. Mater.* **30**(34), 2000794 (2020).
- <sup>130</sup>F. Ünlü, E. Jung, J. Haddad, A. Kulkarni, S. Öz, H. Choi, T. Fischer, S. Chakraborty, T. Kirchartz, and S. Mathur, *APL Mater.* **8**(7), 070901 (2020).
- <sup>131</sup>G. Kieslich, S. Sun, and A. K. Cheetham, *Chem. Sci.* **5**(12), 4712–4715 (2014).
- <sup>132</sup>G. E. Eperon, S. D. Stranks, C. Menelaou, M. B. Johnston, L. M. Herz, and H. J. Snaith, *Energy Environ. Sci.* **7**(3), 982–988 (2014).
- <sup>133</sup>M. C. Gélvez-Rueda, D. H. Cao, S. Patwardhan, N. Renaud, C. C. Stoumpos, G. C. Schatz, J. T. Hupp, O. K. Farha, T. J. Savenije, M. G. Kanatzidis, and F. C. Grozema, *J. Phys. Chem. C* **120**(30), 16577–16585 (2016).
- <sup>134</sup>S. Maheshwari, M. B. Fridriksson, S. Seal, J. Meyer, and F. C. Grozema, *J. Phys. Chem. C* **123**(23), 14652–14661 (2019).
- <sup>135</sup>J.-W. Lee, S. Tan, S. I. Seok, Y. Yang, and N.-G. Park, *Science* **375**(6583), eabj1186 (2022).
- <sup>136</sup>M. Kim, G.-H. Kim, T. K. Lee, I. W. Choi, H. W. Choi, Y. Jo, Y. J. Yoon, J. W. Kim, J. Lee, D. Huh, H. Lee, S. K. Kwak, J. Y. Kim, and D. S. Kim, *Joule* **3**(9), 2179–2192 (2019).
- <sup>137</sup>S. Tan, J. Shi, B. Yu, W. Zhao, Y. Li, Y. Li, H. Wu, Y. Luo, D. Li, and Q. Meng, *Adv. Funct. Mater.* **31**(21), 2010813 (2021).
- <sup>138</sup>D. J. Kubicki, D. Prochowicz, A. Hofstetter, M. Saski, P. Yadav, D. Bi, N. Pellet, J. Lewiński, S. M. Zakeeruddin, M. Grätzel, and L. Emsley, *J. Am. Chem. Soc.* **140**(9), 3345–3351 (2018).
- <sup>139</sup>A. J. Neukirch, W. Nie, J.-C. Blanc, K. Appavoo, H. Tsai, M. Y. Sfeir, C. Katan, L. Pedesseau, J. Even, J. J. Crochet, G. Gupta, A. D. Mohite, and S. Tretiak, *Nano Lett.* **16**(6), 3809–3816 (2016).
- <sup>140</sup>D. Meggiolaro, F. Ambrosio, E. Mosconi, A. Mahata, and F. De Angelis, *Adv. Energy Mater.* **10**(13), 1902748 (2020).
- <sup>141</sup>F. Ambrosio, D. Meggiolaro, E. Mosconi, and F. De Angelis, *ACS Energy Lett.* **4**(8), 2013–2020 (2019).
- <sup>142</sup>S. Tan, I. Yavuz, N. De Marco, T. Huang, S.-J. Lee, C. S. Choi, M. Wang, S. Nuryyeva, R. Wang, Y. Zhao, H.-C. Wang, T.-H. Han, B. Dunn, Y. Huang, J.-W. Lee, and Y. Yang, *Adv. Mater.* **32**(11), 1906995 (2020).
- <sup>143</sup>N. De Marco, H. Zhou, Q. Chen, P. Sun, Z. Liu, L. Meng, E.-P. Yao, Y. Liu, A. Schiffer, and Y. Yang, *Nano Lett.* **16**(2), 1009–1016 (2016).
- <sup>144</sup>J. Zou, W. Liu, W. Deng, G. Lei, S. Zeng, J. Xiong, H. Gu, Z. Hu, X. Wang, and J. Li, *Electrochim. Acta* **291**, 297–303 (2018).
- <sup>145</sup>N. Cheng, W. Li, M. Zhang, H. Wu, S. Sun, Z. Zhao, Z. Xiao, Z. Sun, W. Zi, and L. Fang, *Curr. Appl. Phys.* **19**(1), 25–30 (2019).
- <sup>146</sup>K. Jung, W.-S. Chae, J. W. Choi, K. C. Kim, and M.-J. Lee, *J. Energy Chem.* **59**, 755–762 (2021).
- <sup>147</sup>A. D. Jodlowski, C. Roldán-Carmona, G. Grancini, M. Salado, M. Lalaiarisoa, S. Ahmad, N. Koch, L. Camacho, G. de Miguel, and M. K. Nazeeruddin, *Nat. Energy* **2**, 972–979 (2017).
- <sup>148</sup>D.-K. Lee, D.-N. Jeong, T. K. Ahn, and N.-G. Park, *ACS Energy Lett.* **4**(10), 2393–2401 (2019).

- <sup>149</sup>J. Zhang, L. Yang, Y. Zhong, H. Hao, M. Yang, and R. Liu, *Phys. Chem. Chem. Phys.* **21**(21), 11175–11180 (2019).
- <sup>150</sup>A. R. Marshall, H. C. Sansom, M. M. McCarthy, J. H. Warby, O. J. Ashton, B. Wenger, and H. J. Snaith, *Sol. RRL* **5**(1), 2000599 (2021).
- <sup>151</sup>Y. Wang, X. Liu, T. Zhang, X. Wang, M. Kan, J. Shi, and Y. Zhao, *Angew. Chem.-Int. Ed.* **131**(46), 16844–16849 (2019).
- <sup>152</sup>S. M. Yoon, H. Min, J. B. Kim, G. Kim, K. S. Lee, and S. I. Seok, *Joule* **5**(1), 183–196 (2021).
- <sup>153</sup>J.-W. Lee, Z. Dai, T.-H. Han, C. Choi, S.-Y. Chang, S.-J. Lee, N. De Marco, H. Zhao, P. Sun, Y. Huang, and Y. Yang, *Nat. Commun.* **9**, 3021 (2018).
- <sup>154</sup>J.-W. Lee and N.-G. Park, *Light Sci. Appl.* **10**, 86 (2021).
- <sup>155</sup>T.-H. Han, J.-W. Lee, Y. J. Choi, C. Choi, S. Tan, S.-J. Lee, Y. Zhao, Y. Huang, D. Kim, and Y. Yang, *Adv. Mater.* **32**(1), 1905674 (2020).
- <sup>156</sup>J.-W. Lee, S. Tan, T.-H. Han, R. Wang, L. Zhang, C. Park, M. Yoon, C. Choi, M. Xu, M. E. Liao, S.-J. Lee, S. Nuryevya, C. Zhu, K. Huynh, M. S. Goorsky, Y. Huang, X. Pan, and Y. Yang, *Nat. Commun.* **11**, 5514 (2020).
- <sup>157</sup>Z. Wang, Q. Lin, F. P. Chmiel, N. Sakai, L. M. Herz, and H. J. Snaith, *Nat. Energy* **2**, 17135 (2017).
- <sup>158</sup>M. M. Davy, T. M. Jadel, C. Qin, B. Luyun, and G. Mina, *Sustainable Energy Fuels* **5**(1), 34–51 (2021).
- <sup>159</sup>W.-Q. Wu, P. N. Rudd, Q. Wang, Z. Yang, and J. Huang, *Adv. Mater.* **32**(28), 2000995 (2020).
- <sup>160</sup>Y. Zhang, Y. Li, L. Zhang, H. Hu, Z. Tang, B. Xu, and N.-G. Park, *Adv. Energy Mater.* **11**(47), 2102538 (2021).
- <sup>161</sup>S. Ahmad, P. Fu, S. Yu, Q. Yang, X. Liu, X. Wang, X. Wang, X. Guo, and C. Li, *Joule* **3**(3), 794–806 (2019).
- <sup>162</sup>W.-Q. Wu, Z. Yang, P. N. Rudd, Y. Shao, X. Dai, H. Wei, J. Zhao, Y. Fang, Q. Wang, Y. Liu, Y. Deng, X. Xiao, Y. Feng, and J. Huang, *Sci. Adv.* **5**(3), eaav8925 (2019).
- <sup>163</sup>H. Min, M. Kim, S.-U. Lee, H. Kim, G. Kim, K. Choi, J. H. Lee, and S. I. Seok, *Science* **366**(6466), 749–753 (2019).
- <sup>164</sup>A. Kausar, A. Sattar, C. Xu, S. Zhang, Z. Kang, and Y. Zhang, *Chem. Soc. Rev.* **50**(4), 2696–2736 (2021).
- <sup>165</sup>G. Kim, H. Min, K. S. Lee, D. Y. Lee, S. M. Yoon, and S. I. Seok, *Science* **370**, 108–112 (2020).
- <sup>166</sup>J.-W. Lee, D.-H. Kim, H.-S. Kim, S.-W. Seo, S. M. Cho, and N.-G. Park, *Adv. Energy Mater.* **5**(20), 1501310 (2015).
- <sup>167</sup>I. S. Yang and N.-G. Park, *Adv. Funct. Mater.* **31**(20), 2100396 (2021).
- <sup>168</sup>S.-H. Turren-Cruz, A. Hagfeldt, and M. Saliba, *Science* **362**(6413), 449–453 (2018).
- <sup>169</sup>M. Saliba, T. Matsui, K. Domanski, J.-Y. Seo, A. Ummadisingu, S. M. Zakeeruddin, J.-P. Correa-Baena, W. R. Tress, A. Abate, A. Hagfeldt, and M. Grätzel, *Science* **354**(6309), 206–209 (2016).
- <sup>170</sup>C. Xu, X. Chen, S. Ma, M. Shi, S. Zhang, Z. Xiong, W. Fan, H. Si, H. Wu, Z. Zhang, Q. Liao, W. Yin, Z. Kang, and Y. Zhang, *Adv. Mater.* **34**(14), 2109998 (2022).
- <sup>171</sup>J. Zhuang, P. Mao, Y. Luan, N. Chen, X. Cao, G. Niu, F. Jia, F. Wang, S. Cao, and J. Wang, *Adv. Funct. Mater.* **31**(17), 2010385 (2021).
- <sup>172</sup>Y. Hu, E. M. Hutter, P. Rieder, I. Grill, J. Hanisch, M. F. Aygüller, A. G. Hufnagel, M. Handloser, T. Bein, A. Hartschuh, K. Tvingstedt, V. Dyakonov, A. Baumann, T. J. Savenije, M. L. Petrus, and P. Docampo, *Adv. Energy Mater.* **8**(16), 1703057 (2018).
- <sup>173</sup>M. Abdi-Jalebi, Z. Andajii-Garmaroudi, S. Cacovich, C. Stavrakas, B. Philippe, J. M. Richter, M. Alsari, E. P. Booker, E. M. Hutter, A. J. Pearson, S. Lilliu, T. J. Savenije, H. Rensmo, G. Divitini, C. Ducati, R. H. Friend, and S. D. Stranks, *Nature* **555**, 497–501 (2018).
- <sup>174</sup>D.-Y. Son, S.-G. Kim, J.-Y. Seo, S.-H. Lee, H. Shin, D. Lee, and N.-G. Park, *J. Am. Chem. Soc.* **140**(4), 1358–1364 (2018).
- <sup>175</sup>S.-G. Kim, C. Li, A. Guerrero, J.-M. Yang, Y. Zhong, J. Bisquert, S. Huettner, and N.-G. Park, *J. Mater. Chem. A* **7**(32), 18807–18815 (2019).
- <sup>176</sup>L. Wang, H. Zhou, J. Hu, B. Huang, M. Sun, B. Dong, G. Zheng, Y. Huang, Y. Chen, L. Li, Z. Xu, N. Li, Z. Liu, Q. Chen, L.-D. Sun, and C.-H. Yan, *Science* **363**(6424), 265–270 (2019).
- <sup>177</sup>D.-Y. Son, J.-W. Lee, Y. J. Choi, I.-H. Jang, S. Lee, P. J. Yoo, H. Shin, N. Ahn, M. Choi, D. Kim, and N.-G. Park, *Nat. Energy* **1**, 16081 (2016).
- <sup>178</sup>W. S. Yang, B.-W. Park, E. H. Jung, N. J. Jeon, Y. C. Kim, D. U. Lee, S. S. Shin, J. Seo, E. K. Kim, J. H. Noh, and S. I. Seok, *Science* **356**(6345), 1376–1379 (2017).
- <sup>179</sup>J. J. Yoo, G. Seo, M. R. Chua, T. G. Park, Y. Lu, F. Rotermund, Y.-K. Kim, C. S. Moon, N. J. Jeon, J.-P. Correa-Baena, V. Bulović, S. S. Shin, M. G. Bawendi, and J. Seo, *Nature* **590**, 587–593 (2021).
- <sup>180</sup>S. T. Williams, F. Zuo, C.-C. Chueh, C.-Y. Liao, P.-W. Liang, and A. K.-Y. Jen, *ACS Nano* **8**(10), 10640–10654 (2014).
- <sup>181</sup>M. Lyu and N.-G. Park, *Sol. RRL* **4**(10), 2000331 (2020).
- <sup>182</sup>H. Min, D. Y. Lee, J. Kim, G. Kim, K. S. Lee, J. Kim, M. J. Paik, Y. K. Kim, K. S. Kim, M. G. Kim, T. J. Shin, and S. Il Seok, *Nature* **598**, 444–450 (2021).
- <sup>183</sup>C. Liang, H. Gu, Y. Xia, Z. Wang, X. Liu, J. Xia, S. Zuo, Y. Hu, X. Gao, W. Hui, L. Chao, T. Niu, M. Fang, H. Lu, H. Dong, H. Yu, S. Chen, X. Ran, L. Song, B. Li, J. Zhang, Y. Peng, G. Shao, J. Wang, Y. Chen, G. Xing, and W. Huang, *Nat. Energy* **6**, 38–45 (2021).
- <sup>184</sup>J. Jeong, M. Kim, J. Seo, H. Lu, P. Ahlawat, A. Mishra, Y. Yang, M. A. Hope, F. T. Eickemeyer, M. Kim, Y. J. Yoon, I. W. Choi, B. P. Darwich, S. J. Choi, Y. Jo, J. H. Lee, B. Walker, S. M. Zakeeruddin, L. Emsley, U. Rothlisberger, A. Hagfeldt, D. S. Kim, M. Grätzel, and J. Y. Kim, *Nature* **592**, 381–385 (2021).
- <sup>185</sup>D. H. Kim, C. P. Muzzillo, J. Tong, A. F. Palmstrom, B. W. Larson, C. Choi, S. P. Harvey, S. Glynn, J. B. Whitaker, F. Zhang, Z. Li, H. Lu, M. F. A. M. van Hest, J. J. Berry, L. M. Mansfield, Y. Huang, Y. Yan, and K. Zhu, *Joule* **3**(7), 1734–1745 (2019).
- <sup>186</sup>M. K. Kim, T. Jeon, H. I. Park, J. M. Lee, S. A. Nam, and S. O. Kim, *CrystEngComm* **18**(32), 6090–6095 (2016).
- <sup>187</sup>D. Kim, H. J. Jung, I. J. Park, B. W. Larson, S. P. Dunfield, C. Xiao, J. Kim, J. Tong, P. Boonmongkolras, S. G. Ji, F. Zhang, S. R. Pae, M. Kim, S. B. Kang, V. Dravid, J. J. Berry, J. Y. Kim, K. Zhu, D. H. Kim, and B. Shin, *Science* **368**(6487), 155–160 (2020).
- <sup>188</sup>H. Lu, Y. Liu, P. Ahlawat, A. Mishra, W. R. Tress, F. T. Eickemeyer, Y. Yang, F. Fu, Z. Wang, C. E. Avalos, B. I. Carlsen, A. Agarwalla, X. Zhang, X. Li, Y. Zhan, S. M. Zakeeruddin, L. Emsley, U. Rothlisberger, L. Zheng, A. Hagfeldt, and M. Grätzel, *Science* **370**(6512), eabb8985 (2020).
- <sup>189</sup>N. Ahn, D.-Y. Son, I.-H. Jang, S. M. Kang, M. Choi, and N.-G. Park, *J. Am. Chem. Soc.* **137**(27), 8696–8699 (2015).
- <sup>190</sup>J.-W. Lee, Z. Dai, C. Lee, H. M. Lee, T.-H. Han, N. De Marco, O. Lin, C. S. Choi, B. Dunn, J. Koh, D. Di Carlo, J. H. Ko, H. D. Maynard, and Y. Yang, *J. Am. Chem. Soc.* **140**(20), 6317–6324 (2018).
- <sup>191</sup>R. G. Pearson, *J. Am. Chem. Soc.* **85**(16), 3533–3539 (1963).
- <sup>192</sup>D.-K. Lee, K.-S. Lim, J.-W. Lee, and N.-G. Park, *J. Mater. Chem. A* **9**(5), 3018–3028 (2021).
- <sup>193</sup>J.-W. Lee, H.-S. Kim, and N.-G. Park, *Acc. Chem. Res.* **49**(2), 311–319 (2016).
- <sup>194</sup>J.-W. Lee, S.-H. Bae, Y.-T. Hsieh, N. De Marco, M. Wang, P. Sun, and Y. Yang, *Chem* **3**(2), 290–302 (2017).
- <sup>195</sup>T.-H. Han, J.-W. Lee, C. Choi, S. Tan, C. Lee, Y. Zhao, Z. Dai, N. De Marco, S.-J. Lee, S.-H. Bae, Y. Yuan, H. M. Lee, Y. Huang, and Y. Yang, *Nat. Commun.* **10**, 520 (2019).
- <sup>196</sup>Q. Cao, Y. Li, H. Zhang, J. Yang, J. Han, T. Xu, S. Wang, Z. Wang, B. Gao, J. Zhao, X. Li, X. Ma, S. M. Zakeeruddin, W. E. I. Sha, X. Li, and M. Grätzel, *Sci. Adv.* **7**(28), eabg0633 (2021).
- <sup>197</sup>L. Xie, J. Chen, P. Vashishtha, X. Zhao, G. S. Shin, S. G. Mhaisalkar, and N.-G. Park, *ACS Energy Lett.* **4**(9), 2192–2200 (2019).
- <sup>198</sup>Y. Deng, X. Zheng, Y. Bai, Q. Wang, J. Zhao, and J. Huang, *Nat. Energy* **3**, 560–566 (2018).
- <sup>199</sup>K. Liu, Q. Liang, M. Qin, D. Shen, H. Yin, Z. Ren, Y. Zhang, H. Zhang, P. W. K. Fong, Z. Wu, J. Huang, J. Hao, Z. Zheng, S. K. So, C.-S. Lee, X. Lu, and G. Li, *Joule* **4**(11), 2404–2425 (2020).
- <sup>200</sup>S. You, X. Xi, X. Zhang, H. Wang, P. Gao, X. Ma, S. Bi, J. Zhang, H. Zhou, and Z. Wei, *J. Mater. Chem. A* **8**(34), 17756–17764 (2020).
- <sup>201</sup>F. Yu, J. Liu, J. Huang, P. Xu, C.-H. Li, Y.-X. Zheng, H. Tan, and J.-L. Zuo, *Sol. RRL* **6**(2), 2100906 (2022).
- <sup>202</sup>Y. Xie, J. Duan, L. Peng, A. Arramel, and N. Li, *Adv. Photonics Res.* **2**(8), 2100012 (2021).
- <sup>203</sup>C. Li, J. Hu, S. Wang, J. Ren, B. Chen, T. Pan, X. Liu, and F. Hao, *J. Phys. Chem. Lett.* **12**(19), 4569–4575 (2021).
- <sup>204</sup>D. Li, T. Xia, W. Liu, G. Zheng, N. Tian, D. Yao, Y. Yang, H. Wang, and F. Long, *Appl. Surf. Sci.* **592**, 153206 (2022).
- <sup>205</sup>Y. Yu, C. Wang, C. R. Grice, N. Shrestha, D. Zhao, W. Liao, L. Guan, R. A. Awni, W. Meng, A. J. Cimaroli, K. Zhu, R. J. Ellingson, and Y. Yan, *ACS Energy Lett.* **2**(5), 1177–1182 (2017).

- <sup>206</sup>L. Ning, P. B. Ingabire, N. Gu, P. Du, D. Lv, X. Chen, L. Song, W.-H. Chen, and J. Xiong, *J. Mater. Chem. A* **10**(7), 3688–3697 (2022).
- <sup>207</sup>Y. Zhao, P. Zhu, M. Wang, S. Huang, Z. Zhao, S. Tan, T.-H. Han, J.-W. Lee, T. Huang, R. Wang, J. Xue, D. Meng, Y. Huang, J. Marian, J. Zhu, and Y. Yang, *Adv. Mater.* **32**(17), 1907769 (2020).
- <sup>208</sup>Y. Bi, E. M. Hutter, Y. Fang, Q. Dong, J. Huang, and T. J. Savenji, *J. Phys. Chem. Lett.* **7**(5), 923–928 (2016).
- <sup>209</sup>Z. Lian, Q. Yan, T. Gao, J. Ding, Q. Lv, C. Ning, Q. Li, and J.-L. Sun, *J. Am. Chem. Soc.* **138**(30), 9409–9412 (2016).
- <sup>210</sup>M. M. Byranvand, W. Zuo, R. Imani, M. Pazoki, and M. Saliba, *Chem. Sci.* **13**(23), 6766–6781 (2022).
- <sup>211</sup>R. Lin, J. Xu, M. Wei, Y. Wang, Z. Qin, Z. Liu, J. Wu, K. Xiao, B. Chen, S. M. Park, G. Chen, H. R. Atapattu, K. R. Graham, J. Xu, J. Zhu, L. Li, C. Zhang, E. H. Sargent, and H. Tan, *Nature* **603**, 73–78 (2022).
- <sup>212</sup>J. Tong, Q. Jiang, A. J. Ferguson, A. F. Palmstrom, X. Wang, J. Hao, S. P. Dunfield, A. E. Louks, S. P. Harvery, C. Li, H. Lu, R. M. France, S. A. Johnson, F. Zhang, M. Yang, J. F. Geisz, M. D. McGehee, M. C. Beard, Y. Yan, D. Kuciauskas, J. J. Berry, and K. Zhu, *Nat. Energy* **7**, 642–651 (2022).
- <sup>213</sup>R. Lin, K. Xiao, Z. Qin, Q. Han, C. Zhang, M. Wei, M. I. Saidaminov, Y. Gao, J. Xu, M. Xiao, A. Li, J. Zhu, E. H. Sargent, and H. Tan, *Nat. Energy* **4**, 864–873 (2019).
- <sup>214</sup>Q. Chen, J. Luo, R. He, H. Lai, S. Ren, Y. Jiang, Z. Wan, W. Wang, X. Hao, Y. Wang, J. Zhang, I. constantinou, C. Wang, L. Wu, F. Fu, and D. Zhao, *Adv. Energy Mater.* **11**(29), 2101045 (2021).
- <sup>215</sup>J. Zillner, H.-G. Boyen, P. Schulz, J. Hanisch, N. Gauquelin, J. Verbeeck, J. Küffner, D. Desta, L. Eisele, E. Ahlsweide, and M. Powalla, *Adv. Funct. Mater.* **32**(28), 2109649 (2022).